

# A Terabit Sampling System with a Photonics Time-Stretch ADC

Master Thesis  
of

Olena Manzhura

at the Institute for Data Processing and Electronics (IPE)



Reviewer: Prof. Dr. Anke-Susanne Müller (LAS)  
Second Reviewer: Dr. Michele Caselle (IPE)

15.11.2020 – 13.08.2021



# Declaration

I hereby declare that I wrote my master thesis on my own and that I have followed the regulations relating to good scientific practice of the Karlsruhe Institute of Technology (KIT) in its latest form. I did not use any unacknowledged sources or means, and I marked all references I used literally or by content.

Karlsruhe, 13.08.2021, \_\_\_\_\_  
Olena Manzhura

Approved as an exam copy by

Karlsruhe, 13.08.2021, \_\_\_\_\_  
Prof. Dr. Anke-Susanne Müller (LAS)



# Abstract

In many physical experiments and applications, e.g. beam diagnostics, measuring events occurring in the time range of femtoseconds over long periods of time is necessary. This imposes great technological challenges on Data Acquisition Systems (DAQs) and the Analog-To-Digital-Converters (ADCs) in them concerning sampling rate and memory space. In order to relax the requirements on the acquisition systems, the photonic time-stretch technique can be used to stretch the analog input signal in time. This way, the ADCs can be operated at a lower sample rate than the several THz that would be required without it. When measuring the signal with commercial DAQs, there still is another challenge. Due to the limited memory of such systems, continuous measurements at high sampling rates over a long period of time is not possible. Therefore new concepts for photonic time-stretch based DAQs are needed.

In this thesis, a first demonstrator of such a novel photonic time-stretch based DAQ system, called Terahertz Readout Sampling (THERESA), has been developed. The designed system consists of a high bandwidth front-end sampling card, mounted on a back-end readout card integrating a new generation of Radio-Frequency System-On-Chip (RFSoC) for readout and processing of the acquired samples.

The input signal (e.g. THz pulse) is first stretched using chirped optical pulses and exploiting the chromatic dispersion of two optical fibers. The stretched signal is then detected by a photodetector. The analog signal is sampled with the 16 channel front-end sampling card. Each channel contains a Track-And-Hold-Amplifier (THA) and a ADC (integrated in the RFSoC) capable of sampling at 2.5 GS/s. The sampling time of each THA can be delayed in time individually. Thereby the so-called time-interleaving method can be implemented, allowing for overall higher sampling rate. The design of the board allows it to be used with the time-stretch method as well as independently from it. Furthermore, the it allows for different sampling modes. In single-channel mode one detector is connected to one channel, allowing to acquire data from up to 16 detectors at the same time with one sampling point per channel. In the multi-channel mode, several channels are connected to one detector via a power-splitter, therefore allowing multiple samples per detector.

The RFSoC on the back-end readout card integrates a processing unit and a Field Programmable Gate Array (FPGA). A custom firmware running on the FPGA is responsible for configuring and controlling the components on the sampling card, as well as continuously acquiring the samples and relaying them to the following processing system via high-speed on-chip connections. The processing unit allows the user to control and monitor the overall system via common periphery or over a network connection.

Using the time-interleaving technique for all ADCs results in an overall achievable sample rate of 40 GS/s. With the time-stretch setup, a time resolution in the range of hundreds of femtoseconds is possible, considering the currently achievable time-stretch factors. THERESA therefore achieves the requirements set by particle accelerator facilities and can be a viable tool to be used in beam diagnostics, e.g. at Karlsruhe Research Accelerator (KARA).



# Contents

<b>1. Introduction</b>	<b>1</b>
1.1. Objective . . . . .	2
<b>2. Motivation</b>	<b>5</b>
2.1. Requirements in THz Science . . . . .	5
2.1.1. Coherent Synchrotron Radiation . . . . .	5
2.1.2. Electro-Optic Techniques for Longitudinal Bunch Profile Diagnostics	9
2.2. Photonic Time-Stretch Method . . . . .	10
2.3. Analog-To-Digital Converter . . . . .	12
2.3.1. Characteristics of Analog-To-Digital-Converters . . . . .	15
<b>3. Architecture Of The New Readout-System - THERESA</b>	<b>27</b>
3.1. State Of The Art Readout-Systems . . . . .	27
3.1.1. KAPTURE . . . . .	28
3.1.2. KAPTURE-2 . . . . .	31
3.2. Proposed Architecture for THERESA . . . . .	33
3.2.1. Front-End Sampling Card . . . . .	33
3.2.2. Readout Card . . . . .	39
<b>4. Design Of The Front-End Sampling Card</b>	<b>41</b>
4.1. Schematics . . . . .	41
4.1.1. Connectors . . . . .	44
4.1.2. Sampling-Channel . . . . .	46
4.1.3. Clock Distribution . . . . .	54
4.1.4. Digital-To-Analog-Converter Channels . . . . .	60
4.1.5. Power Supply . . . . .	61
4.2. Layout . . . . .	65
4.2.1. PCB Substrate Selection and Metal Layer Stackup . . . . .	66
4.2.2. Transmission Lines . . . . .	67
4.2.3. Component Placement and Routing . . . . .	77
<b>5. Back-End Readout Card and System Integration</b>	<b>81</b>
5.1. Xilinx ZCU216 Evaluation Card . . . . .	81
5.2. Firmware . . . . .	84
5.2.1. Programmable Logic - Hardware design . . . . .	85
5.2.2. Processing Unit - Software Design . . . . .	87
<b>6. Summary and Outlook</b>	<b>89</b>
<b>Acknowledgements</b>	<b>91</b>
<b>Appendix</b>	<b>93</b>
A. Characteristic Impedance Of Coplanar Waveguides . . . . .	93

B. Verilog Code for SPI Interface for Delay Chips . . . . .	94
<b>Acronyms</b>	<b>101</b>
<b>Bibliography</b>	<b>105</b>

# List of Figures

2.1.	Basic scheme of an electron storage ring (redrawn from [Rou14]) . . . . .	6
2.2.	Electromagnetic spectrum . . . . .	6
2.3.	Incoherent and coherent SR . . . . .	8
2.4.	Electrons interact with their own radiation [BBB <sup>+</sup> 19] . . . . .	8
2.5.	Scheme of scanning-type electro-optical sampling system [Rou14] . . . . .	9
2.6.	Scheme of spectrally encoded electro-optical detection system [Rou14] . . . . .	10
2.7.	Working principle of the electro-optical time-stretch technique [Rou14] . . . . .	11
2.8.	pn-junction with depleted region [Kei] . . . . .	11
2.9.	Transfer function of ideal, 3-bit ADC . . . . .	12
2.10.	SHA timing example . . . . .	13
2.11.	Track-And-Hold-Amplifier schematic and principle [Kes05] . . . . .	14
2.12.	Measurement setup for quantization error . . . . .	15
2.13.	Quantization noise as function of time (redrawn from [Kes05]) . . . . .	16
2.14.	Effects of Offset and Fain error in ADC . . . . .	18
2.15.	ADC Non-linearities . . . . .	19
2.16.	SFDR definition . . . . .	21
2.17.	Aperture jitter and SJNR . . . . .	23
2.18.	Aliasing . . . . .	25
3.1.	THz measurement with KAPTURE . . . . .	29
3.2.	Photo of the power-splitter developed at IPE . . . . .	29
3.3.	General architecture of the KAPTURE system . . . . .	30
3.4.	KAPTURE Pulse Sampling . . . . .	31
3.5.	Comparison between KAPTURE v1 and KAPTURE v2 . . . . .	32
3.6.	Photo of KAPTURE v2 system . . . . .	32
3.7.	General architecture of the THERESA sampling card . . . . .	33
3.8.	Time-Interleaving Method . . . . .	34
3.9.	Offset-mismatch in Interleaving [Har19] . . . . .	35
3.10.	Gain-mismatch in Interleaving [Har19] . . . . .	35
3.11.	Timing-mismatch in Interleaving [Har19] . . . . .	36
3.12.	Bandwidth-mismatch in Interleaving [Har19] . . . . .	36
3.13.	Track-And-Hold Timing diagram . . . . .	38
3.14.	Discrete components vs. IC . . . . .	40
4.1.	Capacitor equivalent circuit . . . . .	43
4.2.	Impedance response of a real capacitor . . . . .	43
4.3.	Rendering of FMC+ connector . . . . .	44
4.4.	Male and female type V connector . . . . .	45
4.5.	LPAM 8 × 50 connector . . . . .	46
4.6.	LPAM 6 × 20 connector . . . . .	46
4.7.	HMC5640 THA schematic . . . . .	48
4.8.	Connection of the analog and digital grounds at the THAs . . . . .	48

4.9.	Delay chip SDI connections	49
4.10.	NB6L295 delay chip schematic	50
4.11.	Schematic of a resistive voltage divider	51
4.12.	NB6L295 Delay Chip Schematic	51
4.13.	SN74AVC32T245 bus transceiver	53
4.14.	LVPECL driver topology	53
4.15.	Overview of the clocking paths on the sampling board	55
4.16.	PLL block diagram	55
4.17.	PLL block diagram	56
4.18.	PLL loop filter components	56
4.19.	Schematics of the LMX2594	58
4.20.	Schematic of the fanout	60
4.21.	DAC-channel with balun. Signal propagates from right to left.	61
4.22.	EMI-filter used for power supply	62
4.23.	Recommended schematic of the ADP1741 voltage regulator [Anaa]	64
4.24.	Via types	66
4.25.	Screenshot of the Polaris Si9000e	68
4.26.	Coplanar Waveguide with ground plane	69
4.27.	CWG, $Z_o$ vs $\epsilon_r$	70
4.31.	Edge-coupled differential coplanar waveguide	70
4.28.	CWG, $Z_o$ vs. $a$	71
4.29.	CWG, $Z_o$ vs. upper trace width	71
4.30.	Attenuation CPWG for 10 mm	72
4.32.	DCWG, $Z_{\text{diff}}$ vs. $w$	73
4.33.	DCWG, $Z_{\text{diff}}$ vs. $\epsilon_r$	73
4.36.	Symmetrical differential coplanar waveguide	73
4.34.	DCWG, $Z_{\text{diff}}$ vs. upper trace width	74
4.35.	Attenuation DCWG for 200 mm	75
4.37.	SCWG, $Z_{\text{diff}}$ vs. $w$	75
4.38.	SCWG, $Z_{\text{diff}}$ vs. $s$	75
4.39.	SCWG, $Z_{\text{diff}}$ vs. $\epsilon_r$	76
4.40.	SCWG, $Z_{\text{diff}}$ vs. upper trace width	76
4.41.	SCWG	76
4.42.	Trace accordions	78
4.43.	THA layout	79
4.44.	THERESA sampling card	80
5.1.	Topview of ZCU216 evaluation board with labeled components [Xilc]	82
5.3.	ZCU216 Evaluation Tool	82
5.2.	Zynq Ultrascale+ RFSoC block diagram	83
5.4.	Graphical User Interface (GUI) of the RF Data Converter Evaluation Tool	84
5.5.	Schematic of the firmware and processing unit on the readout card	85
5.6.	Simple example design with the Radio Frequency (RF) Data Converter	86
5.7.	Serial Data Interface (SDI) timing diagram for the NB6L295 delay chip [ONS]	86
5.8.	Xilinx ERNIC working principle example [Xilb]	87

# List of Tables

2.1. Some KARA parameters [Rot18] . . . . .	7
3.1. Real Time Oscilloscopes Examples . . . . .	28
4.1. FMC+ Voltages . . . . .	45
4.2. HMC5640 Characteristics . . . . .	47
4.3. NB6L295 Characteristics . . . . .	52
4.4. LMK04808B loop filter characteristics . . . . .	57
4.5. LMX2594 loop filter characteristics . . . . .	58
4.6. Power consumption of components on the board . . . . .	61



# 1. Introduction

In many scientific applications and experiments, the observation of non-repetitive, statistically rare events with very high occurrence rates is desired. As these events might occur on a time scale of femtoseconds, real-time measurement systems with fine temporal resolution are needed that are also capable of long acquisition times. This imposes high technological challenges on Data Acquisition Systems (DAQs) and Analog-To-Digital-Converters (ADCs).

One bottleneck in the acquisition of ultra-fast events is the limited timing performance of commercially available ADCs. The limitation posed by the converters is a trade-off between the dynamic range (Effective Number Of Bits (ENOB)) and sampling rate of the converters. With an increase in the sampling rate, ambiguity of the comparators (output neither '0' nor '1') inside the ADC and sampling errors due to clock jitter become major limiting factors on the overall performance. [MCB<sup>+17</sup>]

A first demonstration of a concept to overcome these limitations was presented in 1999 by [CBJ99]. The idea is to stretch the analog signal in time before digitizing it in the converter and hence relax the demands on the data converter performance. This time-stretching is accomplished by using chirped optical pulses and chromatic dispersion in optical fibers. The concept is therefore called “photonic time-stretch” and was successfully tested in combination with a moderate-speed ADC in [CBJ99].

Since then, the time-stretch method has been continuously improved and has found use in many applications. For example, in biomedical diagnostics, a first demonstration of an artificial intelligence based high-speed phase microscope has been developed. It uses time-stretch quantitative phase imaging (TS-QPI), a technique based on the time-stretch concept which enables simultaneous measurement of phase and spatial intensity profiles. This allows label-free classification of cells for cancer diagnostics and drug development. [MCB<sup>+17</sup>]

The time-stretch concept is also useful for applications in particle accelerators due to the short timescales involved. In a storage ring for example, relativistic electron bunches interact with their own radiation which can lead to the formation of spatial microstructures inside the bunches, a phenomenon also called micro-bunching instability. This is a source of intense pulses of terahertz radiation, the so called Coherent Synchrotron Radiation (CSR). Due to its non-ionizing nature, this radiation can be potentially used in imaging applications for many research fields such as biology and is therefore an important field of study. A first demonstration of direct observation of the micro-bunching instability was performed at the synchrotron facility Source optimisée de lumière d'énergie intermédiaire du LURE (SOLEIL) using a time-stretched signal together with a real-time oscilloscope. [RELP<sup>+15</sup>]

The use of the time-stretch method in different applications has demonstrated the advantages to measure events with femtosecond resolution. However, commercially available real-time diagnostics systems are limited in memory space. The current maximal memory depth

of such systems lies in the the range of few GS. This limits the acquisition time of such systems at maximum sampling rate, which lies in the range of a few milliseconds at best. Due to this limitation it is not possible to measure data continuously over a long period of time. This creates a problem in applications where a longer observation time (up to hours) is required, e.g. in accelerator applications where the turn-by-turn (and bunch-by-bunch) analysis of the electron bunches is desired in order to study the evolution of the bunch profiles.

This challenge was the motivation to design novel ultra-fast acquisition systems based on the photonic time-stretch ADC. Together with the next generation of Field Programmable Gate Array (FPGA)-based systems with integrated high-performance ADCs, this gives rise to a new concept of DAQ, the photonic time-stretch DAQ. The photonic time-stretch DAQ consists of a photonic part, containing the time-stretching section and the conversion of photons into electrical signal with a photo-detector. Furthermore, such a system has one or multiple ADCs converting the analog signals into digital samples. The digital samples are then processed in a computing unit and broadcast to other units as needed if the system is integrated e.g. into a cluster of distributed instrumentation systems.

### 1.1. Objective

In this thesis, a first demonstrator of a DAQ-system based on the time-stretch concept is developed. This system, called Terahertz Readout Sampling (THERESA), enables high-speed measurements of ultrafast events with a time resolution in the range of femtoseconds.

In order to achieve such high resolution, the time-stretch technique will be used in order to stretch the input signal in the range of pico- to nano-seconds. The input signal is continuously sampled by high-speed ADCs with a temporal resolution defined by the user as needed. To sample the signal, the ADCs need to have a sampling rate in the order of several GHz. The amplitudes of the signals to be measured are very small and an ADCs with an appropriate resolution has to be chosen in order to guarantee an ENOB of at least 10 b. [Ser]

This leads to the next challenge: Sampling at several GHz with high resolution implies a large amount of data, leading to a data rate in the range of terabits per second. In order to enable such a high data-throughput, the system will be based on a new generation of System-On-Chip (SoC), integrating a FPGA and a processing unit together with the high-speed ADCs. The SoC will have high-speed peripherals in order to guarantee the continuous high-speed data-throughput. Combination with the FPGA should allow for flexible system tuning for a user-defined application. The user will be able to control and configure the system via an application or operating system running on the processing unit.

Furthermore, the system should be compatible with already existing high-speed DAQ frameworks (e.g. based on PCI Express (PCIe)) and be easily integrated into the system for the user application (e.g. through optical fibers to a distributed instrumentation system). However, stand-alone operation should also be possible. Furthermore, the DAQ should be designed in such way that usage independently from the time-stretch method is possible.

The overall thesis is structured in the following way: In chapter 2 necessary theoretical background for the new THERESA system is given. The subject of Terahertz (THz) science in particular is touched being the main motivation for the design of the novel time-stretch sampling system. The general architecture of THERESA is covered in chapter 3, including also state of the art readout-systems, especially Karlsruhe Pulse Taking Ultra-fast Readout Electronics (KAPTURE) which is in operation at Karlsruhe Research Accelerator (KARA). The design steps of the front-end sampling card of THERESA are described in chapter 4 in detail. The description of the back-end readout card, as well as an overview of the design of

appropriate firmware is covered in chapter 5. At last, results are concluded and an outlook for the newly developed system is given.



## 2. Motivation

The main aspired use case of the newly developed time-stretch Data Acquisition System (DAQ) lies in accelerator physics applications. Especially Terahertz (THz) science e.g. at Karlsruhe Research Accelerator (KARA) is of interest. Therefore an introduction into this topic is given in the first section of this chapter.

After that the general architecture and basic theory of a photonic time-stretch DAQ is given. First, the basic working principle of the time-stretch concept is explained. Then, a short overview of the basic Analog-To-Digital-Converter (ADC) theory is given, together with the most important figures of merit. Knowledge and understanding of ADC characteristics is necessary to evaluate the overall performance of the converter in the next chapters.

### 2.1. Requirements in THz Science

Recent years have seen an increasing interest in THz radiation, ranging from 3 THz up to 30 THz<sup>1</sup>, as it allows non-destructive analysis of organic material. This is possible because unlike e.g. X-Rays, THz radiation is not ionizing. It is therefore of great interest to use THz radiation in fields like biology, medicine or material science. However, until recently the usage of THz radiation was very limited, as generation of such radiation has proven to be difficult.

Synchrotrons and storage rings are a potential source of THz radiation. The emission of THz radiation is closely linked to instabilities of the charged particles which are accelerated in a synchrotron (see [Mü12]). These instabilities occur in the time range of femtoseconds and cause bursts of THz radiation. The periodicity of these bursts depends on multiple parameters of the synchrotron and therefore imposes a challenge on controlling the emission of THz radiation. Studying the dynamics of these instabilities is an important step towards the application of synchrotrons as source of THz radiation. [Rot18]

#### 2.1.1. Coherent Synchrotron Radiation

In synchrotron radiation facilities synchrotron radiation (SR) is produced by accelerating relativistic electrons. Emission of SR occurs when electron beams are bent or deflected with dipole magnets or using undulators. The latter are used to make the electrons oscillate by generating a periodic magnetic field. Figure 2.1 shows the general scheme of an electron storage ring.

Electrons, which are grouped to “electron bunches”, are generated with an electron gun and accelerated to relativistic speeds<sup>2</sup> by a pre-accelerator (often a linear accelerator (LINAC), a booster ring accelerator or a microtron with a booster). After being brought up to their nominal energy, the bunches are injected into the storage ring. In the ring, the path of the

---

<sup>1</sup>At KARA: 0.1 THz to 1.2 THz

<sup>2</sup>almost speed of light

electron bunches is altered by dipole magnets, guiding them on a circular trajectory. Due to emission of SR at each bend, the electrons lose energy, which has to be compensated for. This is done by accelerating the electrons with an electric field inside a Radio Frequency (RF) cavity. Not shown in the drawing are the beamlines, which lead the SR radiation, or rather chosen wavelength ranges, through an optical system to the respective user experiments. [Rou14, Rot18]

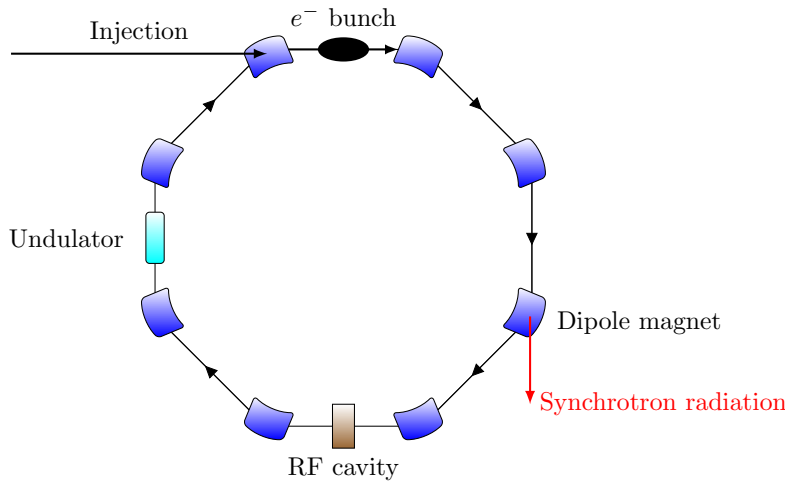


**Figure 2.1.** Basic scheme of an electron storage ring (redrawn from [Rou14])

The range of SR reaches from hard X-rays down to the infrared region of the electromagnetic spectrum (see Figure 2.2). SR shows properties like high intensity, high collimation, polarisation and generation in pulses of well-defined time duration. High intensity is necessary for better penetration of the matter under study. It prevents unnecessary exposure of the matter outside the area of interest and improves the image quality by producing less scatter radiation from these areas. Well defined duration of the pulses allows to observe chemical reactions on short time scales. Due to this properties, synchrotrons are used for microscopy, spectroscopy, and time-resolved experiments in such fields like condensed matter physics, biology, material science and many more. [ESR]

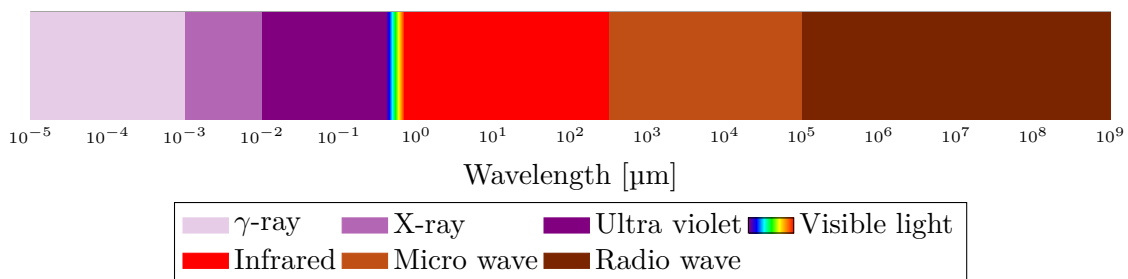


**Figure 2.2.** Electromagnetic spectrum

**Table 2.1.** Some KARA parameters [Rot18]

Parameter	Value
Beam energy (max.)	2.5 GeV
Circumference	110 m
Revolution Frequency (one electron)	2.7 MHz
<b>Minimum bunch spacing</b>	
multi-bunch	2 ns
single-bunch	368 ns
<b>Bunch length (rms)</b>	
normal operation	45 ps
short bunch	2 ps

### Karlsruhe Research Accelerator

At the synchrotron light source KARA, the possibility to utilize a synchrotron as a source of THz is actively researched. The photonic time-stretch DAQ, which has been developed in this thesis, should also be integrated into the beam diagnostics system at KARA. Therefore, a short overview of some parameters of this facility is given below.

KARA is located at Karlsruhe Institute of Technology (KIT) and is operated by the Institute of Beam Physics and Technology (IBPT). The storage ring can be filled up with up to 184 electron bunches with a distance of 2 ns ( $\cong 500$  MHz) between two adjacent bunches. The main accelerator parameters are listed in Table 2.1.

One scientific focus at KARA lies in the study of so-called micro-bunching instabilities which are described next.

### Micro-Bunching Instabilities

Increasing demands in current and future accelerators applications call for higher brilliance of the emitted radiation. Brilliance denotes both the brightness and the angular spread of the beam. Higher brilliance allows to see more detail in the material under study. [ESR] The higher brilliance is achieved by shortening the electron bunches. As illustrated in Figure 2.3, this results in emission of Coherent Synchrotron Radiation (CSR), the spectrum of which spans from 100 GHz up to THz. Due to this CSR the bunches interact with their own radiation as shown in Figure 2.4, which introduces complex longitudinal dynamics. [Rot18, Bro20]

These dynamics are the so called micro-bunching instabilities: the formation of micro-structures (in the sub-millimeter range) in the longitudinal density profile of the electron bunches. These instabilities occur in bursts and are hard to control, as they depend on a number of system parameters. This imposes on one side a huge limitation to the stable operation of the overall system at high current density/short bunch length mode. On the other side, these instabilities themselves emit brilliant THz radiation that could be potentially used in imaging applications. Such applications however require a stable power of the radiation. Therefore, a control of these instability bursts could potentially make them a source of THz radiation for user-applications. A thorough understanding and studying of these beam dynamics is therefore an important step towards providing an applicable THz source. [Rot18, Bro20] In order to make such investigations possible, appropriate beam diagnostic systems are required, which are capable of both capturing (ultra-)fast and long-term changes in the bunch profile.

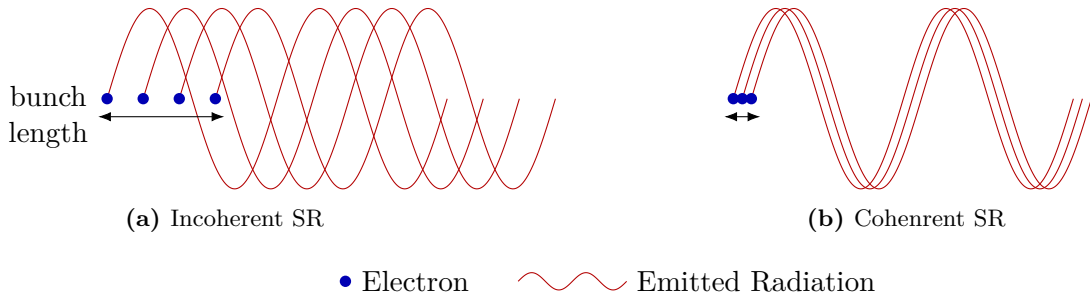


**Figure 2.3.** Incoherent SR and coherent SR due to shorter electron bunch length [Rot18]

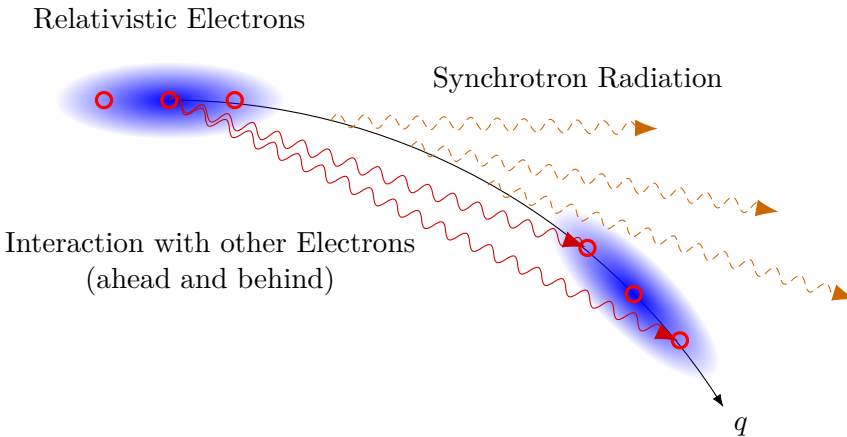


**Figure 2.4.** Electrons interact with their own radiation [BBB<sup>+</sup>19]

### Control of Micro-Bunching Instabilities

The Exploration et contrôle ULTRArapide de la dynamique des paquets d'électrons dans les sources de lumière SYNChrotron (ULTRASYNC) project, funded by ANR-DFG<sup>3</sup>, has an objective of ultrafast study and control of electron bunches in synchrotron light sources.

There is the question of control (i.e. suppression) of the bursts of THz radiation occurring during the micro-bunching instability. The goal is to obtain a high power and stable coherent emission. The current experimental setup uses a relatively simple feedback loop:

- A bolometer/Schottky barrier diode detector which produces the input signal for the feedback loop.
- A low-cost Field Programmable Gate Array (FPGA) that controls the accelerating voltage of the synchrotron based on the input

However, there are limitations in the controllable bunch charge in the accelerator this feedback loop can handle, which is around 10 mA. Therefore, an open question is whether measuring each THz pulse using the setup

- Electro-Optic Sampling (EOS) and time-stretching
- Association with the new FPGA-based system, i.e. Terahertz Readout Sampling (THERESA) system

<sup>3</sup>Agence Nationale de la Recherche (ANR), Deutsche Forschungsgemeinschaft (DFG)

- Finding adequate feedback, programmed in the FPGA

would help in solving the problem and allow the control to succeed also at higher currents (goal: 15 mA). [Ser]

### 2.1.2. Electro-Optic Techniques for Longitudinal Bunch Profile Diagnostics

Methods for analyzing the longitudinal profile of electron bunches are based on a similar, if not the same, Electro-Optic (EO) concept as the time-stretch method. Two most prominent methods are briefly described for the sake of completeness.

#### Scanning-Type Electro-Optic Sampling

The scanning-typeEOS samples one point at the time of the THz pulse, emitted e.g. from an electron bunch, at each acquisition, hence the naming of this method.

A short laser pulse (duration typically hundreds of femtoseconds) co-propagates with a THz pulse from CSR (range of picoseconds) in an EO crystal. Due to the Pockels effect the THz pulse causes a time dependent birefringence in the crystal. This modulates the polarization state of the laser pulse.

To sample the pulse, the delay between the laser and the THz pulse is varied. To detect the changing polarization, the polarization of the laser pulse is transformed into an intensity modulation. This is done by using polarizers, e.g. Quarter-Wave Plates (QWPs) and Wollaston Prism (WP) (as shown in Figure 2.5). A general scheme of the system is shown in Figure 2.5. For this technique a stable emission of the THz pulses is crucial, as they are not measured in one acquisition. [Rou14]

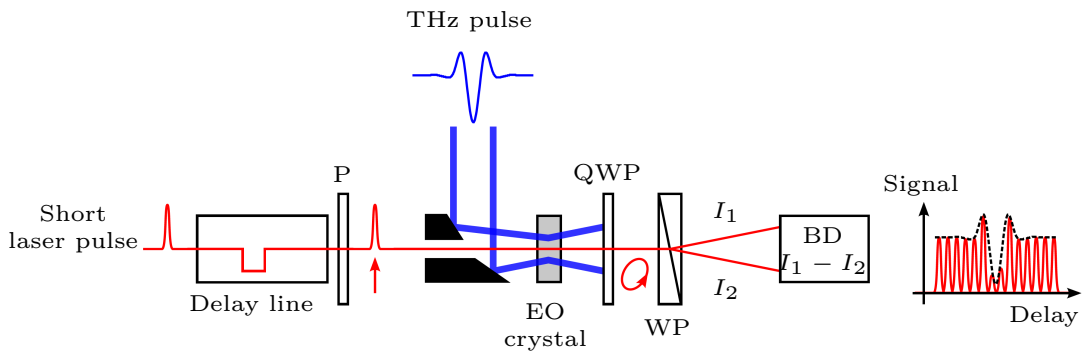


**Figure 2.5.** Scheme of scanning-type electro-optical sampling system [Rou14]

#### Spectrally Resolved Electro-Optic Detection

In contrast to the EOS, single-acquisition is possible with the spectrally resolved EO detection technique. The short laser pulse is first stretched to a duration similar to the THz pulse in a dispersive material, called stretcher. In this way the pulse is chirped, meaning the instantaneous frequency of the pulse varies over time. Together with the THz pulse, the laser pulse propagates through an EO crystal. Again, the induced birefringence modulates the laser pulse in time and in the spectral domain. The polarization state of the pulse is converted into an intensity modulation. This is done with a series of QWP, Half-Wave Plate (HWP) and a polarizer (P) (as shown in Figure 2.6). To retrieve the THz pulse shape in time, the spectrum of the laser pulse is measured with an optical spectrometer. A general scheme of the system is shown in Figure 2.6. [Rou14]

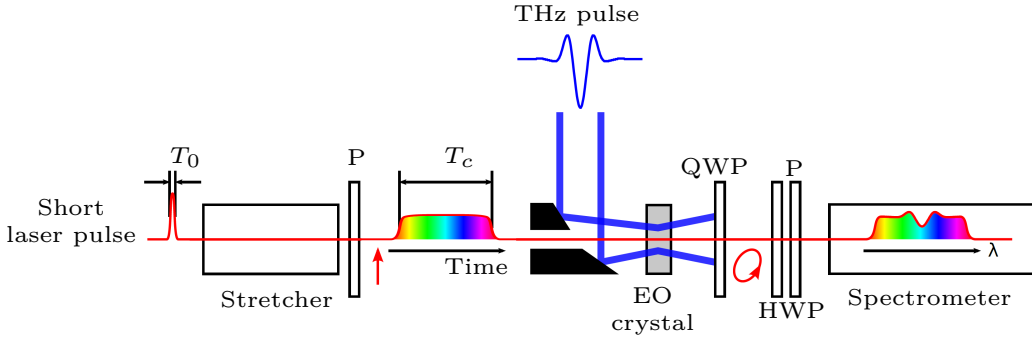


**Figure 2.6.** Scheme of spectrally encoded electro-optical detection system [Rou14]

The temporal resolution of this method is limited due to the finite chirp rate

$$\text{chirp rate} = \frac{\text{laser bandwidth}}{\text{laser pulse duration after stretcher}}. \quad (2.1)$$

The minimal resolution  $T_{\min}$  depends on the bandwidth-limited pulse duration (before stretcher)  $T_0$  and the duration of the chirped laser pulse  $T_c$  (see [Rou14]):

$$T_{\min} = \sqrt{T_0 T_c} \quad (2.2)$$

## 2.2. Photonic Time-Stretch Method

The operating principle of the optical time-stretch technique can be described in three steps (see Figure 2.7).

First, a short laser pulse (duration typically hundreds of femtoseconds) propagates in a dispersive medium, e.g. an optical fiber of length  $L_1$  (see Figure 2.7). With the optical bandwidth of the laser pulse  $\Delta\lambda$  and the dispersion parameter  $D_1$  of the fiber, this results in a chirped laser pulse of the duration

$$T_1 = \Delta\lambda D_1 L_1. \quad (2.3)$$

The next step is the time-to-wavelength-mapping, where a temporal intensity modulation is imprinted on the chirped pulse. This happens when the laser pulse co-propagates with another pulse, e.g. a THz pulse from CSR (duration in the range of picoseconds), in an EO crystal. Due to the Pockels effect the THz pulse causes a time-dependent birefringence in the crystal. The Pockels effect describes the phenomenon of occurring and change of existing birefringence in an electric field, which is linearly proportional to the electric field strength. [DID]

After that, the modulated chirped pulse propagates through another dispersive medium, a fiber of the length  $L_2$ . In this way, the temporal modulation of the pulse is further stretched to the duration  $T_2$ , which is long enough for detection with photodetectors and the digitizing with ADCs. [Rou14]

The factor  $M$ , by which the pulse is slowed down, is calculated as (see [Rou14])

$$M = 1 + \frac{L_2}{L_1}. \quad (2.4)$$

As example, assume the length of the dispersive media as  $L_1 = 10\text{ m}$  and  $L_2 = 2\text{ km}$  and an input signal with the duration  $T_{\text{sig}} = T_1 = 1\text{ ps}$ . With Equation 2.4 the stretching factor for this set-up is  $M \approx 200$ . The input pulse is stretched to  $T_2 = M \cdot T_1 = 200 \cdot 1\text{ ps} = 200\text{ ps} = 0.2\text{ ns}$ . This corresponds to a frequency of 5 GHz which is much easier to handle e.g. for an oscilloscope.

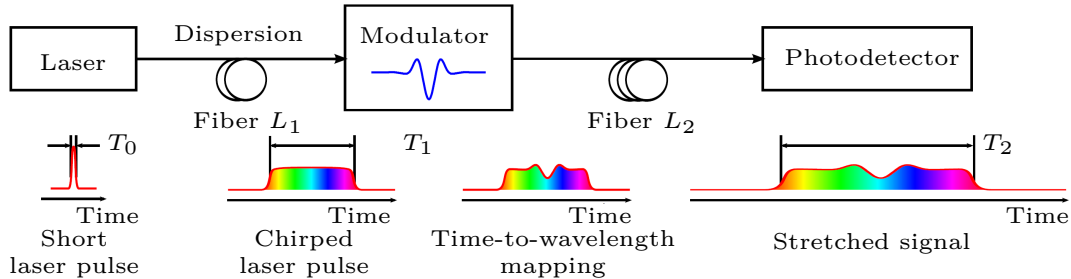


**Figure 2.7.** Working principle of the electro-optical time-stretch technique [Rou14]

### Photodetector

In order to convert the time-stretched optical signal into an electrical value, a photodetector, e.g. a photodiode, is needed. A circuit is a photo-diode operated in reverse bias, meaning the *p*-side is connected to the negative terminal and the *n*-side to the positive terminal of a power supply with some sort of current-limiting capability. This enlarges the depletion region (see Figure 2.8) of the *p/n*-junction as the depletion region contains only a very small amount of free charge carriers. Irradiating the diode with photons of sufficient energy generates electron-hole pairs due to the photoelectric effect. If the electron-hole pairs are produced in the depleted region of the *p/n*-junction, they are separated by the electric field applied across, before they can recombine. This creates a so called photo-current which can be measured and converted into a voltage signal. [Ele]

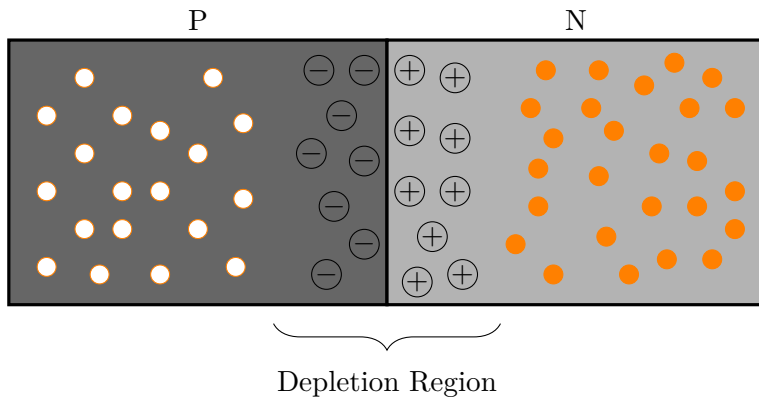


**Figure 2.8.** pn-junction with depleted region [Kei]

### 2.3. Analog-To-Digital Converter

ADCs are used to translate analog signals, like voltages, into the digital representation of these signals. This *digitized* version can then be stored and processed by information processing, computing, data transmission and control systems. This translation, also called “conversion”, can be seen as encoding a continuous-time analog input  $V_{\text{in}}(t)$  (voltage) into a series of discrete,  $N$ -bit words. This process is also called *sampling*. With the full-scale voltage of  $V_{\text{FS}}$ <sup>4</sup>, the individual output bits  $b_k$  and the quantization error  $\epsilon$  (see subsubsection 2.3.1.1), the ADC should satisfy the relation (see [LV02])

$$V_{\text{in}}(t) = V_{\text{FS}} \sum_{k=0}^{N-1} \frac{b_k}{2^{k+1}} + \epsilon. \quad (2.5)$$

This can also be rewritten in terms of the Least Significant Bit (LSB) or quantum level  $V_Q$  (see [LV02])

$$1 \text{ LSB} = \frac{V_{\text{FS}}}{2^N} = V_Q. \quad (2.6)$$

With Equation 2.5 this leads to

$$V_{\text{in}} = V_Q \sum_{k=0}^{N-1} b_k 2^k + \epsilon. \quad (2.7)$$

Figure 2.9 shows the ideal transfer function of a 3-bit ADC. Each digital  $N$ -bit word corresponds to a range of input voltage values (*code width*), which is centered around a *code center*. [LV02] The input voltage is resolved to the code of the nearest code center.

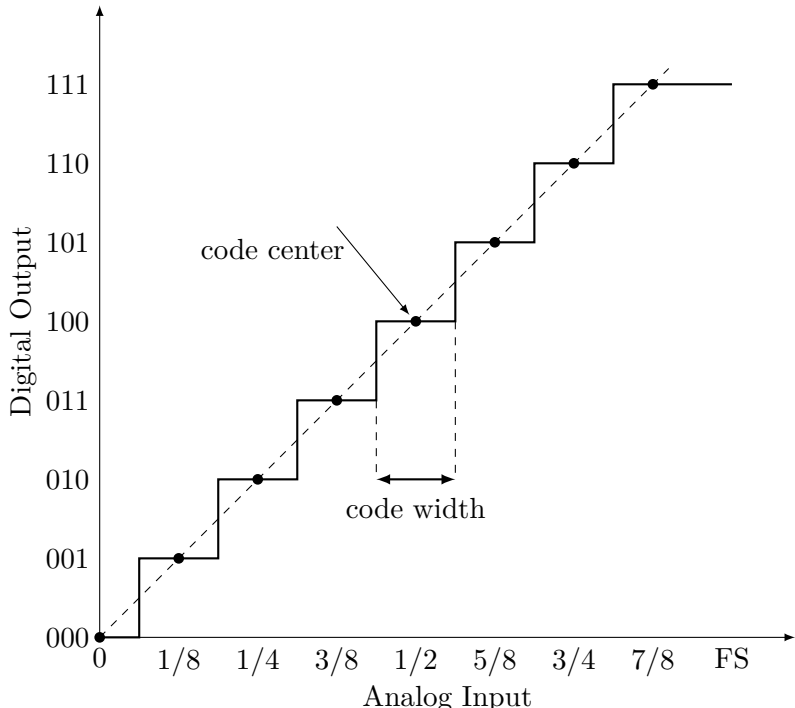


**Figure 2.9.** Transfer function of an ideal, 3-bit ADC (redrawn from [LV02])

<sup>4</sup>Maximal voltage the converter can output

### Sample-And-Hold-Amplifier

ADCs need a certain amount of time to sample the input signal. If the level of the analog signal changes by more than one LSB during this period, this can result in large errors in the output signal. Therefore so called Sample-And-Hold-Amplifier (SHA) are used in front of the ADC to hold the input level constant for the needed amount of time. [Kes05]

It consists of an input and output buffer, a switch controlled by the sampling clock and a capacitor. The analog input is buffered in an input buffer which leads to a switch that is controlled by a sampling clock. During the sample mode, i.e. during the negative sampling clock cycle, the switch is open. At the transition from negative to positive clock cycle, the switch closes, connecting the input signal with the capacitor which is charged in this way. [Kes05]

The ADC sampling time needs to be timed in such way, that the whole duration of an analog-to-digital conversion falls into the hold period of the SHA and does not exceed into the sample period. Figure 2.10 shows a qualitative example for proper sample timing. As conclusion, the upper frequency limitation is not determined by the ADC itself, but rather by the aperture jitter, bandwidth, distortion, etc. of the SHA. [Kes05]

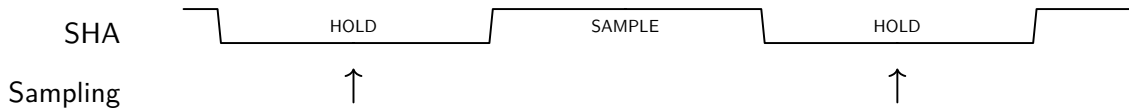
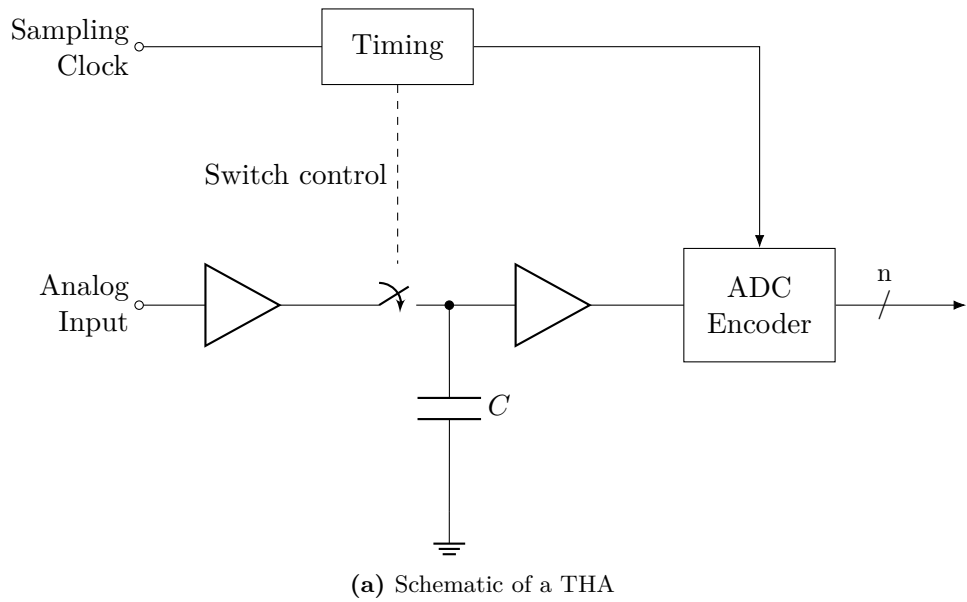


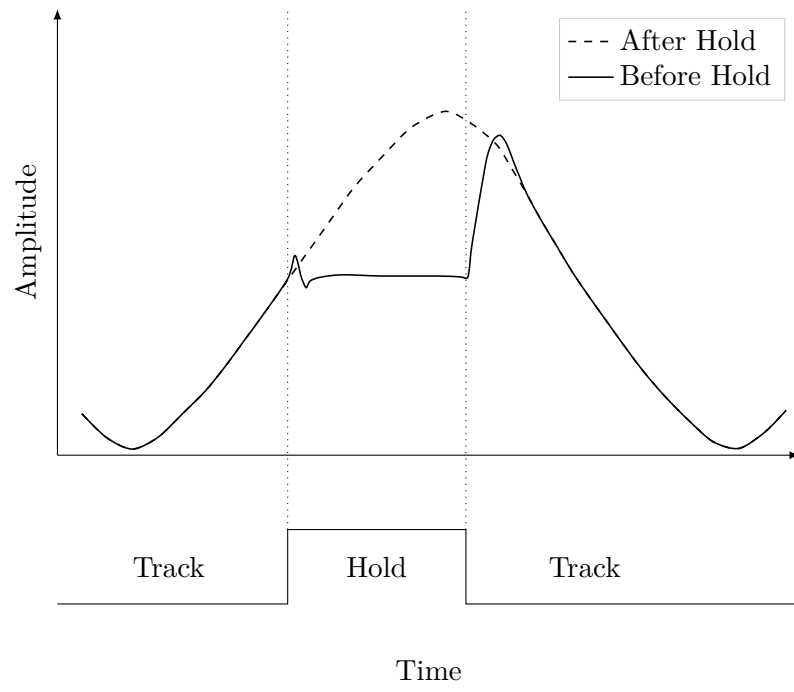
**Figure 2.10.** Example for appropriate sampling timing when using Sample-And-Hold-Amplifier. The sample points of the ADC should be inside the period, where the SHA holds the input value.

### Track-And-Hold Amplifier

Apart from the SHAs there also exists the so called Track-And-Hold-Amplifier (THA). A general block diagram of a THA is shown in Figure 2.11a. Though the names are often used interchangeably, there is one fundamental difference between a SHA and a THA. Strictly speaking, the output of a SHA is not defined during the sample period. Only when switching to the hold mode, the output is assigned to a defined value: the voltage level at the input in that moment. Contrary to that, the THA acts as a unity gain amplifier during the sample period, meaning the output is just a replication of the input. The THA “tracks” the input signal (see also Figure 2.11b). Therefore, instead of speaking of a “sample” period, the term used here is the “track” period. When switching to hold mode, the instantaneous input level is held over the course of the hold period. This principle allows to improve the sampling rate, as the settling time of an THA is in general smaller than the one of a SHA. Settling time denotes the amount of time needed for the output voltage to be at a stable level, after the transition from track/sample to hold mode. This process is quicker, when the output voltage is already in the range of the sampled input at the moment, instead of when the hold capacitor first has to be charged to the input voltage. [Ree17]



(a) Schematic of a THA



(b) Working principle of the THA

**Figure 2.11.** Track-And-Hold-Amplifier schematic and principle [Kes05]

### 2.3.1. Characteristics of Analog-To-Digital-Converters

For an ideal converter, the number of bits and the sampling rate would be sufficient to fully characterize its performance. Real ADCs however differ from the ideal behavior by introducing static and dynamic imperfections. Different applications have different requirements, which leads to a number of specifications. These can be divided into the categories according to [LV02]:

- Quantization Noise
- Static parameters
- Frequency-domain dynamic parameters
- Time-domain dynamic parameters

This section provides an overview of these figures of merit. Which of them are needed to specify the necessary performance of the ADC has to be chosen for each application accordingly.

#### 2.3.1.1. Quantization Noise

Even an ideal  $N$ -bit converter has errors resulting from the quantization process which can be modeled like noise. The reason is that each  $N$ -bit word represents a certain range of analog input values, which is 1 LSB wide and centered around a code center (see Figure 2.9). [LV02]

The input voltage is assigned to the word of the nearest code center. This means that there will always be a difference between the corresponding voltage of the respective digital code  $x_q(t)$  and the actual analog input voltage  $x(t)$ . This difference is called the *quantization error*. For an equidistant quantization, the quantization error for a code width  $q$  is (see [Pue15])

$$|e_q(t)| = |x(t) - x_q(t)| \leq \frac{q}{2}. \quad (2.8)$$

A setup in order to measure this quantization error is shown in Figure 2.12.

The output of the ADC, the  $N$ -bit code corresponding to the voltage level of the input signal  $x(t)$ , is fed to a Digital-To-Analog-Converter (DAC), which converts this code into a corresponding voltage level  $x_q(t)$ . The difference between  $x(t)$  and  $x_q(t)$  is the quantization error  $e_q(t)$ .

In order to analyze the quantization noise and the resulting theoretical maximum Signal-To-Noise-Ratio (SNR) of the ideal ADC, assume a ramp with the slope  $s$  as an input signal. Then, the quantization error  $e_q(t)$  can be approximated with a sawtooth signal in the time domain (see [Kes05]):

$$e_q(t) = st, \quad -\frac{q}{2s} < t < \frac{q}{2s} \quad (2.9)$$

The function in Equation 2.9 is plotted in Figure 2.13.

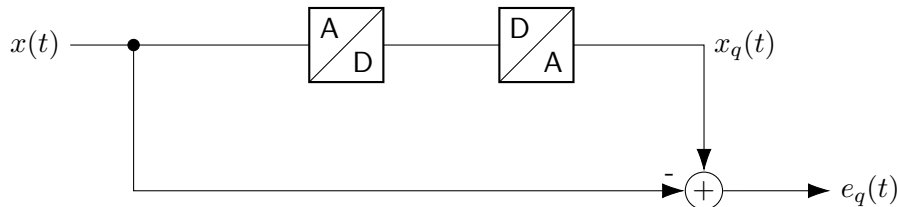


**Figure 2.12.** Setup for measuring the quantization error of an (ideal) ADC with input signal  $x(t)$

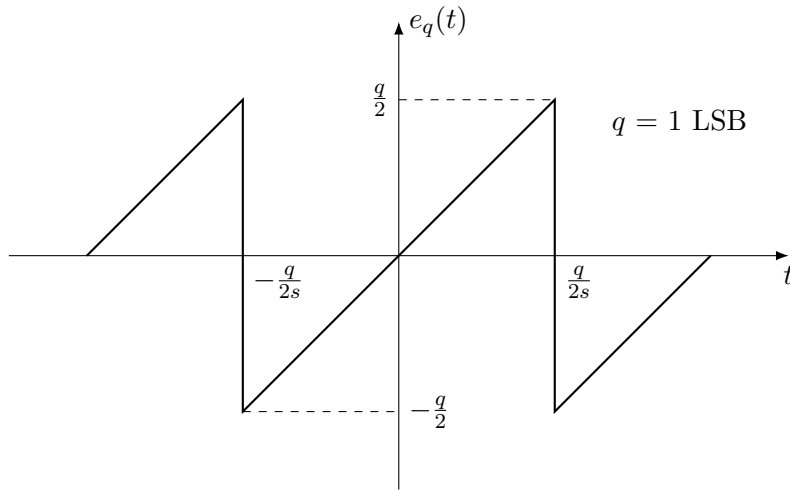


**Figure 2.13.** Quantization noise as function of time (redrawn from [Kes05])

The power of this quantization noise can be calculated as the mean-square  $e_{\text{rms}}^2$  of  $e(t)$  (see [Kes05]):

$$P_{\text{QN}} = e_{\text{rms}}^2 = \overline{e^2(t)} = \frac{s}{q} \int_{-q/2s}^{+q/2s} (st)^2 dt = \frac{s^3}{q} \left[ \frac{t^3}{3} \right]_{-\frac{q}{2s}}^{+\frac{q}{2s}} = \frac{q^2}{12} \quad (2.10)$$

In order to calculate the maximal SNR of an ideal converter, a full-scale input sine wave is applied to the input:

$$u(t) = u_s \sin(2\pi ft) = \frac{2^N q}{2} \sin(2\pi ft) = 2^{N-1} q \sin(2\pi ft) \quad (2.11)$$

With the effective value of the signal amplitude

$$u_{\text{eff}} = \frac{u_s}{\sqrt{2}} = \frac{2^{N-1} q}{\sqrt{2}} \quad (2.12)$$

the SNR can be calculated as

$$\text{SNR} = \frac{P_{\text{signal}}}{P_{\text{noise}}} = \frac{u_{\text{eff}}^2}{e_{\text{rms}}^2} = \frac{2^{2N-2} q^2 / 2}{q^2 / 12} = 2^{2N} \cdot 1.5. \quad (2.13)$$

In decibel, the SNR is calculated as (see [Pue15, Kes05]):

$$\text{SNR}_{\text{dB}} = 10 \log (2^{2N} \cdot 1.5) = 6.02N + 1.76 \quad (2.14)$$

### 2.3.1.2. Static parameters

*Static parameters* are specifications, which can be measured at low speed/DC.

#### Accuracy

*Accuracy* is the total error with which an ADC can convert a known voltage, which includes the effects of (see [LV02]):

- Quantization error
- Gain error
- Offset error
- Non-linearities

#### Resolution

*Resolution* is the number of bits  $N$  of the ADC. Depending from the resolution are the size of the LSB, which in its turn determines the dynamic range, code widths and quantization error.

#### Dynamic Range

The *dynamic range* represents the ratio between smallest possible output (LSB voltage) and the largest possible output (full-scale voltage). It can be calculated as

$$20 \log 2^N \approx 6N. \quad (2.15)$$

#### Offset and Gain Error

The *offset error* is defined as the deviation of the actual ADC transfer function from the ideal ADC transfer function in the point of zero. It is measured in LSB.

*Gain Error* defines the deviation of the slope of the line going through the zero and full-scale point of the transfer function. Figure 2.14 visualizes the effects of both offset and gain error.

These errors can easily be corrected by calibration. In order to measure the offset and gain error, two different voltage levels  $V_1$  and  $V_2$  are applied at the ADC input. This results in corresponding bit codes  $b_1$  and  $b_2$ . The slope  $s$  of the transfer function can then be calculated by

$$s = \frac{b_2 - b_1}{V_2 - V_1}. \quad (2.16)$$

From this, the gain error can be determined. In order to obtain the offset error  $b$ , the linear equation

$$b = b_1 - s \cdot V_1 \quad (2.17)$$

is solved.

#### Integral and Differential Non-Linearity Distortion

Integral Nonlinearity (INL) is the distance of the code centers on the actual ADC transfer function from the ideal line (dashed line in Figure 2.15). It results from the integral non-linearities of the front-end, SHA and also the ADC itself [Kes05, LV02].

Differential Nonlinearity (DNL) is the deviation in actual code width from the ideal width of 1 LSB. This non-linearity stems exclusively from the encoding process in the ADC. [LV02, Kes05]

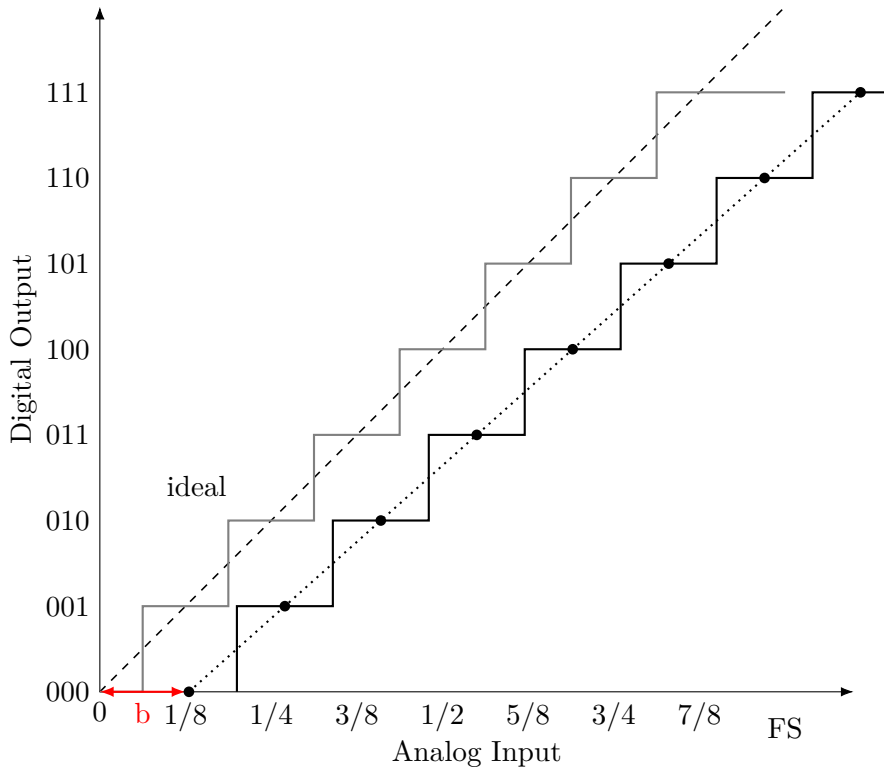


**Figure 2.14.** Offset and Gain Error in the ADC characteristic transfer function. The offset error is indicated with the red arrow. The gain error expresses itself via different slope of the real ADC (dotted) compared to the ideal ADC (dashed)

The effect of these errors is shown in Figure 2.15.

These non-linearities could be measured with a histogram test. A voltage ramp is applied at the input and the number of occurrences of each ADC output code,  $n(\text{code})$ , is measured. With the ramp slope  $s$  ( $[s] = \text{V/s}$ ) of an ideal ADC with the sampling frequency  $f_s$  would give (see [Vol])

$$n(\text{code}) = \frac{\text{LSB}}{s} \cdot f_s = n_{\text{avg}}, \quad (2.18)$$

which ideally would be constant for the whole input range (except for the first and last code). For a real ADC this is not the case and the DNL and INL are calculated as (see [Vol])

$$\text{DNL}(\text{code}) = \frac{n(\text{code}) - n_{\text{avg}}}{n_{\text{avg}}} \quad (2.19)$$

$$\text{INL}(\text{code}) = \sum_{i=0}^{\text{code}} \text{DNL}(i). \quad (2.20)$$

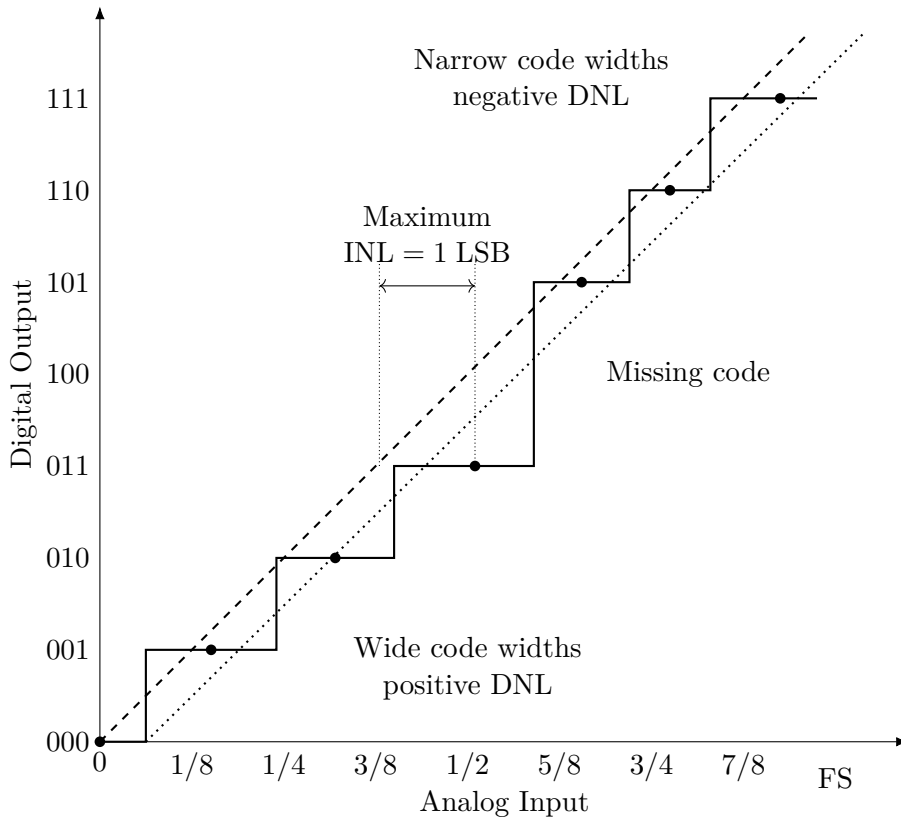


Figure 2.15. Transfer function of a real ADC showing DNL and INL [LV02]

### 2.3.1.3. Frequency-Domain Dynamic Parameters

Any real ADC is subject to noise distortion. *Noise* denotes any unwanted random signal, which interferes with the measuring of the desired signal. Examples are quantization noise or random fluctuations due to thermal noise. *Distortion* is the term for alteration of the shape of the original signal. As an example, distortion of the amplitude might result due to not equal amplification of the parts of a signal. [wil]

In an ADC (with built-in SHA) there are a couple of sources, which introduce noise and distortion:

- **Input Stage:** Wideband noise, non-linearity and bandwidth limitation
- **SHA:** Non-linearity, aperture jitter (see subsubsection 2.3.1.4) and bandwidth limitation
- **ADC:** Quantization noise, non-linearity

For quantification of noise and distortion, frequency-domain metrics are used. Therefore the figures of merit described in the following paragraphs are also called frequency-domain dynamic parameters. These parameters are measured with the help of the Fast-Fourier-Transform (FFT) meaning any modern oscilloscope can be used to quickly assess the frequency-domain dynamic performance for a given input at the ADC. As some parameters, such as Spurious-Free Dynamic Range (SFDR), are only defined for one carrier input frequency, several measurements at different input frequencies need to be carried out in order to fully characterize the ADC.

In the following paragraphs, an overview of the metrics for quantification of the noise and distortion of an ADC is given.

## Signal-to-Noise Ratio

The SNR is defined as the ratio of the input signal power to the power of the noise signal. It is expressed in dB and can be calculated using the Root Mean Square (RMS) value of the signal and noise amplitudes (see [Xila]):

$$\text{SNR} = \frac{\text{Power}_{\text{Signal}}}{\text{Power}_{\text{Noise}}} \quad (2.21)$$

$$= \left( \frac{\text{Amplitude}_{\text{Signal, rms}}}{\text{Amplitude}_{\text{Noise, rms}}} \right)^2 \quad (2.22)$$

$$= 20 \log \left( \frac{V_{\text{in, rms}}}{V_{\text{Q, rms}}} \right) \quad (2.23)$$

Usually, the SNR degrades at higher frequencies due to sampling jitter. [Xila]

## Signal-to-Noise-and-Distortion Ratio

Signal-to-Noise-and-Distortion Ratio (SINAD) (also called SNDR or S/N+D) denotes the ratio between the RMS of the signal amplitude to the mean value of the Root Sum Square (RSS) of all other spectral components, including harmonics, but excluding Direct Current (DC) (0 Hz). SINAD is a good indication over the general dynamic performance of the ADC, as it includes all contributions from noise and distortion. The higher the SINAD the stronger the input power is differentiated from noise and spurious components. [Xila]

SINAD can be calculated from the average power of the input signal  $P_{\text{signal}}$ , noise  $P_{\text{noise}}$  and  $P_{\text{distortion}}$  (see [Xila]):

$$\text{SINAD} = 10 \log \left( \frac{P_{\text{signal}}}{P_{\text{noise}} + P_{\text{distortion}}} \right) \quad (2.24)$$

It is commonly expressed in dB, decibels relative to the carrier (dBc) or decibels relative to full scale (dBFS).

## Effective-Number-Of-Bits

The Effective Number Of Bits (ENOB) expresses the SINAD in terms of bits. It can be calculated as (see [Kes09])

$$\text{ENOB} = \frac{\text{SINAD} - 1.76 \text{ dB}}{6.02 \text{ dB/b}}. \quad (2.25)$$

This is derived from solving the equation of the “ideal SNR” (Equation 2.14) for the number of bits  $N$  and substituting SNR with SINAD. This however means, that this parameter assumes a full-scale input signal. Expressing the ENOB for a smaller signal amplitude requires measuring the SINAD at this level and a correction factor. [Kes05]

## Spurious-Free Dynamic Range

SFDR indicates the dynamic range of the converter, which can be used, before there is interference or distortion from spurious components with the fundamental signal. [LV02] The SFDR is calculated as the RMS value of the fundamental signal to the RMS value of the worst spurious signal, i.e. the highest spur in the spectrum. It is measured over the whole Nyquist bandwidth from DC to  $f_s/2$ , with  $f_s$  being the ADC sampling rate. The spur may or may not be a harmonic of the fundamental signal. [Kes09, LV02]

The SFDR is an important characteristic in the sense, that it indicates the smallest signal which can still be distinguished from a strong interfering signal. [Kes09]

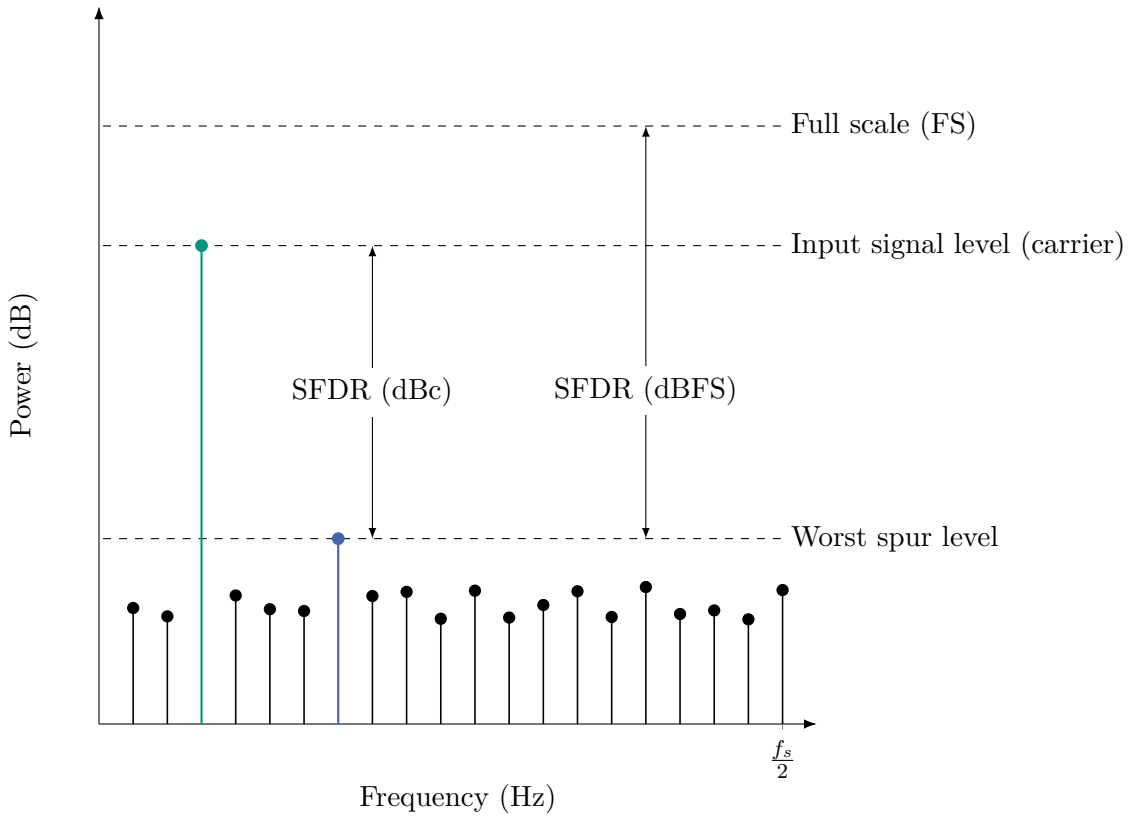


**Figure 2.16.** Visualization of the SFDR. It can be indicated either with reference to the carrier frequency in “dBc” or with reference to the Full-Scale Input in “dBFS”. [Kes09]

The SFDR in dBc can be calculated as (see [Xila]).

$$\text{SFDR}_{\text{dBc}} = 20 \log \left( \frac{\text{Fundamental Amplitude (RMS)}}{\text{Largest Spur Amplitude (RMS)}} \right). \quad (2.26)$$

Figure 2.16 illustrates the SFDR in terms of dBFS and dBc.

### Total Harmonic Distortion

*Total Harmonic Distortion* describes the ratio of the RMS sum of the first five harmonic components (or aliased versions of them) to the RMS of the considered fundamental signal. [LV02]

### Effective Resolution Bandwidth

*Effective Resolution Bandwidth* denotes the frequency of the input signal, at which the SINAD has fallen by 3 dB ( $\cong 0.5$  bit in terms of ENOB) compared to the SINAD at lower frequency range. [LV02]

### Analog Input Bandwidth

*Analog Input Bandwidth* is the analog input frequency at which the power of the fundamental component is reduced by 3 dB with respect to the low-frequency value. [LV02] It is not to be confused with the maximal input frequency which the ADC is able to sample.

## Full-Linear Bandwidth

The *Full-Linear Bandwidth* is defined as the frequency at which the slew-rate of the SHA starts to distort the input signal by a specified value. [LV02] The slew-rate (SR) is defined as the rate of how much the voltage  $v$  changes over time  $t$ :

$$\text{SR} = \frac{dv}{dt} \quad (2.27)$$

A slew-rate of  $1 \text{ V}/\mu\text{s}$  for example means, that the output of the amplifier can not change more than  $1 \text{ V}$  over the course of  $1 \mu\text{s}$ . [Col21]

### 2.3.1.4. Time-Domain Dynamic Parameters

Time-Domain Dynamic parameters describe the deviation of the converter's behavior from the ideal one in time domain.

#### Aperture Delay

*Aperture Delay* (or *aperture time*) is defined as delay between the triggering of the converter (e.g. rising edge of the sampling clock) and the actual conversion of the input voltage into the digitized value. [LV02]

#### Aperture Jitter

*Aperture jitter* describes the sample-to-sample variation in aperture delay. Jitter can cause significant error in the voltage and decreases the overall SNR of a converter. Especially for high-speed ADCs jitter poses a limit in performance.

Assuming a full-scale sine wave  $V_{\text{in}}(t)$  as input signal with

$$V_{\text{in}}(t) = V_{\text{FS}} \sin(\omega t) \quad (2.28)$$

the maximal slope of this signal is then

$$\left. \frac{dV_{\text{in}}}{dt} \right|_{\text{max}} = \omega V_{\text{FS}} \quad (2.29)$$

Aperture jitter  $\Delta t_{\text{rms}}$  occurring during the sampling of this maximal slope produces the RMS voltage error

$$\Delta V_{\text{rms}} = \omega V_{\text{FS}} \Delta t_{\text{rms}} = 2\pi f V_{\text{FS}} \Delta t_{\text{rms}}. \quad (2.30)$$

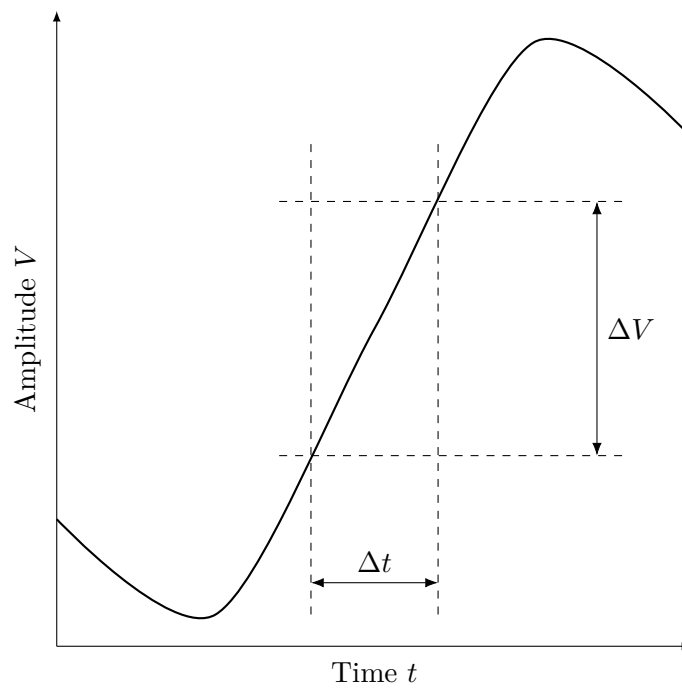
As variations in aperture time occur randomly, these errors behave like a random noise source. This way, a Signal-to-Jitter-Noise-Ratio (SJNR) can be defined as

$$\text{SJNR} = 20 \log \left( \frac{V_{\text{FS}}}{\Delta V_{\text{rms}}} \right) = 20 \log \left( \frac{1}{2\pi f V_{\text{FS}}} \right) \quad (2.31)$$

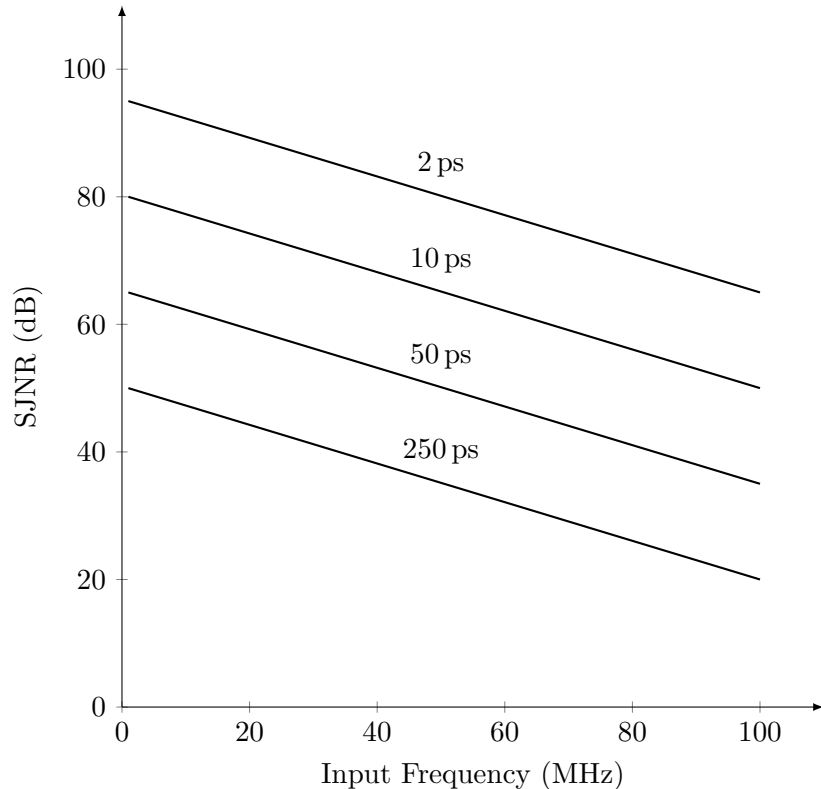
The voltage error due to jitter and the SJNR for different aperture jitter values are shown in Figure 2.17.

#### Transient Response

The *transient response* denotes the settling time of an ADC until full accuracy ( $\pm 1/2 \text{ LSB}$ ).



(a) Effect of aperture jitter



(b) SJNR for different aperture jitter values

**Figure 2.17.** Effects of aperture jitter on the output voltage and SJNR. Left: In time domain, Right: SJNR for different aperture jitter [LV02]

### 2.3.1.5. Sampling Theory

An ADC samples an analog signal with a sample frequency  $f_s$ . This frequency has to be chosen in such way, that the original signal can be fully reconstructed. The *Nyquist criteria* states, that in order to accurately reconstruct continuous signal limited to the bandwidth  $B$  (see [Pue15])

$$y(t) \circ \bullet Y(f) \quad \text{with} \quad Y(f) = 0|_{f>B/2} \quad (2.32)$$

it has to be sampled with a frequency  $f_s$  respecting

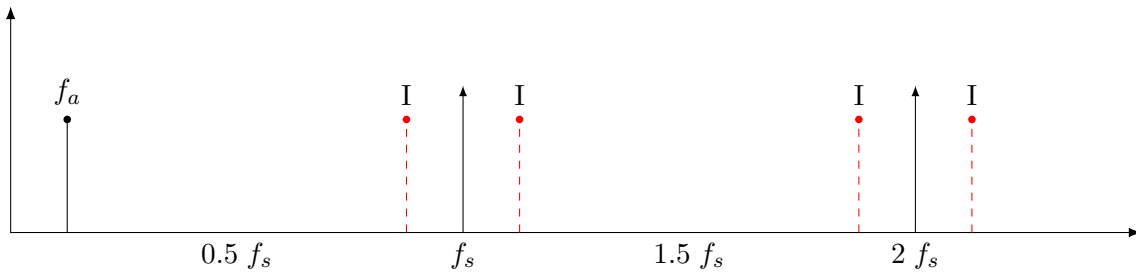
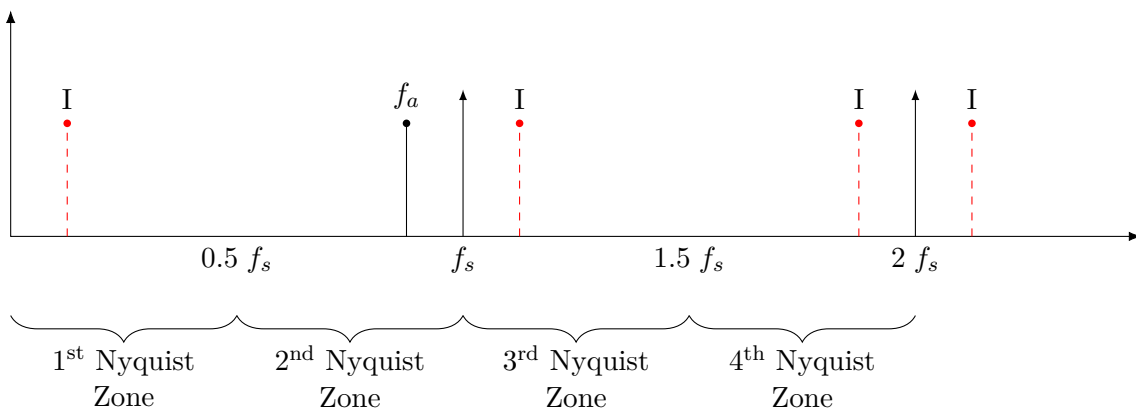
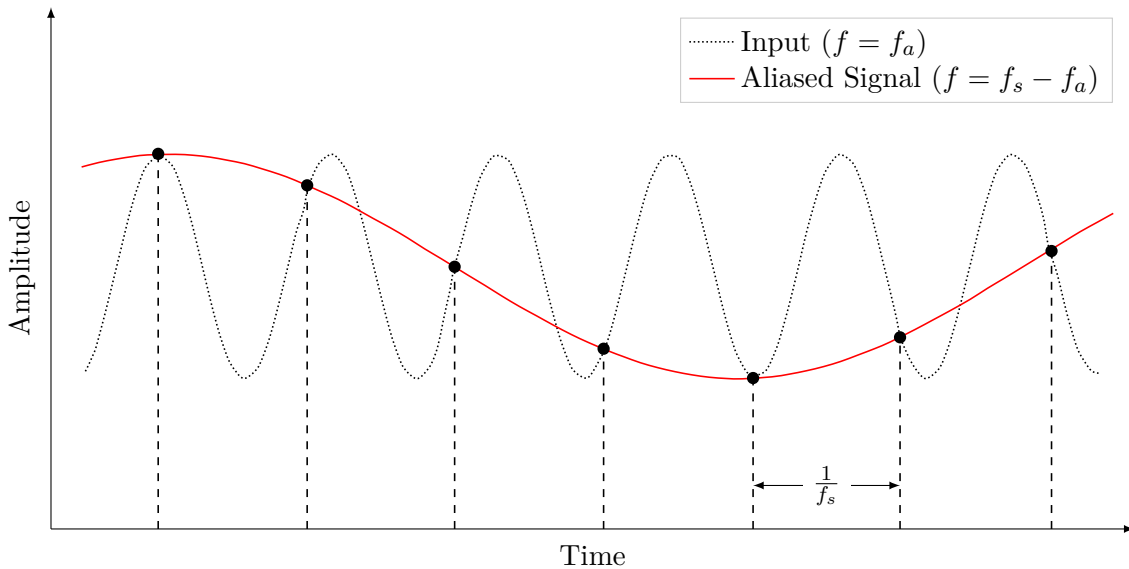
$$f_s > B \quad \text{or} \quad f_s > 2f_a, \quad (2.33)$$

with  $f_a$  being the highest frequency contained in the signal. [Kes05, Pue15]

The range from 0 Hz to  $f_s/2$  is also called *Nyquist-Zone* (or “1st Nyquist zone”, see Figure 2.18b). Violation of this rule leads to *aliasing*. The effects of aliasing are shown in Figure 2.18.

When a harmonic wave of the frequency  $f_a$  is sampled with the frequency  $f_s$ , this leads to periodic repetition of the signal spectrum in frequency domain in intervals of  $f_s$ , or “images” (see dashed, red frequency components in Figure 2.18a). If Equation 2.33 is respected, i.e.  $f_a$  lies inside the Nyquist bandwidth, there is no overlap with the images created by the sampling process.

Now assuming a signal frequency  $f_a \approx f_s$ , the sampling process leads to an image falling inside the Nyquist bandwidth (see Figure 2.18b). The reconstructed signal then lies at the frequency of this image which is much lower than the original frequency. The result of this *undersampling* is shown in Figure 2.18c. [Nyg28, Sha49, Kes05]

(a) Analog signal with frequency  $f_a$  sampled at  $f_s$  respecting the Nyquist criteria(b) Analog signal with frequency  $f_a$  sampled at  $f_s$  not respecting the Nyquist criteria

(c) Effect of aliasing in time domain

**Figure 2.18.** Analog signal with frequency  $f_a$  sampled at  $f_s$  respecting (Figure 2.18a) and not respecting (Figure 2.18b) the Nyquist criteria. Figure 2.18c shows the effect of aliasing in time domain. [Kes05]



### **3. Architecture Of The New Readout-System - THERESA**

This section is dedicated to describing the general concept of the new readout-system. The system was given the name THERESA and in the sections to follow, this name will be used to denote the new system.

First, a short overview of state of the art systems is given, including commercially available real-time oscilloscopes and Karlsruhe Pulse Taking Ultra-fast Readout Electronics (KAPTURE). This system was developed at the Institute for Data Processing and Electronics (IPE) at KIT specifically addressing the needs of THz diagnostics at KARA. The working principle of this system is explained in detail, as the new THERESA system is an evolution of the KAPTURE system.

Then, the architecture of the THERESA system itself is described.

#### **3.1. State Of The Art Readout-Systems**

In this section first a short overview over commercially available real-time oscilloscopes and their performance is given. Then, the KAPTURE system, which is in operation at KARA, is presented in detail.

##### **Real-Time Oscilloscopes**

Real-time oscilloscopes are defined by three key specifications: bandwidth, sample rate, and memory depth. Some examples of currently commercially available oscilloscopes are listed in Table 3.1. The acquisition time is given for the case of maximal sample rate. It can be calculated as

$$\text{Acquisition Time} = \frac{\text{Memory Depth}}{\text{Max. Sample Rate}} \quad (3.1)$$

As can be derived from the table, the acquisition time of such oscilloscopes is quite limited, not allowing for continuous sampling of fast input signals.

**Table 3.1.** Some example real-time oscilloscopes with (max.) key characteristics

Model	Bandwidth	Sample Rate	Memory Depth	Acquisition time
Keysight MXR608A	6 GHz	16 GS/s	1.6 GS	10 ms
Tektronix DPO70000SX	70 GHz	200 GS/s	1 GS	5 ms
LeCroy LabMaster 10-100Zi	65 GHz	160 GS/s	512 MS	3.2 ms

### 3.1.1. KAPTURE

KAPTURE (Karlsruhe Pulse Taking Ultra-Fast Readout Electronics) is a fast readout system developed at the IPE for THz diagnostics at KARA. It is designed to digitize the pulses generated by THz detectors at each electron bunch revolution, with a memory-efficient approach to acquire the detector signal on a bunch-by-bunch basis (sampling only the pulses themselves). The system is able to sample pulses with a Full Width At Half Maximum (FWHM) between a few tens to a hundred picoseconds with a minimal sample time of 3 ps. [CAB<sup>+17]</sup>

To showcase the revolution of this DAQ system, the general architecture and concept is explained with the first version of KAPTURE. Then, the improved version Karlsruhe Pulse Taking Ultra-fast Readout Electronics 2 (KAPTURE-2) is presented. At the end, being a further evolution of these two versions, the architecture of THERESA is explained.

#### General Concept

The system consists of two parts: the sampling front-end card and a FPGA readout card. In Figure 3.1 the setup for THz radiation measurements with KAPTURE is shown.

The incoming radiation is fed into a detector, which converts the incident photons into an electrical signal. This signal is then amplified in a wide-band Low-Noise-Amplifier (LNA). A wideband lossless power splitter, developed at IPE, splits the detector signal into four identical signals, which are then propagated to the sampling front-end card. The card consists of four parallel sampling channels with adjustable sampling time. Each channel contains a THA and an ADC. This card is connected to a read-out card by a high-speed and high-density connector. The FPGA sets the sampling time for each individual sampling channel and reads, processes and sends all acquired data to a Central Processing Unit (CPU)/Graphics Processing Unit (GPU) cluster for further processing. [CBC<sup>+14]</sup>

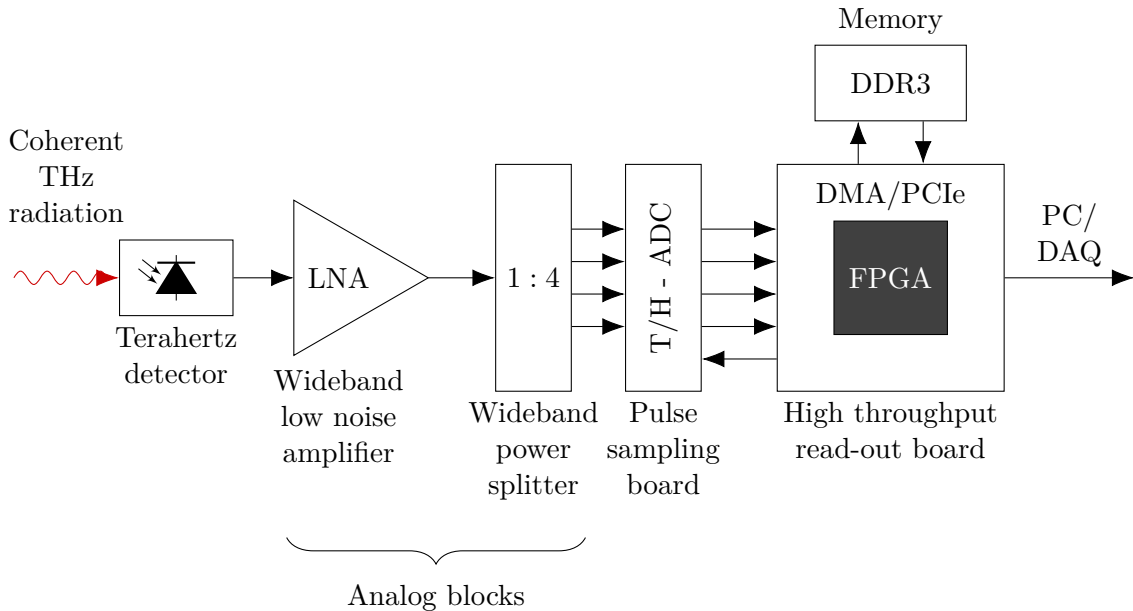


**Figure 3.1.** THz radiation measurement setup with KAPTURE (redrawn from [CBC<sup>+</sup>14])

### Analog Front-End

Due to the high bandwidth nature of the detector signal, the analog front-end of the system has to be wideband as well to be able to sample the signal with picosecond resolution.

The used LNA is based on a commercial GaAs Microwave Monolithic Integrated Circuit (MMIC) which operates from DC to 50 GHz. It is needed to compensate the insertion loss<sup>1</sup> of the following power-splitter stage. Classical power-splitters are not intrinsically wideband (see [CBC<sup>+</sup>14]). For that reason, a wideband power-splitter was developed at IPE which fulfills the bandwidth requirements. The designed power-splitter works up to 100 GHz with an insertion loss of 8 dB (at 100 GHz) and a return loss<sup>2</sup> of about 20 dB at 50 GHz. [CBC<sup>+</sup>14] A photo of the power-splitter is shown in Figure 3.2.

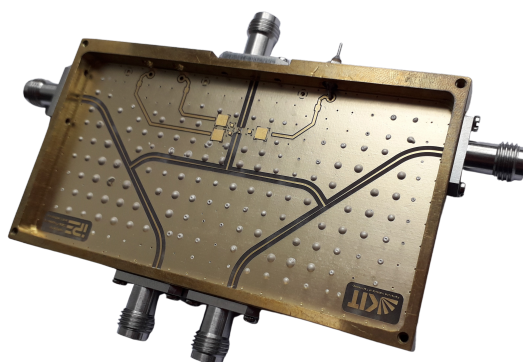


**Figure 3.2.** Photo of the power-splitter developed at IPE

<sup>1</sup>Insertion loss is the loss of signal power which occurs, when a signal passes through a component.

<sup>2</sup>Return loss is the loss of signal power due to reflection by a discontinuity in the transmission line.

## Sampling Board

The architecture of the front-end board with the power-splitter is shown in Figure 3.3.

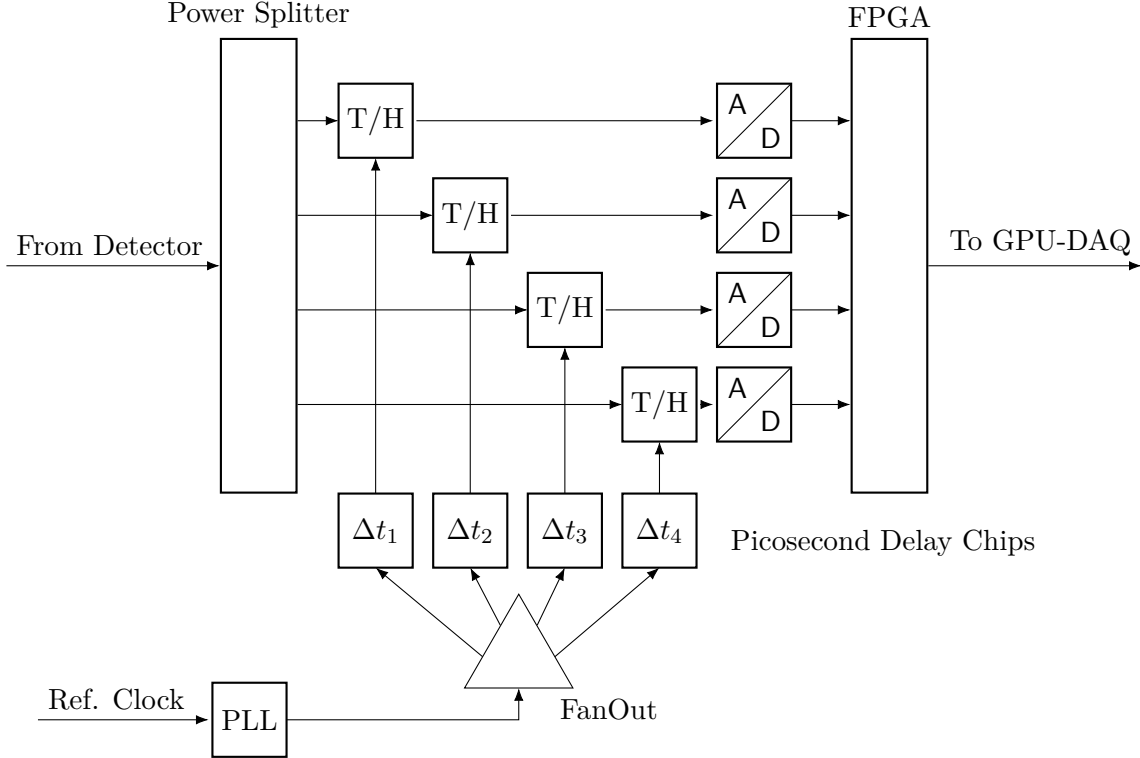


**Figure 3.3.** General architecture of the KAPTURE (v1) front-end sampling card (cf. [CAB<sup>+</sup>17, p.2])

The power-splitter splits the incoming signal into four identical signals, which are then fed into four parallel channels, consisting of a respective THA unit and a 12-bit ADC sampling at 500 MS/s. The sampling time of each unit can be adjusted individually with a delay chip with a resolution of 3 ps (maximal delay range: 100 ps). The delay chips are programmed with the FPGA on the readout card. The clock signal is provided by KARA, which is cleared from jitter by a Phase-Locked-Loop (PLL). This ensures the synchronization of the ADCs with the RF system. The cleaned clock signal is distributed to the delay chips via fan-out buffer [CAB<sup>+</sup>17]. In this way, the pulse can be “locally sampled” by adjusting the different delay with a maximum rate of 330 GS/s possible. A simplified representation of the local sampling of the signal is shown in Figure 3.4. The plot shows on the left the sampling of the signal for KAPTURE and on the right for KAPTURE-2 (described below). The sampling points  $S_n$  are acquired by setting the respective delay  $\Delta t_n$  of the sampling times.

## GPU-DAQ System

The sampling system produces a large amount of data. In order to keep a continuous data acquisition the necessary bandwidth is

$$12 \text{ bits} \cdot 8 \text{ samples} \cdot 1 \text{ GHz} = 96 \text{ Gb/s} \quad (3.2)$$

To ensure high data throughput, a high-speed PCI Express (PCIe) readout card was developed (called “High-Flex”) was developed. This card receives the samples and tags them with the respective bunch identification. The data is then sent to a GPU using a

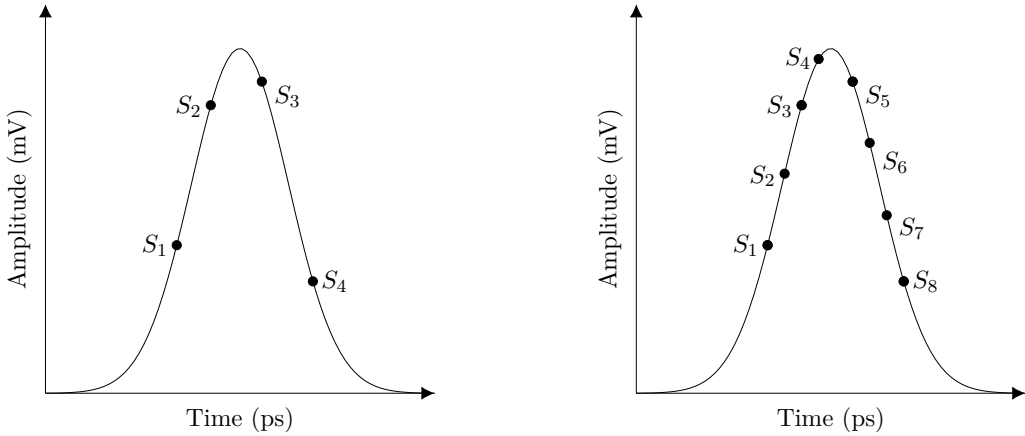


**Figure 3.4.** Sample points  $S_n$  acquired by setting the sampling delay times  $\Delta t_n$  accordingly. Left plot shows pulse sampled by KAPTURE v1, right plot by KAPTURE v2

PCIe connection based on direct FPGA-GPU direct memory access architecture. The GPU node reconstructs the pulse based on the given sampling points and calculates the amplitude and pulse arrival time. It also performs an online FFT for frequency analysis. To store the data temporary before it is sent to the DAQ system, a large Double Data Rate Gen 3 (DDR3) memory device is used, as seen in Figure 3.1. [CAB<sup>+</sup>17]

### 3.1.2. KAPTURE-2

The first version of KAPTURE has a limitation concerning the number of sampling points per pulse and does not allow to sample the baseline of the detector. Analyzing the baseline however is very important, as it is changing slightly and affects the pulse amplitude of the bunch. Due to this distortion, calculating the correlation between bunches was limited. For this reason, a second version of KAPTURE was designed in order to overcome these limitations. The PLL on the sampling board allows for synchronization between two or more PLLs located on different boards. With this feature, the sampling time of two boards can be synchronized and in this way extend the number of sampling points beyond four. A comparison of the sampling concepts is shown in Figure 3.5.

In KAPTURE-2, two front-end boards can be connected to directly sample the pulses with up to eight sampling point at the pulse repetition rate 2 GHz. Alternatively, the system can sample the pulse and the baseline between two consecutive pulses with a constant pulse rate up to 1 GHz (see Figure 3.5b). In this way, the read-out card can calculate the correct amplitude of the pulse and send it to the GPU for further processing [CAB<sup>+</sup>17].

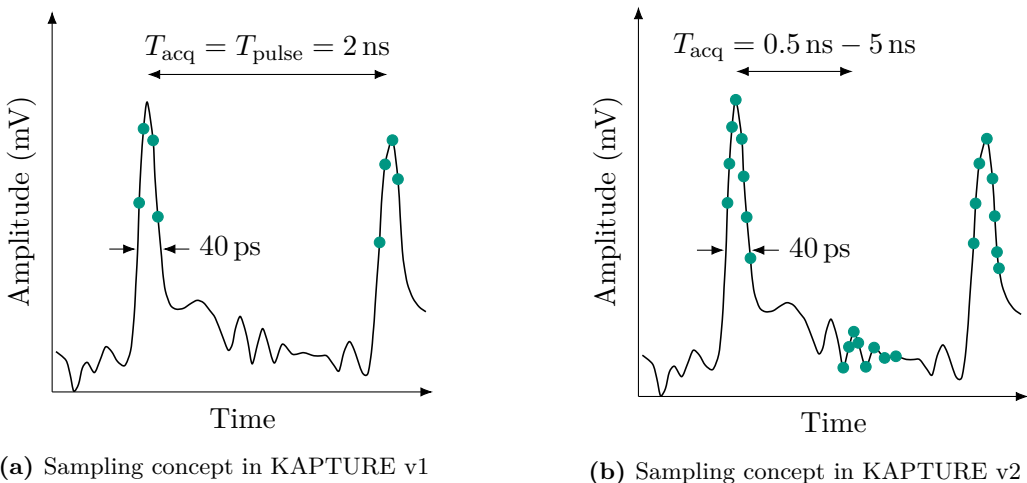


**Figure 3.5.** Comparison between the sampling concepts of KAPTURE v1 and KAPTURE v2

Figure 3.6 shows a photo of the system setup of KAPTURE-2.

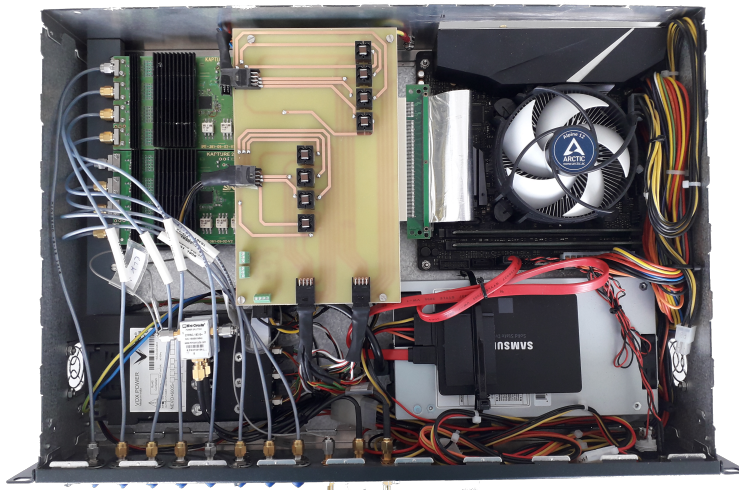


**Figure 3.6.** Photo of the KAPTURE-2 setup

### 3.2. Proposed Architecture for THERESA

In this section the architecture for the THERESA system is described. The system consists of the optical time-stretch setup, which stretches the analog input signal and the photodetector in order to convert the optical signal into an electrical one. This signal is sampled by a front-end sampling card, which is mounted on a back-end readout card, which processes the acquired samples.

#### Optical Part

For the optical time-stretch setup, a femtosecond Ytterbium-doped fiber laser from *MENLO GmbH* is used. The emitted pulses have a bandwidth of 50 nm and a total output average power of 40 mW. The photodetector used is an InGaAs photodiode from *Discovery Semiconductors* with a 20 GHz bandwidth.

##### 3.2.1. Front-End Sampling Card

The concept of the front-end sampling card is based on and an evolution of the concept used in the KAPTURE system.

The incoming signal is split into 16 identical signals, each leading to the respective sampling channel on the sampling board. These sampling channels consist of a high bandwidth (18 GHz), low noise THA and an ADC, which is integrated into the readout card. The sampling clock to these THAs is provided by respective programmable delay chips. In this way, a time interleaving technique (described below) can be implemented by programming the delay chips accordingly. The main clock is provided by a main PLL, which cleans the reference clock coming from the system in which the sampling system is integrated. Figure 3.7 shows the general schema of the sampling system, reduced to four channels for presentation purposes.

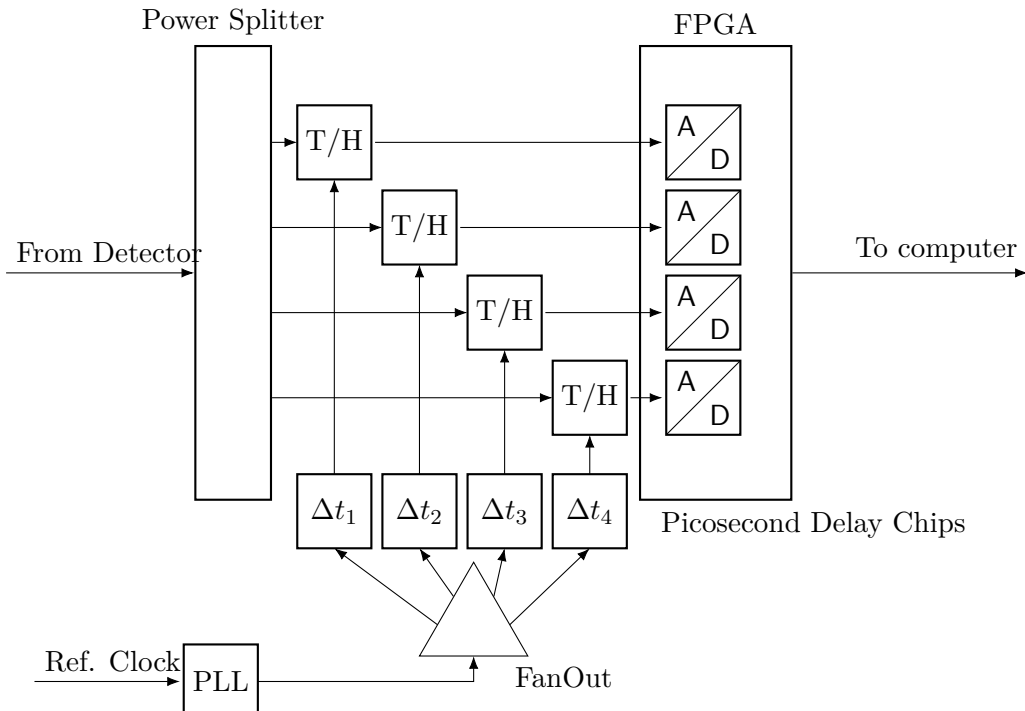


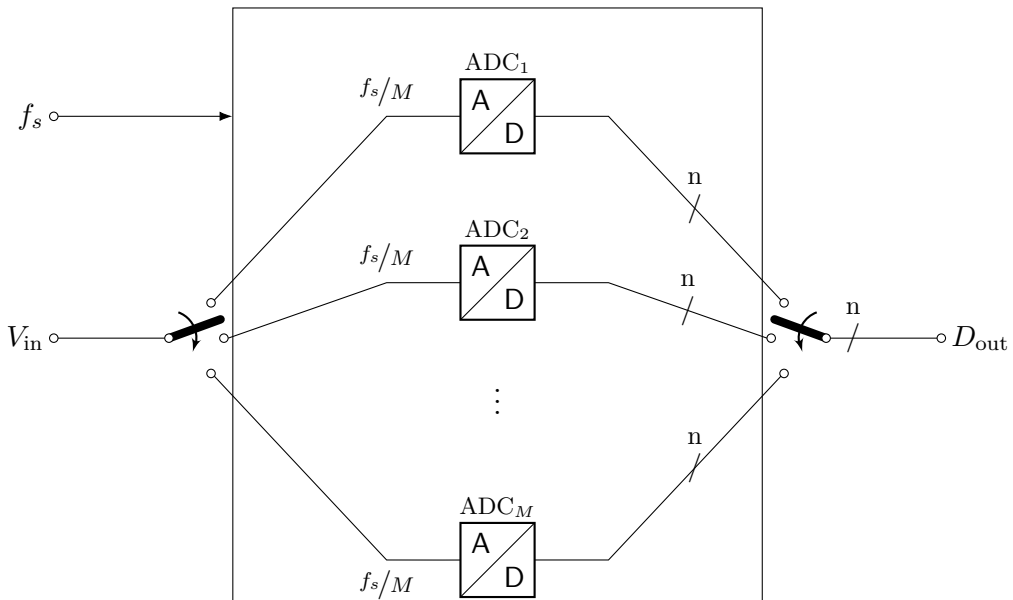
**Figure 3.7.** General architecture of the THERESA sampling card with power splitter and ADCs. For presentation purposes only four of the sixteen channels are shown.

### 3.2.1.1. Time Interleaving

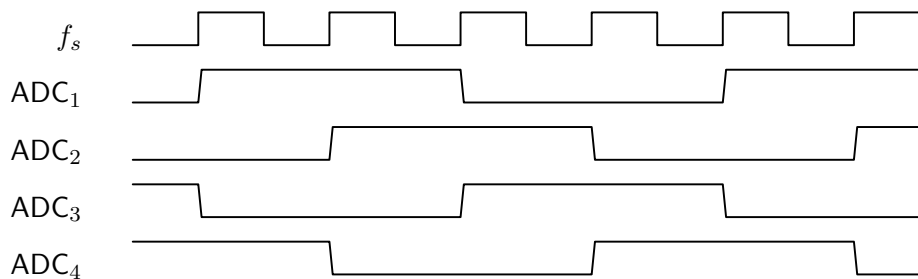
In order to increase the sampling rate, the so called time-interleaving technique is used. In this section, first the fundamental theory about this technique is given. Then, the implementation in the new system is described.

#### Theory

In the *Time Interleaving* technique multiple ADCs are used in such way that allows to sample data at a faster rate than the respective sample rate of each individual ADC. The principle is based on time-multiplexing an array of  $M$  identical ADCs (see Figure 3.8a), each operating at a sampling rate of  $f_c = f_s/M$  individually. The sampling times of the ADCs are shifted in phase as shown in Figure 3.8b with the example of 4 time-interleaved ADCs. At time  $t_0$  the first ADC starts converting the input signal  $V_i(t_0)$ , after a defined time delay  $\Delta t_i$  the second ADC samples and converts  $V_i(t_0 + t_i)$ , the third converts  $V_i(t_0 + 2t_i)$  and so on. After the  $M$ -th ADC has sampled the signal  $V_i(t_0 + (M - 1)t_i)$ , the whole cycle starts anew with the first ADC. [MR15] An example for such a cycle for 4 ADCs is shown in Figure 3.8b.



(a) An array of  $M$  time interleaved  $N$ -bit ADCs [MR15]



(b) Clocking Scheme for interleaving 4 ADCs

**Figure 3.8.** Array of  $M$  time interleaved ADCs and clocking example for  $M = 4$

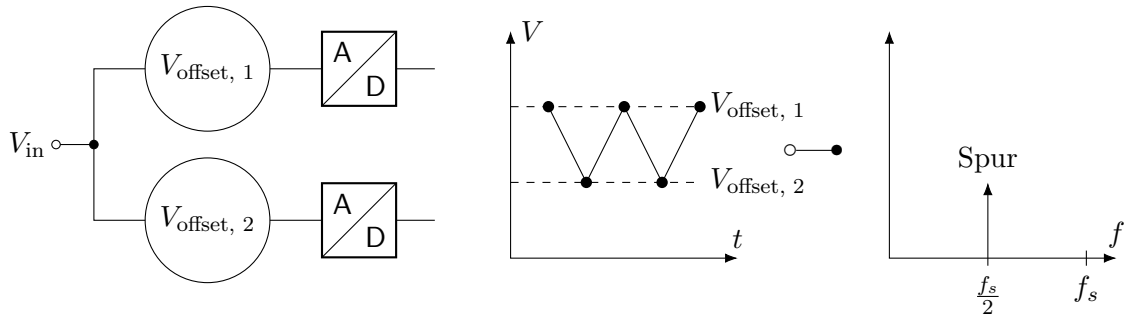


**Figure 3.9.** Offset-mismatch in Interleaving [Har19]

### Challenges

When using the time-interleaving method, spurious components appear in the spectrum. There are several reasons for this which are described in the following.

The first reason is the *offset mismatch* between den ADCs. Each ADC is characterized by a DC offset. Considering as example an interleaving structure with two ADCs and a constant input voltage: when the samples are acquired back and forth between the two ADCs, the resulting output will switch back and forth between two levels due to the different offset levels of the ADCs. This output switches at the frequency  $f_s/2$ . Therefore this introduces spurious harmonic components at the frequency  $f_s/2$  in the spectrum (see Figure 3.9). The magnitude of the spur depends on the offset difference between the ADCs. [Har19]

Besides of the offset also the gain of the converters can be mismatched. This *gain mismatch* has a frequency component to it, which in case of an input signal of the frequency  $f_{in}$  results in a spur at  $f_s/2 \pm f_{in}$  (see Figure 3.10). [Har19]

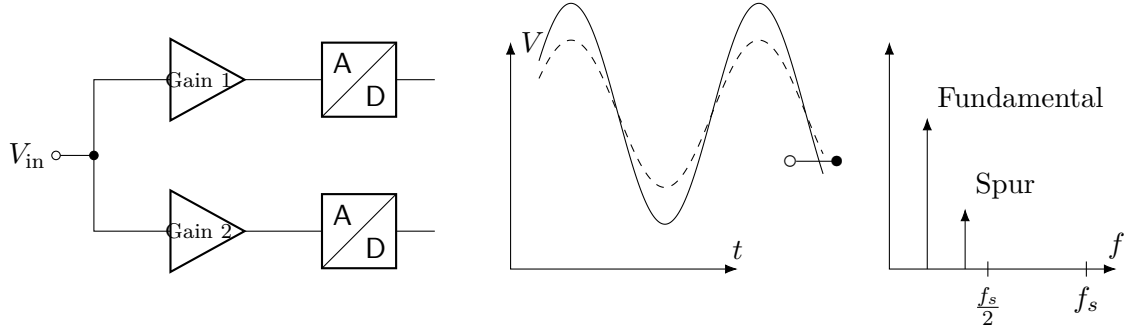


**Figure 3.10.** Gain-mismatch in Interleaving [Har19]

In the time domain, *timing mismatch* due to group delay in the analog circuitry of the ADC and clock skew<sup>3</sup> can occur. The group delay in analog circuitry can vary between the converters. The clock skew has on the one hand an aperture uncertainty component at each of the ADCs. On the other hand it has a component related to the accuracy of the clock phases, which are input to each converter. [Har19] This mismatch also produces a spurious component at  $f_s/2 \pm f_{in}$  (see Figure 3.11).

<sup>3</sup>Difference in arrival time of the clock signal at different components.

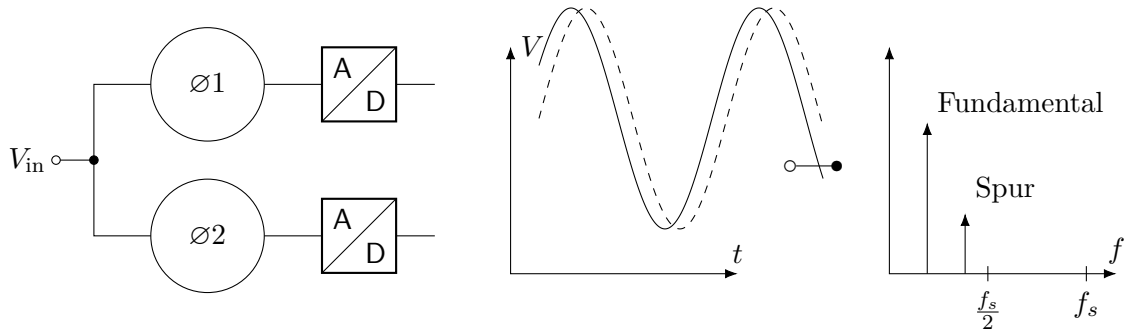


**Figure 3.11.** Timing-mismatch in Interleaving [Har19]

The last possible mismatch is the *bandwidth mismatch*, which contains both gain and phase/frequency component (see Figure 3.12). Due to bandwidth mismatch, different gain values at different frequencies can be seen. An additional timing component causes different delays for signals at different frequencies through each ADC. Just like gain and timing mismatch, the bandwidth mismatch causes a spur at  $f_s/2 \pm f_{\text{in}}$ .

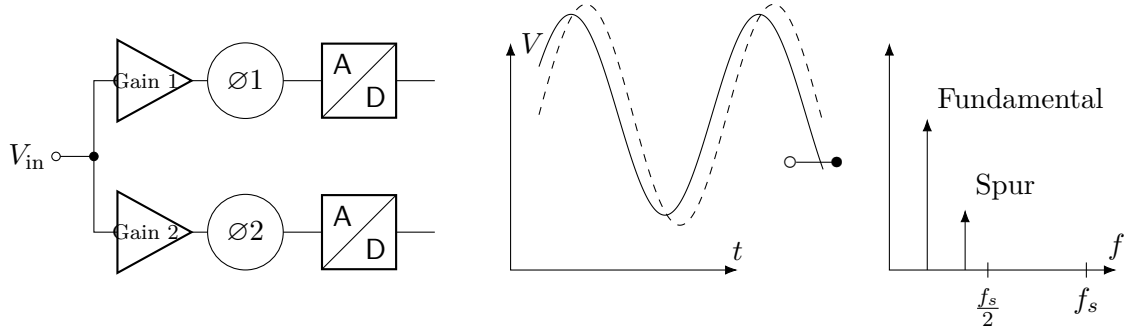


**Figure 3.12.** Bandwidth-mismatch in Interleaving [Har19]

In order to compensate for the presented mismatches, a proper characterization of the ADCs is crucial. The characterization is required in order to account for all systematical errors in the ADCs and to reduce the spurious components in the spectrum. For this purpose, a circuit on the THERESA sampling board is foreseen, in order to provide the possibility to generate test signals from the readout card.

### 3.2.1.2. Implementation

On the selected readout card for THERESA, 16 ADCs with a sampling rate up to 2.5 GHz are present. In order to implement the time-interleaving method, an appropriate delay step size for the sample time has to be calculated. To calculate the maximal step size possible can be calculated as follows: The ADCs on the read-out card sample at a maximal sample rate of 2.5 GS/s, meaning during the time

$$t_s = \frac{1}{2.5 \text{ GS/s}} = 400 \text{ ps} \quad (3.3)$$

all 16 ADCs have to sample the signal one time. This means, a delay step can not be greater than  $400 \text{ ps}/16 = 25 \text{ ps}$ . With this method, the maximal achievable sampling rate of the card is  $16 \cdot 2.5 \text{ GS/s} = 40 \text{ GS/s}$ .

On the selected readout card, sampling clock signals are not propagated individually to the respective ADCs. The converters are grouped together into tiles, each tile

containing four converters. One single reference clock signal is propagated to all tiles. To implement the optimal time-interleaving method with this card, four individual sampling clocks to all tiles shifted by 90° would be necessary. Analyzing the schematic of the readout board revealed however, that only two individual sampling clocks can be provided to the card.

Therefore, another approach needs to be considered. Figure 3.13 shows qualitatively the concept of the time-interleaving method implemented in this design. The main 1 GHz clock is propagated to the THAs, which are in hold-mode when the clock signal is HIGH and in track-mode when the clock signal is LOW. As shown in Figure 3.13 the clock signal to each THA is provided with a respective delay. The maximal delay step size to cover the whole period of the clock is calculated by:

$$\frac{1 \text{ ns}}{16 \text{ channels}} = 62.5 \text{ ps} \quad (3.4)$$

In some way, this implementation can therefore also be regarded as time-interleaving, as each THA holds a different sample point in time, which can then be converted by the ADCs. The two sampling clocks, indicated with “ADC<sub>1</sub>” and “ADC<sub>2</sub>”, need to be phase-shifted by 180°. In this way, an alternate clocking of the ADCs is made possible. As can be derived from the diagram, only the four respective ADC channels should be considered for signal conversion during one sampling point.

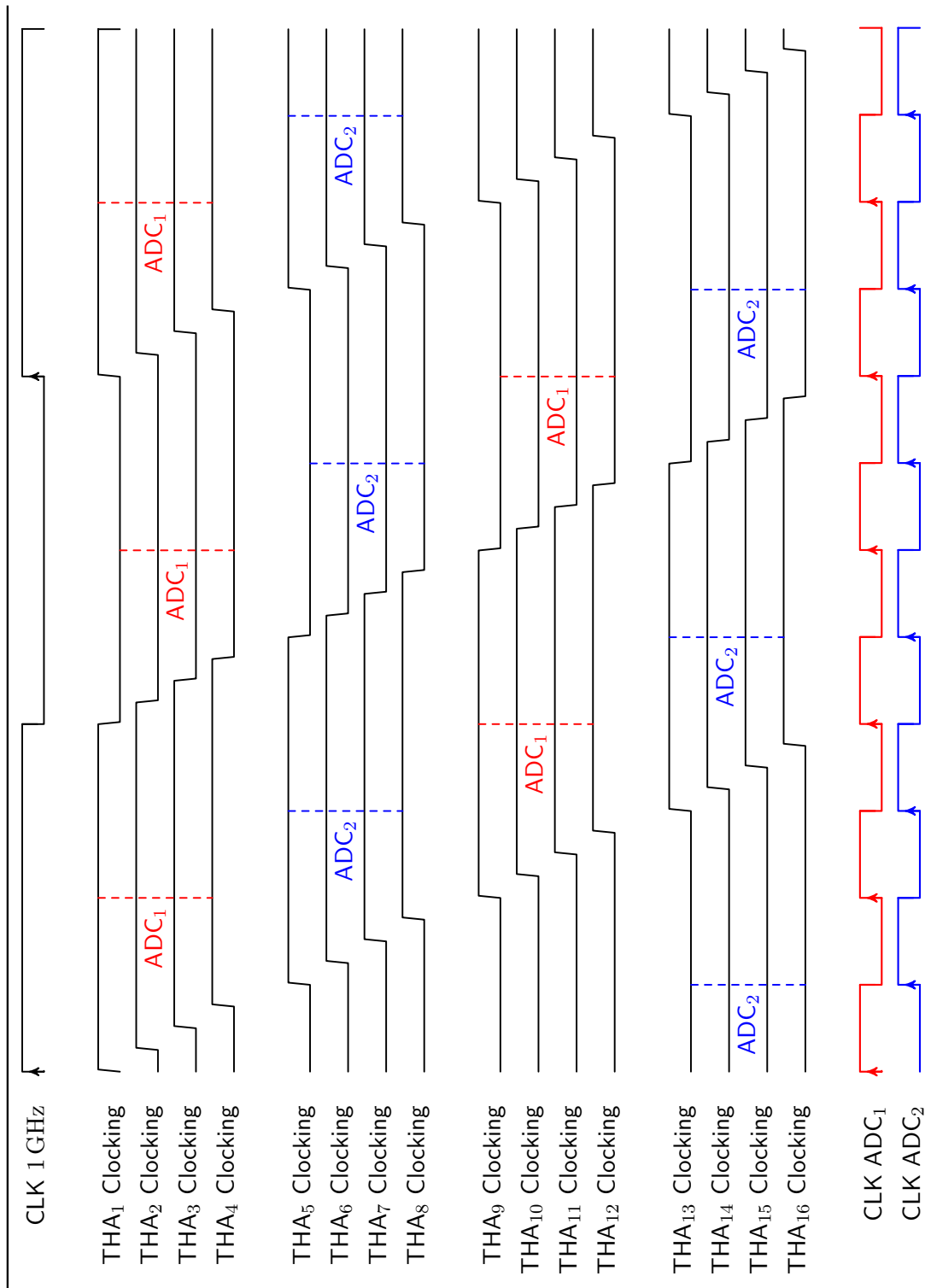


Figure 3.13. THA Timing diagram. Shows the clocking of the THA (HIGH = hold mode, LOW = track mode). Dashed line represents the sampling of the ADC.

### 3.2.2. Readout Card

The most important points to consider when choosing the readout card is its capability to handle high data-throughput, provide the possibility for user-defined firmware and control of the system. This flexibility is provided by FPGA-based System-On-Chips (SoCs), which also integrate the required high-speed peripheral connections for data transfer. An important point for THERESA is also to integrate the ADCs inside the SoC. The reason for this is illustrated in Figure 3.14. In order to fulfill the requirements, the system would need a processing unit, an FPGA and a number of data converters (ADC/DAC). Realizing this in discrete components results in a higher footprint, than integrating every component inside one Integrated Circuit (IC).

Integration of the necessary components inside an IC also drastically reduces the complexity of the sampling board. Implementing the data converters in a discrete way would result in a high number of interfaces or connections, especially for a high ADC resolution, making expensive high pin count connectors necessary. Integrating the converters inside the SoC therefore resolves these challenges.

The currently only commercially available system, meeting the mentioned requirements, is the Xilinx ZU49DR Zynq Ultrascale+ Radio-Frequency System-On-Chip (RFSoC). This SoC integrates 16 high-speed data converters (ADCs and DACs), ARM processor cores and programmable logic (the FPGA). An evaluation card, containing all necessary peripherals (optical interfaces, Universal Serial Bus (USB), ...) and integrating the RFSoC, was chosen for the implementation of the THERESA system. The card is described in detail in chapter 5.

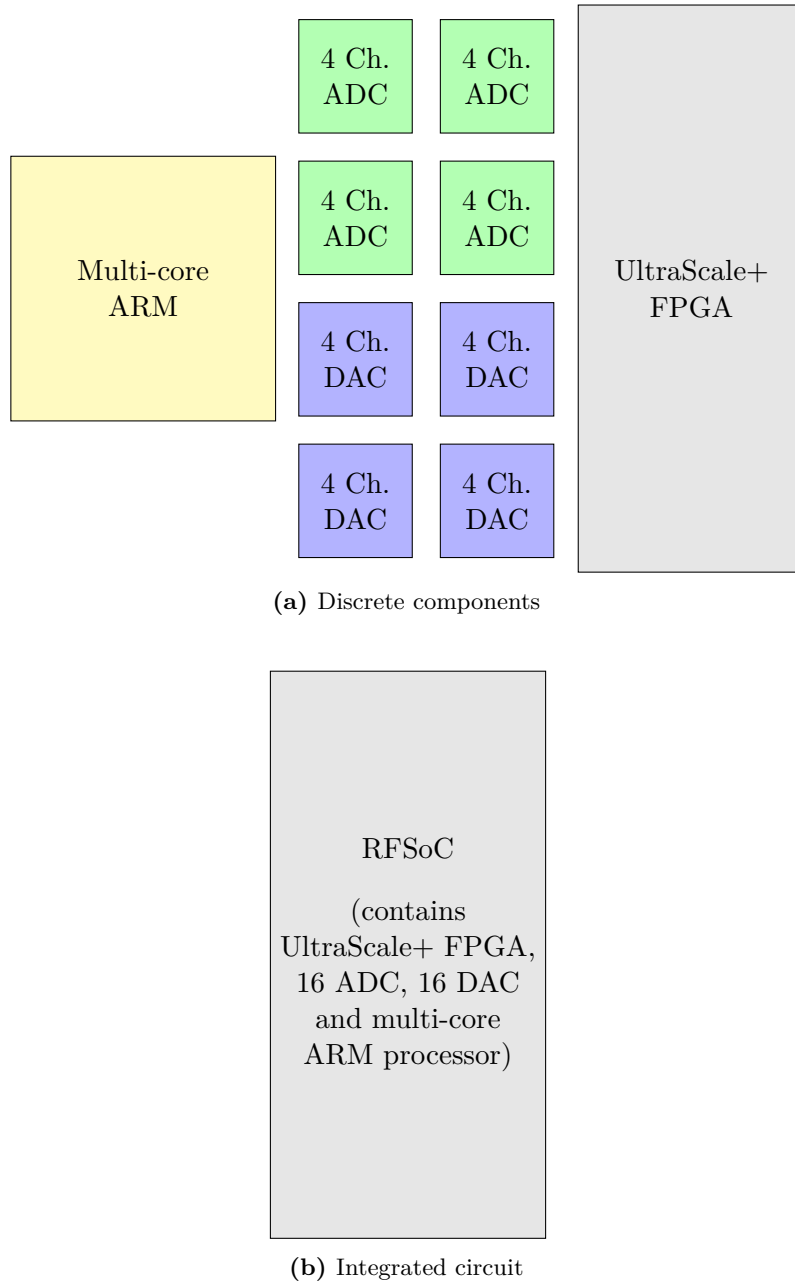


**Figure 3.14.** Footprint of discrete components vs. footprint of IC integrating the components

## 4. Design Of The Front-End Sampling Card

In this chapter the process of designing the front-end sampling card is described. Designing a Printed Circuit Board (PCB) is a two step process: circuit design and layout design. In this thesis, the software used to cover both of these steps is *PADS xDx Designer* (for schematic capture) and *PADS Layout/Router* (for PCB layout design) from *Mentor Graphics* (subsidiary of Siemens).

### 4.1. Schematics

Without knowing which components are needed and how they are interconnected, it is impossible to manufacture any board, no matter how high or low the level of complexity is. The schematic is a graphical documentation of an electrical circuit, showing the needed components and their interconnections using standardized symbols. Furthermore, a schematic provides a starting point for automatic placement and routing, i.e. where the components are placed and how they are connected on the physical PCB. The placement and routing is done with the layout design tool. During the creation of the schematics, the following points have to be considered:

- Deciding which components are needed and what the requirements on the performance are. Especially for high-speed components carefully considering specifications like signal rise and fall times, jitter, skew, etc. is crucial to achieve the overall expected performance.
- Keeping in mind how many pins are available for high- and low-speed peripheral connections, control signals, etc. Many components have an interface for programming (e.g. Serial Peripheral Interface (SPI)) which requires several pins that need to be connected to the controlling unit. Especially for boards with a lot of components this can quickly become an issue.
- Checking the signaling interfaces of the components. Additional circuitry might be needed for interfacing between two different components. Some signaling interfaces, like Low Voltage Differential Signaling (LVDS), require a specific voltage level, which might result in the need of voltage level translators.
- Keep in mind the different common mode voltages at input/output pins of different components and placing decoupling capacitors if needed.
- Consider placing additional filtering for power supplies in order to reduce noise and PCB, as well as recommended filters from manufacturers of the components.
- Choose suitable type and amount of power supplies/voltage regulators.
- Keep in mind the packaging/Size of the components. The size of the component is important, as space on the board is limited. The package introduces additional capacitive/inductive parasitics, which can be a problem for precise filtering circuits.

- Consider the power dissipation of the components. Components like voltage regulators might need coolers or heat sinks. These additional elements might not pose any problems for components which are located on the top side of the board. However, components on the bottom side might create a space issue, if the designed PCB should be mounted on another board.
- For mixed-signal boards, i.e. boards containing digital and analog signal paths, analog and digital ground should be separated. For ICs like THAs or ADCs, where both analog and digital signals are present, connecting the grounds via appropriate components needs to be considered.
- Check if the components are still available and if they can be delivered in the given project time.

This list is certainly not complete, but provides an overview over the most important points which need to be taken into account during design. Decoupling techniques and separation of analog and digital ground are explained a bit more detailed, being very important and crucial steps for design of high-performance PCB.

### Decoupling techniques

Probably the most important part in schematics design is proper decoupling of power supplies, as ICs require a stable voltage on the power supply pins for optimal performance. Any ripple<sup>1</sup> or noise can substantially degrade the performance of the ICs, i.e. by decreasing the noise margin. *Noise margin* defines the difference between the useful signal and noise. A sufficient noise margin is necessary to guarantee that the output signal will still be correctly interpreted, even if some noise is added to the signal. Variation on the power supply produces also a variation on the signal and can therefore lead to a smaller difference between signal and noise.

Usually, manufacturers give information about proper power supply decoupling circuits for their component in the data sheet. If this is not the case, there are basic rules of thumb which can be followed to ensure proper decoupling. [Anac]

Basically, two types of voltage variations on the power supply pin can be distinguished: low frequency and high frequency variation. Low frequency variation occurs for example due to devices (or parts of them) being enabled/disabled or in the event of data traffic or data processing. The current draw during these occurrences cannot be compensated immediately by the voltage regulator providing the supply voltage, which leads to drops in the voltage level. Time frames of this variation vary in the range of milliseconds up to days. High frequency variation results from switching events in the device, occurring in the range of the clock frequency and the corresponding harmonics up to about 5 GHz. Spikes due to Electro-Magnetic Interference (EMI) are also a source of high frequency variation and need to be compensated for. [Xile]

Ideally, one capacitor, which acts as a low-pass filter, should be enough to mitigate these variations. A real capacitor however has parasitics and thus can in general not be modeled by a “pure” capacitive behavior. This reduces the filtering performance at high frequencies. Additional resistances and inductance need to be considered [Anac]:

- A parallel resistance  $R_P$ , which shunts the nominal capacitance ( $C$ ), representing insulation resistance or leakage.
- A series resistance  $R_S$ , or Equivalent-Series-Resistance (ESR), which represents the plates and the leads of the capacitor.

---

<sup>1</sup> Ripple is additional Alternating Current (AC)-voltage (of small amplitude) superimposed on a the general voltage level.

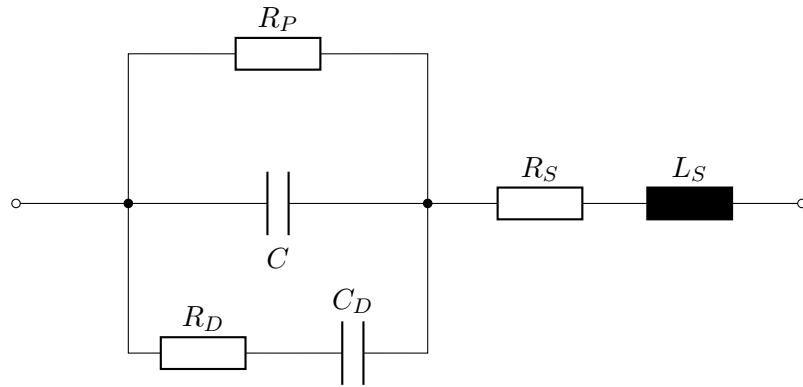


**Figure 4.1.** Equivalent circuit of a real capacitance (redrawn from [Anac])

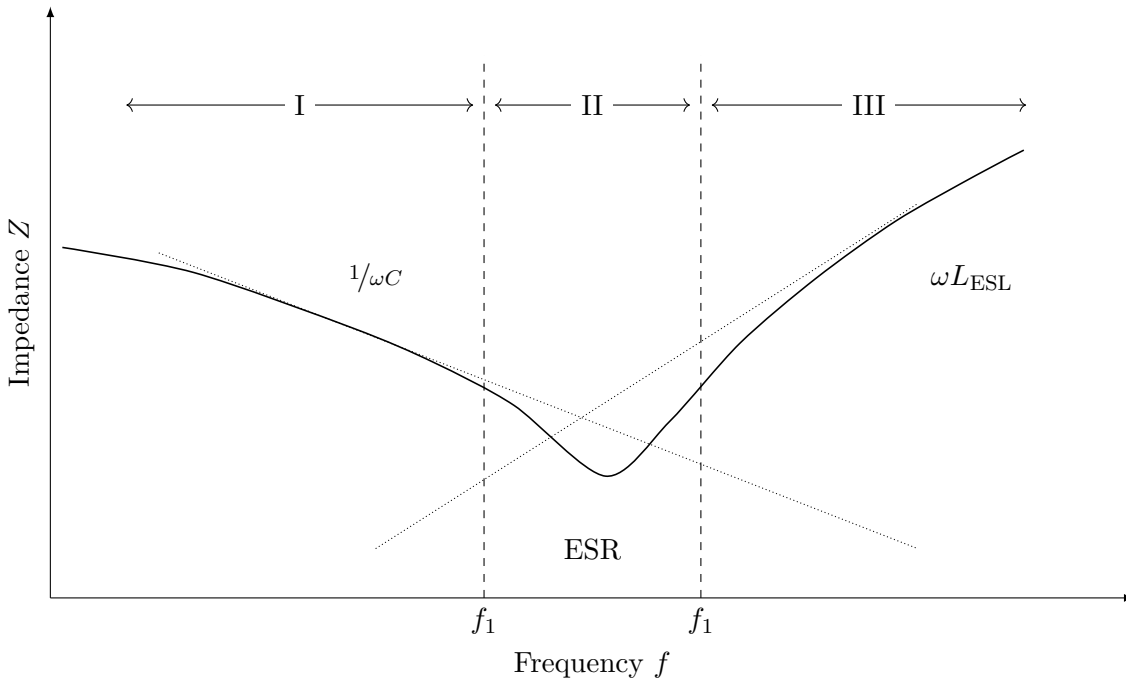


**Figure 4.2.** Qualitative impedance response of a real capacitance [DK20]

- A series inductance  $L_S$ , or Equivalent-Series-Inductance (ESL), that models the inductance of the plates and leads of the capacitor.
- A parallel resistance and capacitance,  $R_D$  and  $R_C$ , which model the effect called dielectric absorption. This denotes the phenomenon, that a capacitor which has been charged for a long time, does not fully discharge when briefly discharged. Dielectric absorption can be detrimental for high-precision use-cases, for power supply decoupling this effect doesn't have to be considered.

Consideration of all these effects leads to the equivalent circuit shown in Figure 4.1. It can be seen that this forms a *RLC* circuit, meaning the capacitor will not have the ideal behavior over the whole frequency range. In fact, a real capacitor shows an impedance response as seen in Figure 4.2, which resembles one of a band stop, rather than a low pass. Typical capacitive behavior is seen in region (I). Region (II) shows the influence of the ESR, which is why there is a residual impedance at the lowest point. Region (III) showcases the effect of the ESL. To extend the capacitive behavior over a wider frequency range, at least two capacitors are placed.

To deal with the low frequency variation, a large capacitor (typical values: 10  $\mu\text{F}$  to 100  $\mu\text{F}$ )

is placed next to the component, not more than 5 cm away. The role of this capacitor is to be a charge supply for the instantaneous needs of the device, i.e. keeping a constant voltage level until the slower control loop of the voltage regulator can compensate for the changed current draw. [Anac] This capacitor is also called *decoupling capacitor*.

Another, small capacitor (typical values: 0.01  $\mu\text{F}$  to 0.1  $\mu\text{F}$ ) is placed as close as possible to the power pins of the component. This capacitor should bypass (therefore also called *bypass capacitor*) the high frequency variation on the power supply line. [Anac]

To cover a larger frequency range, multiple capacitors can be used.

All capacitors should be connected through vias or short traces to a large area, low impedance ground plane. Vias on a PCB are used to connect different layers, a plane is an uninterrupted area of metal covering the whole (or part) of a PCB layer (basic PCB structures are also explained in section 4.2). Connecting capacitors in this way minimizes the inductance due to connection traces. [Anac]

An optional ferrite bead in series with the supply pin keeps external high frequency from the device and the noise generated inside the component from the rest of the board. [Anac]

#### 4.1.1. Connectors

The number and type of connectors is primarily defined by the read-out card, on which the sampling board is mounted. The different connector types serve different purposes, which can be organized into three categories.

##### Digital Control Signals

For digital control (i.e. SPI, enable signals, ...) and clocking signals a VITA 57.4 FMC+ connector from *SAMTEC* is used (see Figure 4.3).

FPGA Mezzanine Card (FMC) is a standard defined by VMEbus International Trade Association (VITA) to provide a standard mezzanine card<sup>2</sup> form factor, connectors and modular interface to a FPGA located on a base board (carrier card). [See09] The FMC+ standard extends the pin count and throughput of the present high-speed interfaces. An assembly drawing of the FMC+ connector is shown in Figure 4.3.

The FMC+ connector provides 560 pins arranged in a  $14 \times 40$  array, 80 of which are additional high-speed interfaces, located on either side of the connector (therefore this connector type is also called High Serial Pin Count Extension (HSPCe) connector, as opposed to the HSPC connector which doesn't have additional rows). For user-defined purpose 160 pins are available. They can be used as single-ended or differential pins.

<sup>2</sup>A PCB which is plugged on a plug-in board. [PCM]

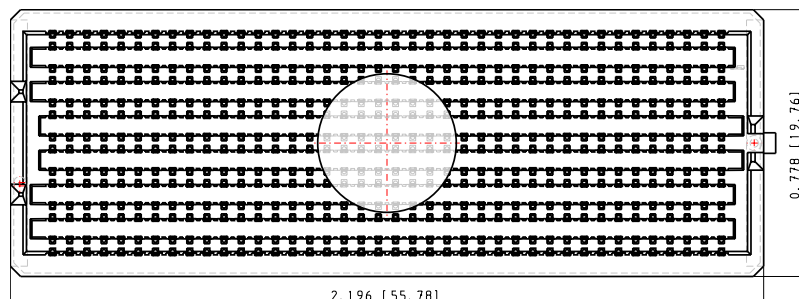


**Figure 4.3.** Part drawing of FMC+ connector [SAM]

**Table 4.1.** Voltage levels provided by the FMC+

Voltage	Max. current	Max. capacitive load
$V_{ADJ}$ , 0 V to 3.3 V	4 A	1000 $\mu$ F
3.3 V	3 A	1000 $\mu$ F
12 V	1 A	1000 $\mu$ F

Clocking capable pins can be used to propagate clock signals from the mezzanine to the carrier board.

Furthermore, the connector provides pins for power supply from carrier board to mezzanine card. [FMC] The voltage levels provided are listed in Table 4.1.

### Analog Signals

The analog signals coming from the power-splitter are propagated to the THAs through 1.85 mm high-frequency connectors. These connectors use an air dielectric filled interface which enables operation up to 65 GHz. This type of connector is also called “V connector”; due to its frequency range it is considered as a mm-wave RF connector. It is therefore used in precision instrumentation and other laboratory applications. The design has been introduced as an open standard under the Institute of Electrical and Electronics Engineers (IEEE) 287 Precision Connector Standards Committee.

Figure 4.4 shows a V connector in male and female type.

**Figure 4.4.** Male and female type V connector

On the read-out board two RFMC 2.0 (RF Mezzanine Card) interface connectors are provided. The connectors used are Low Profile Array, Female (LPAF) connectors from *SAMTEC* with 400 pins arranged in a  $8 \times 50$  array. One connector is dedicated for transmitting signals from the mezzanine card to the on-board ADCs. The other provides the analog output from the on-board DACs<sup>3</sup> to the mezzanine card. On the sampling board, the male counterpart of the connectors, Low Profile Array, Male (LPAM), is used (see Figure 4.5).

### Clock Signals

The clock signals from the PLLs on the sampling board are propagated in different ways. The reference clock for the FPGA is propagated through the FMC+ connector. Clocking for the ADCs and the DACs is provided through a  $6 \times 20$  LPAM connector (see Figure 4.6).

<sup>3</sup>A DAC translates digital values into an analog signal.

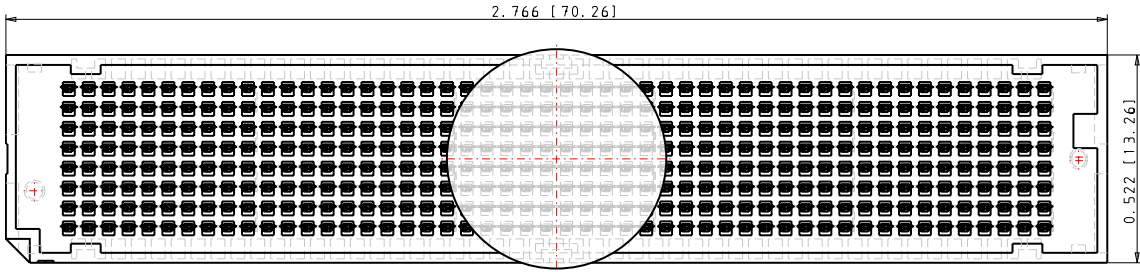


**Figure 4.5.** Part drawing of a LPAM 8 × 50 connector

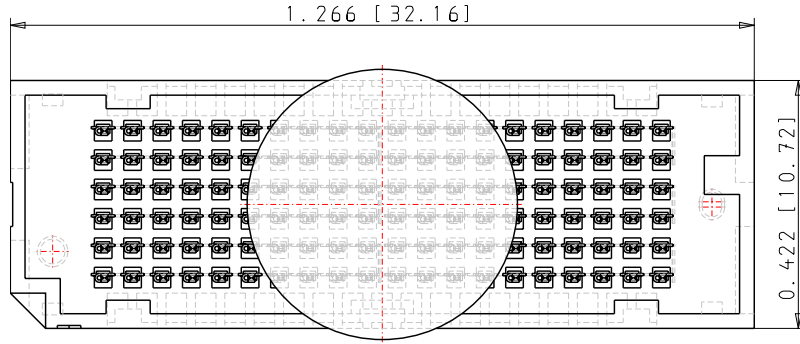


**Figure 4.6.** Part drawing of LPAM 6 × 20 connector

The clock coming from KARA is provided through RF SMA connectors directly to the PLL.

#### 4.1.2. Sampling-Channel

The most important circuit part of the sampling board is the sampling channel. On the board, 16 of such sampling channels are present integrating a wideband THA and delay chip. The sampling time of the THA, derived from the clock coming from the main PLL on the board, can be delayed individually by programming the delay time of each delay chip respectively (via FPGA).

##### Track-And-Hold-Amplifier

The THA used is the same as in KAPTURE. The component has been chosen due to its high bandwidth ( $> 18$  GHz) and low aperture jitter (range of hundreds of femtoseconds). [CBC<sup>+</sup>13] Therefore it is also a good candidate for the new THERESA sampling board.

The main features of the THA are listed in Table 4.2. These input specifications are important for the later interface with the ADC with the delay chip. Switching characteristics are important for estimation of the maximal sample frequency possible and overall performance of the system.

The input coming from the power-splitter is single-ended. However, the analog input of the THA is differential, therefore a  $50\Omega$  termination on the unused input pin has been added, as recommended in the data sheet [Anad].

The differential outputs are connected to the corresponding RFMC LPAM 8x50 connector pins. The schematics of the THA is shown in Figure 4.7.

At the power pins, decoupling capacitors and a ferrite bead were placed. The THA is a crucial component, as it samples the sensor signal, therefore any possible noise should be reduced to a minimum.

**Table 4.2.** Specifications of the HMC5640 THA

Parameter	Min	Typ.	Max	Unit
<b>Analog Inputs</b>				
Differential FS Range		1		V <sub>pp</sub> <sup>1</sup>
Common mode voltage	-0.1	0	0.1	V
<b>Clock Inputs</b>				
DC Differential High Voltage (Track Mode)	20	40	2000	mV
DC Differential Low Voltage (Hold Mode)	-2000	-40	-20	mV
Common mode voltage	-0.5	0	0.5	V
<b>Analog Outputs</b>				
Differential FS Range		1		V <sub>pp</sub>
Common mode voltage		0		V
<b>Track-to-Hold/Hold-to-Track Switching</b>				
Aperture Delay		-6		ps
Random Aperture Jitter (FS, 1 GHz)		< 70		fs
Settling time <sup>2</sup> (to 1 mV)		116		ps

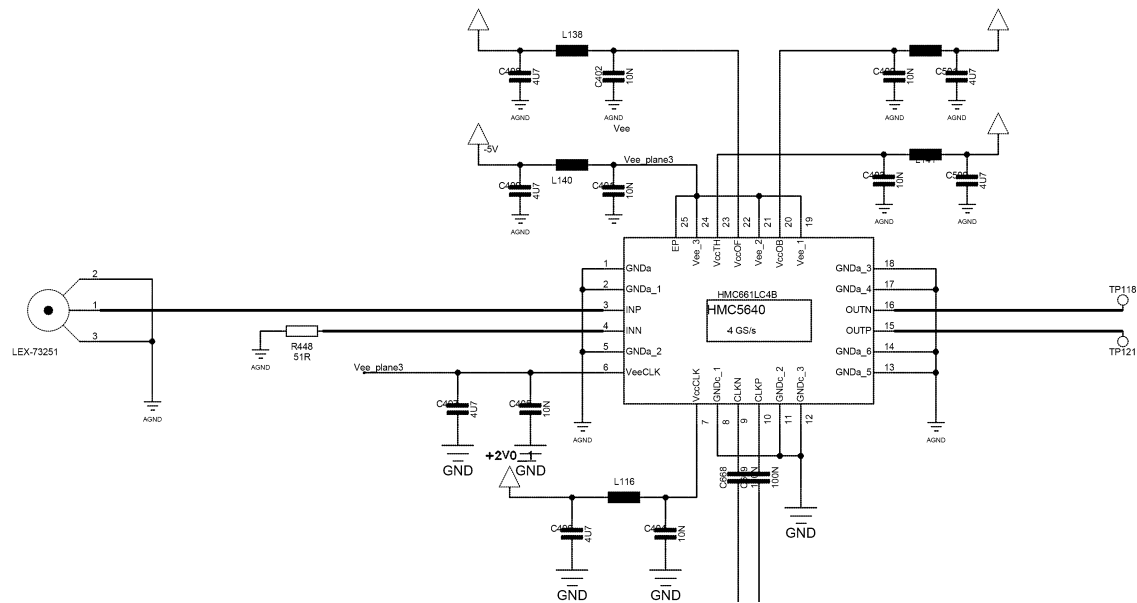
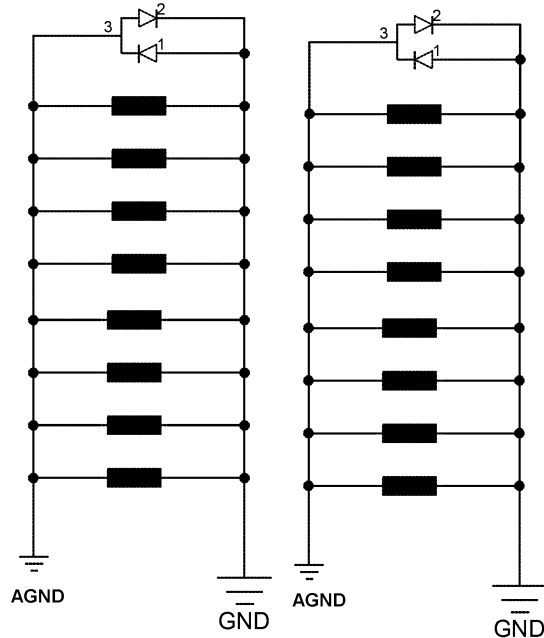
<sup>1</sup>Volt peak-to-peak<sup>2</sup>*Settling time* is the interval between the internal track-hold transition and the time when the output signal is settled within the specified value.

## Separating Analog and Digital Ground

Digital ground is more noisy than analog ground due to switching of the digital components. Analog components are more sensitive to noise (due to e.g. lower amplitudes) than digital components<sup>4</sup> and need a clean ground. In a mixed-signal (having both analog and digital signals) PCB analog and digital ground should be therefore well separated. For some mixed-signal components, such as THAs, where separate analog and digital ground pins are provided. However, it is recommended to connect both grounds directly at the component. For the THAs in this design, this is done by connecting the ground pins via ferrite bead at each THA (see Figure 4.8). The ferrite bead mitigates any high-frequency components and therefore protects the analog ground from noise. For every THA, one ferrite bead is needed, making a total of 16 beads (see Figure 4.8).

Protection against a possible high voltage level between analog and digital grounds is implemented by two back-to-back diodes (Figure 4.8). The diodes should limit this voltage to around 0.6 V.

<sup>4</sup>Digital components work with voltage thresholds, rather than concrete voltage levels.

**Figure 4.7.** HMC5640 THA schematic**Figure 4.8.** Connection of the analog and digital grounds at the THAs

## Delay Chip

The delay chips are employed to create a delay in the sampling time of the THA chips. For the selection of the delay chip, the most important characteristics, apart from time jitter, is the delay step size and delay range.

To optimize the performance of THERESA and allowing a sample rate up to 40 GS/s (see subsubsection 3.2.1.2), the step-size of the delay chip must not exceed 25 ps.

With the HMC856 delay chip from *Analog Devices*, which is also used for the KAPTURE sampling board, a minimal step size of 3 ps [Anab] is possible. This is much less than 25 ps and thus the chip could be potentially used for the intended purpose. However, one drawback is the limited delay range of 100 ps. Considering a signal, which is stretched over several nanoseconds, this range limits the possibility to sample large time-stretched optical pulses. Another challenge, coming from the available number of I/Os, is the programming interface of the chip, which consists of five differential Current Mode Logic (CML) inputs. This means, one chip already takes up 10 pins only for control signals. For a total of 16 necessary delay chips, this results in 160 pins used only for control of the delay chips. This uses up all pins of the FMC+ connector (see subsection 4.1.1) available for user-defined purpose.

A better candidate is the dual channel programmable delay chip NB6L295 from *ON Semiconductor*. This chip provides two separately programmable delay channels. This reduces the necessary chip count by half and therefore reduces the overall complexity of the PCB. The minimal delay step size of 11 ps lies under the maximal allowed 25 ps. Therefore the chip is suitable for the targeted interleaving method, covering a total delay range up to 8.8 ns per delay channel.

The chip is programmed via Serial Data Interface (SDI), which only requires 4 pins (enable pin, data pin, clock pin, load pin). Thus, the total number of digital control pins used by the delay chips is  $4 \cdot 8 = 32$ , which is a significant reduction compared to the 160 control pins needed by the HMC856 chips. This number can be even more reduced, by propagating the same data, clock and load pins to the chips and providing the enable signal on individual lines to the respective chip (see Figure 4.9). In this way, only 11 pins (8 enable pins and 3 pins for data, clock and load) are necessary in total for programming all delay chips.

The schematic of the delay chips is shown in Figure 4.10.

## Inputs

The inputs of the delay chip are driven by the preceding low time-skew, low-jitter and high-performance clock distribution , the outputs of which are Low-Voltage Positive Emitter-Coupled Logic (LVPECL) drivers. According to the data sheet, when driving the inputs

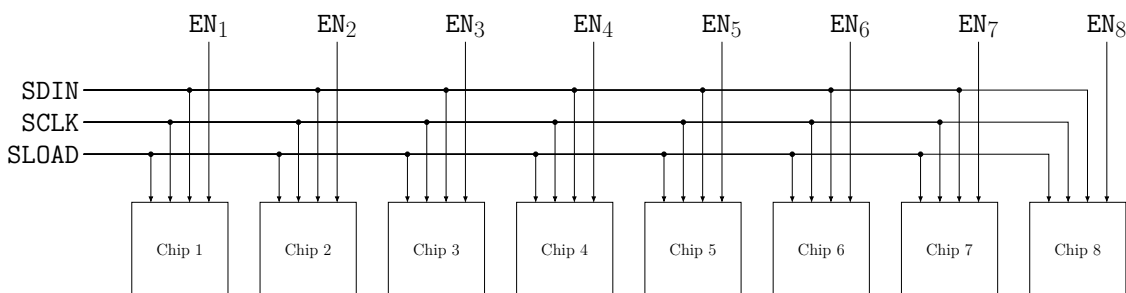


**Figure 4.9.** Diagram of the SDI control pins for the NB6L295 delay chip. The data (SDIN), clock (SCLK) and load (SLOAD) pins are shared by all chips. Only the enable (ENx) signals are routed individually.

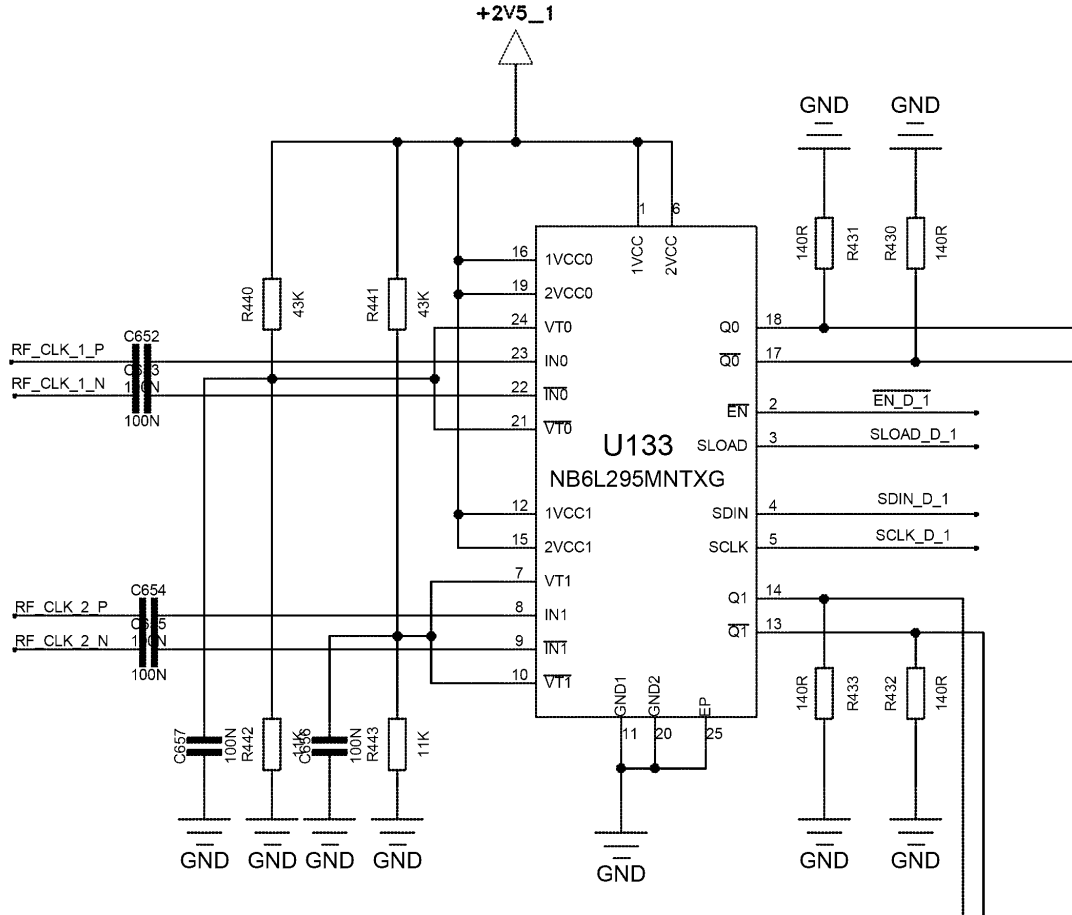


**Figure 4.10.** NB6L295 delay chip schematic

with a LVPECL driver, the  $V_{Tx}$  and  $\overline{V_{Tx}}$  pins of the delay chip need to be connected to  $V_{cc} - 2\text{ V}$  (see Figure 4.12). In case of  $V_{cc} = 2.5\text{ V}$ , this results in a voltage level of  $V_{Tx} = \overline{V_{Tx}} = 0.5\text{ V}$ .

This voltage level is achieved by using a resistive voltage divider connected to  $V_{cc}$ . A voltage divider with the resistors  $R_1$  and  $R_2$  (see Figure 4.11) produces a voltage  $V_{out}$  which is a fraction of the input voltage  $V_{in}$ .  $V_{out}$  is calculated as

$$V_{out} = \frac{R_2}{R_1 + R_2} V_{in}. \quad (4.1)$$

The resistor values are chosen to be  $R_1 = 43\text{ k}\Omega$  and  $R_2 = 11\text{ k}\Omega$ . According to Equation 4.1 this results in a voltage of

$$V_{cc} \frac{11\text{ k}\Omega}{11\text{ k}\Omega + 43\text{ k}\Omega} = 0.5093\text{ V} \approx 0.5\text{ V} \quad (4.2)$$

at the  $V_{Tx}$  and  $\overline{V_{Tx}}$  pins. Resistor values are chosen high to minimize current flow. A 100 nF capacitor is put in parallel to stabilize  $V_{cc}$ .

According to the data sheet [ONS], the digital control pins need a minimum input HIGH voltage of 2 V. Directly connecting to the FMC+ connector pins is therefore not possible, as the maximal level provided by the readout card is smaller than 2 V. The SN74AVC32T245 bus transceiver from *Texas Instruments* (see Figure 4.13) which allows for level shifting from 3.3 V at the device input to 1.8 V at the device output. In this design, the bus transceiver is configured to propagate signals from the “A” ports (coming from the FMC+ connector)

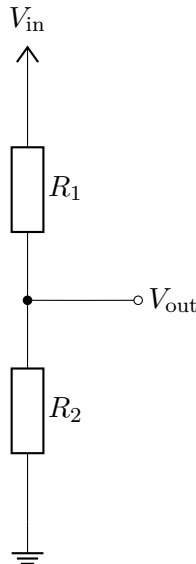


**Figure 4.11.** Schematic of a resistive voltage divider

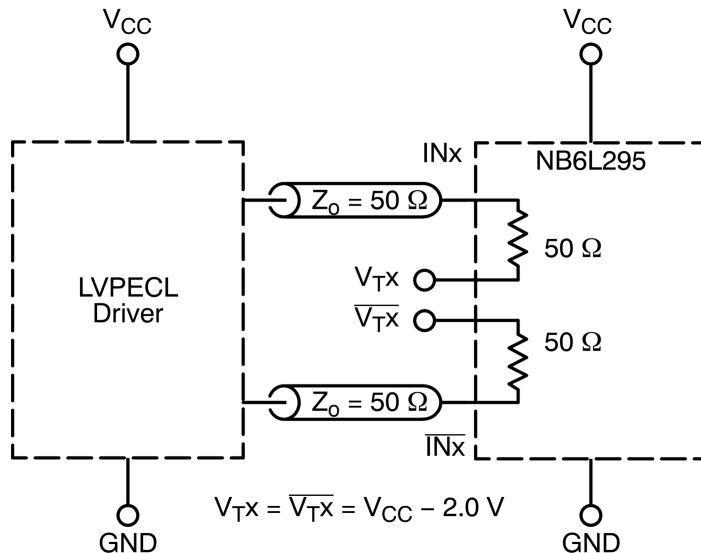


**Figure 4.12.** LVPECL recommendations for NB6L295 [ONS]

to the “B” ports (going to the delay chips), shifting the signals from the  $V_{ADJ}$  (1.8 V) of the FMC+ connector to 2.5 V (see Figure 4.13). To guarantee signal integrity and to decouple the components, the digital signals are propagated in a “fanout configuration”, i.e. one digital signal at the input is propagated to eight outputs. Furthermore, resistors are placed at the pins to reduce possible voltage overshoots which result from reflections on the line.

## Outputs

The output of the delay chip is using a LVPECL signaling interface, which is based on an open-emitter topology (see Figure 4.14). This requires a path to DC, which is achieved by adding  $140\ \Omega$  resistors (recommended in the data sheet).

As the output will be connected to the THA, it is necessary to check the compatibility of the maximum amplitude and common-mode of the pins.

According to the data sheet [ONS], the voltage level of the output can vary between  $V_{cc} - 1825\text{ mV}$  and  $V_{cc} - 825\text{ mV}$  (see Table 4.3). Maximal voltage amplitude acceptable by

**Table 4.3.** Specifications of the NB6L295 delay chip [ONS]

Parameter	Min	Typ.	Max	Unit
<b>Outputs</b>				
Output HIGH Voltage	$V_{cc} - 1075$	$V_{cc} - 950$	$V_{cc} - 825$	mV
Output LOW Voltage	$V_{cc} - 1825$	$V_{cc} - 1725$	$V_{cc} - 1625$	mV
Output HIGH Voltage ( $V_{cc} = 3.3\text{ V}$ )	2225	2350	2475	mV
Output LOW Voltage ( $V_{cc} = 3.3\text{ V}$ )	1475	1575	1675	mV
Common mode voltage	-0.1	0	0.1	V
<b>AC Characteristics</b>				
Random Clock Jitter RMS		3	10	ps
Output Rise/Fall Times <sup>1</sup>	85	120	170	ps
Serial Clock Input Frequency <sup>2)</sup>			20	MHz
Minimum Pulse width SLOAD	1			ns

<sup>1</sup>(@50 MHz)<sup>2</sup>(50% Duty Cycle,Percentage of the ratio of pulse width and total period of the waveform.)

the THA inputs is 2000 mV (see Table 4.2). When using a supply voltage of  $V_{cc} = 3.3\text{ V}$ , provided e.g. by the read-out card through the FMC+ connector, this leads to a maximum output level of 2475 mV. This exceeds the limit given by the THA. Therefore, for  $V_{cc}$  a smaller voltage should be considered. In this design a voltage of  $V_{cc} = 2.5\text{ V}$  is chosen, which guarantees that the amplitude falls within the range 675 mV to 1675 mV.

The second point to consider is the common mode voltages. According to the data sheet of the THA, the common mode voltage of the input clock pins is 0.1 V (see Table 4.2). The common mode voltage of the delay chip is not explicitly mentioned in the data sheet, thus it has to be calculated.

The common mode voltage  $V_{CM}$  is just the mean value between the HIGH level and the LOW level voltage of the output pins:

$$V_{CM} = \frac{V_{out, \text{LOW}} + V_{out, \text{HIGH}}}{2}. \quad (4.3)$$

According to this, the common mode voltage  $V_{CM}$  of the delay chip output, when taking the minimum/maximum voltage level values, is

$$V_{CM} = \frac{675\text{ mV} + 1675\text{ mV}}{2} = 1175\text{ mV}. \quad (4.4)$$

This is higher than the maximal input common mode voltage of the THA. AC coupling is therefore necessary in this case, i.e. connecting the pins via capacitors.

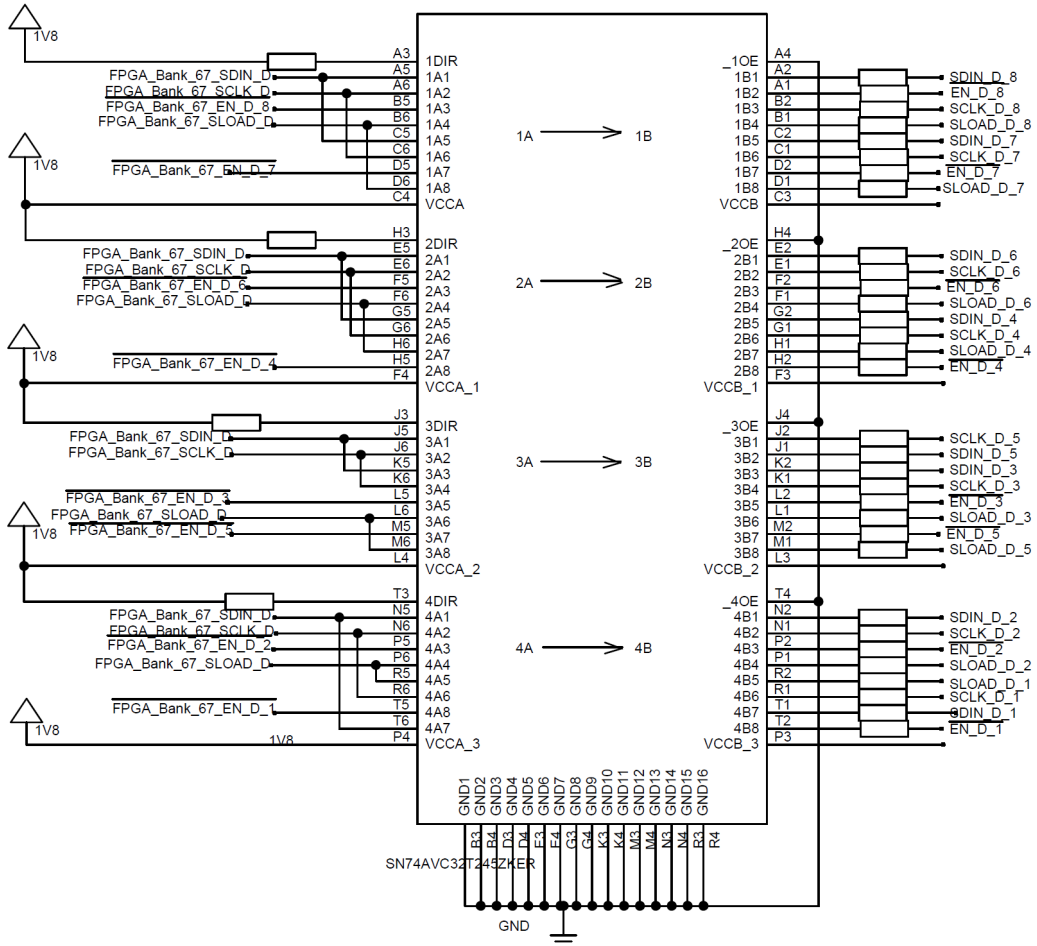


**Figure 4.13.** Schematic of the SN74AVC32T245 bus transceiver

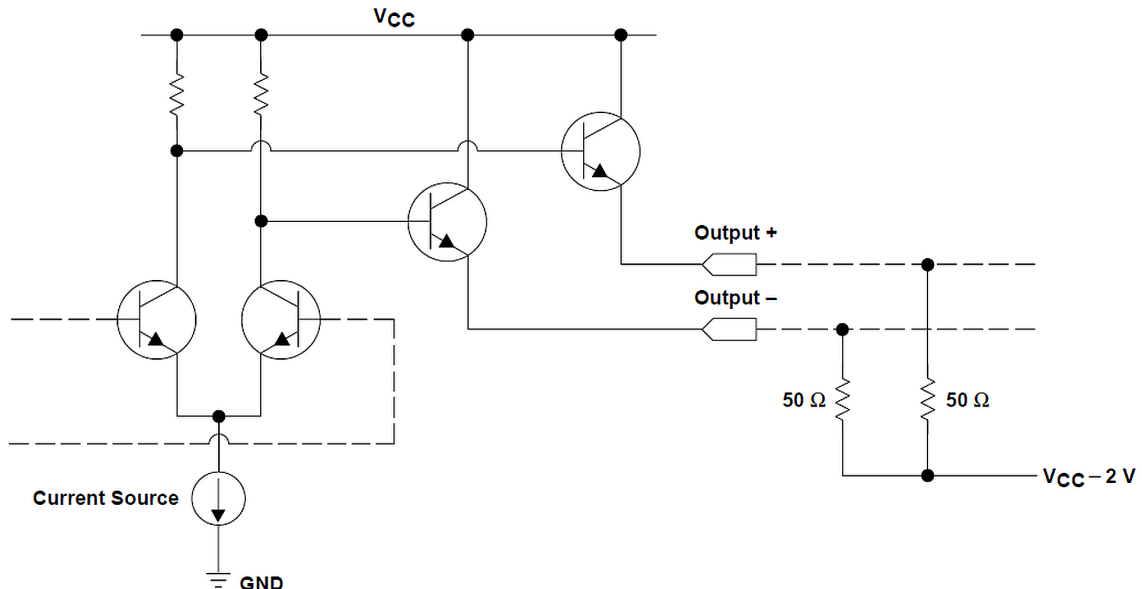


**Figure 4.14.** LVPECL driver topology. Left side shows the emitter-follower based driver. On the right, an example biasing with resistors is shown. [Mik]

### 4.1.3. Clock Distribution

The clock distribution is designed as shown in Figure 4.15.

The LMK04808B low-noise clock jitter cleaner with dual-loop PLLs from *Texas Instruments* cleans the incoming reference clock provided from the system (e.g. from KARA) for high temporal precision [CBC<sup>+</sup>13]. It is used with an external Voltage-Controlled Crystal Oscillator (VCXO) from *ABRACON*.

The LMK04808B contains two PLLs (therefore called “dual-loop”). The first PLL is used to clean the jitter from the reference clock. The second is then used to generate and distribute the cleaned clock signals to the outputs of the components.

Time skew between the PLL outputs lies in the range of 30 ps ([Tex]). Compared to the 11 ps delay step this is very high and therefore not suitable for high temporal accuracy. In order to guarantee low time skew (range of few picoseconds), two fanout buffers are used to distribute the cleaned clock signal to the components on the board. The fanout buffers used are the HMC987LP5E from *Analog Devices*. Time skew of these components between channels typically lies in the range of 1.5 ps, 20 times smaller than the time skew of the PLL. As one fanout buffer has eight outputs, two chips are needed to cover all 16 sampling channels. Each fanout receives the clock reference from one output of the LMK0480B. To ensure exactly identical clocking signals between the two fanouts they are connected to two outputs of the same output group.

The LMK04808B has only 12 outputs which are divided into six groups à two outputs. Outputs in one group have the same configuration (frequency, phase, ...), which means that effectively only six different outputs are available. This is not enough for the 16 THAs and additional clock signals needed for FPGA, ADCs and DAC.

One output of the PLL is propagated to the FMC+ connector as reference clock for the FPGA.

The maximum output frequency of the LMK04808B is 1536 MHz, not enough to clock the ADCs at maximum sampling rate (2.5 GS/s). A second kind of PLL is therefore needed to provide programmable reference clocks to the ADCs and DACs. As Figure 4.15 shows, the LMK04808B also provides a clocking signal to other PLLs, the LMX2594 from *Texas Instruments*. This PLL is able of clocking signal frequencies up to 15 GHz.

Due to the ADC clocking limitations on the read-out card explained in subsubsection 3.2.1.2, two of the PLLs are needed. The reference clock signal is provided by outputs from different output groups of the LMK04808B. This way, the phase of each reference clock can be programmed individually, which allows to implement the ADC clocking technique described in subsubsection 3.2.1.2.

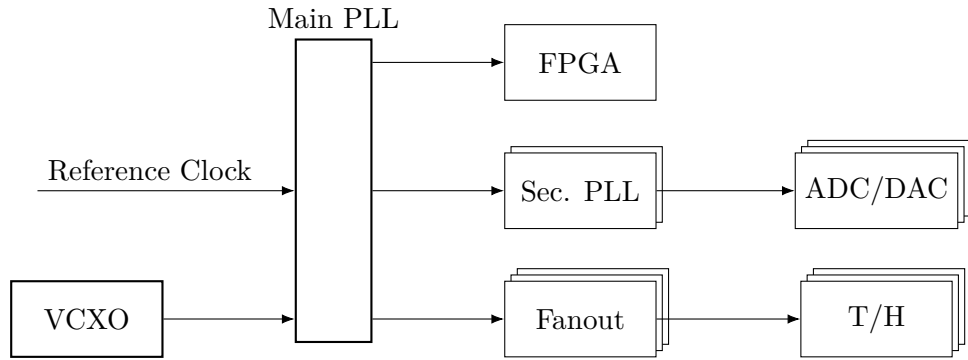


**Figure 4.15.** Overview of the clocking paths on the sampling board

### PLLs

A PLL is a control loop, used to synchronize an output oscillator signal with a reference signal. The principle lies in comparing the phases between the two inputs. When there is a varying phase difference, it means that the signals are at different frequencies. As soon as the phase difference stays constant, it means that both of the frequencies are the same or one is a multiple of the other. In this state the PLL is called to be “locked”. The general architecture of a PLL is shown in Figure 4.16.

For proper noise performance, a properly designed loop filter for both PLLs is needed. The output of the loop filter is the voltage for controlling the Voltage-Controlled Oscillator (VCO). The VCO output of is a frequency  $f_{\text{VCO}}$  proportional to the applied voltage.  $f_{\text{VCO}}$  is divided by the  $N$  Divider to the frequency  $f_n$  and then compared to the phase detector frequency  $f_{\text{PD}}$  in the phase detector.  $f_{\text{PD}}$  results from dividing the reference frequency  $f_{\text{osc}}$  with an  $R$  divider. The phase detector produces current correction pulses (with magnitude  $K_{\text{PD}}$ ) with a duty cycle proportional to the phase error between  $f_{\text{PD}}$  and  $f_n$ . These pulses are filtered by the low pass loop filter, which basically converts these pulses into a voltage. [Ban] The loop filter is one of the key component determining the PLL performance (concerning jitter, noise, ...) and therefore has to be designed carefully.

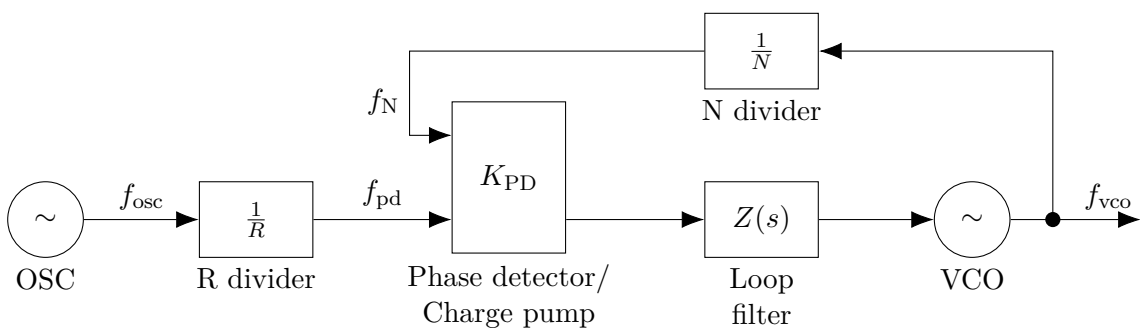


**Figure 4.16.** General block diagram of a PLL [Ban]

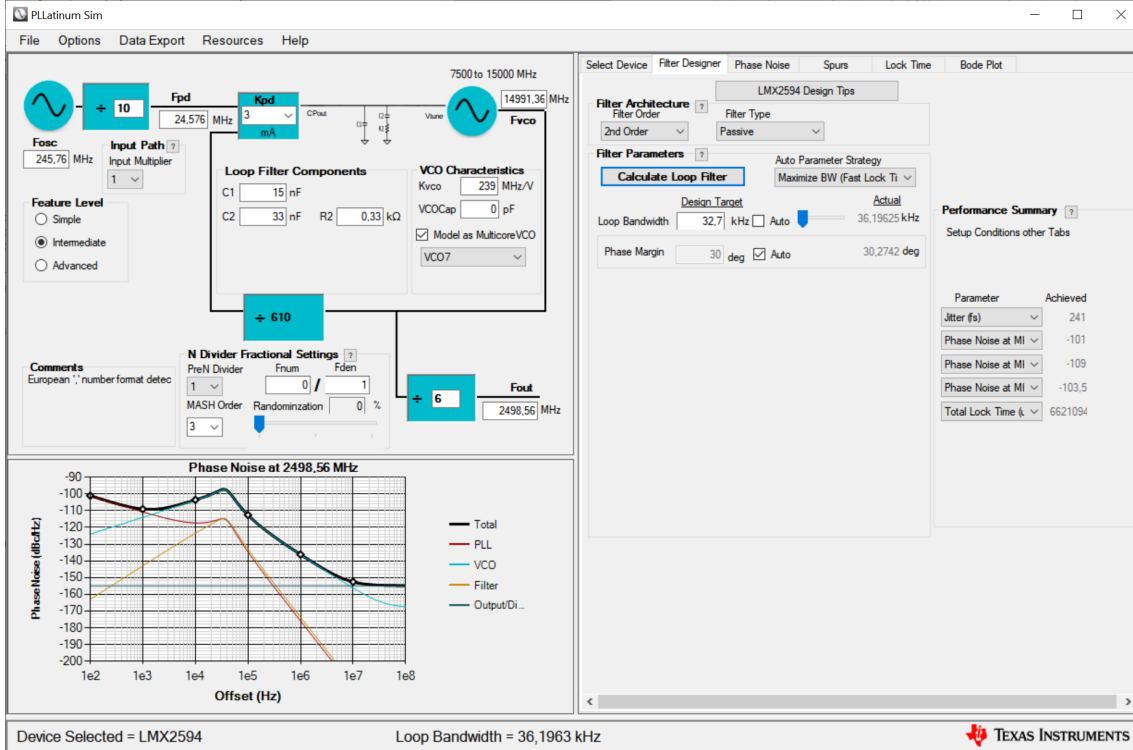


**Figure 4.17.** Screenshot of the TI PLLatinum Sim tool for loop filter design and PLL performance simulation

To calculate the loop filter, the *Texas Instruments PLLatinum Sim* tool is used (see Figure 4.17). This tool provides a convenient way to calculate the necessary loop filter components, given the VCO characteristics, desired filter order, charge pump current and desired performance (e.g. optimize jitter). A passive fourth order loop filter is shown in Figure 4.18. In order to implement a lower order filter, some components need to be left out. To implement an active filter an additional operational amplifier is necessary. The input of the filter is connected to the output of the charge pump from which it receives the current pulses. The output of the filter is the voltage  $V_{\text{tune}}$  which is the input to the VCO.

The LMK04808B has two PLLs inside (PLL1 and PLL2). For both the loop filter has to be calculated separately. Both filters are implemented as second order filters, the calculated parameters are listed in Table 4.4. Note that PLL2 has already a partially integrated loop filter.

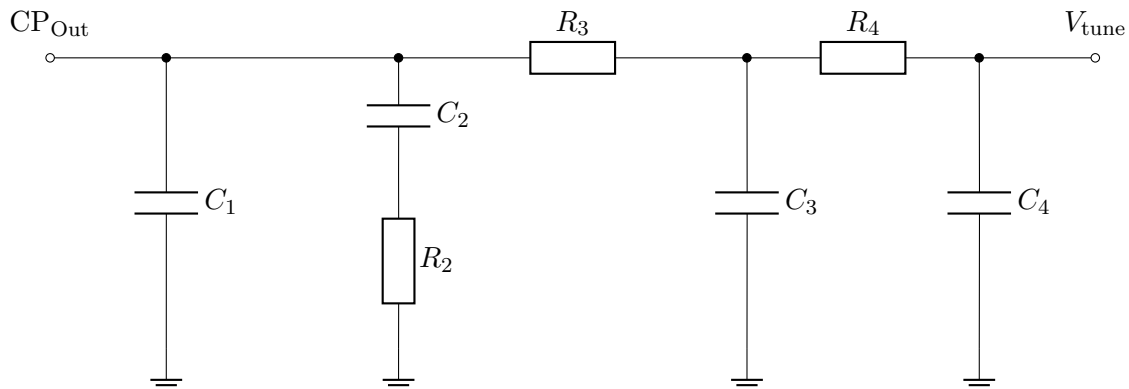


**Figure 4.18.** Passive fourth order loop filter for PLL

**Table 4.4.** Loop filter characteristics of the LMK04808B

Parameter	Value
<b>PLL1 parameters</b>	
VCO Gain	0.15 MHz/V
Loop Bandwidth	0.2578 kHz
Phase Margin	70°
Effective Charge Pump Gain	0.4 mA
Phase Detector Frequency	25 MHz
VCO Frequency	200 MHz
<b>Loop filter components for PLL1</b>	
$C_1$	39 nF
$C_2$	1800 nF
$R_2$	2.2 kΩ
<b>PLL2 parameters</b>	
VCO Gain	30 MHz/V
Loop Bandwidth	390.9624 kHz
Phase Margin	70°
Effective Charge Pump Gain	1.6 mA
Phase Detector Frequency	50 MHz
VCO Frequency	3000 MHz
<b>Loop filter components for PLL2</b>	
$C_1$	22 pF
$C_2$	2.2 nF
$R_2$	3.3 kΩ

The loop filter for the LMX2594 is designed in the same way as described above with the *PLLatinum Sim* tool. The calculated values for the components to be implemented are shown in Table 4.5. The filter is implemented as a third order passive filter. The schematic and layout of the filter have been implemented in a way to enable alteration of the filter, i.e. changing the filter order or component values. The schematic and layout have been implemented in order to enable flexible change. This gives the possibility to experimentally find the correct order and components for best performance by real measurements with the board. The schematic of the LMX2594 is shown in Figure 4.19.

Both PLLs are supplied by the digital 3.3 V coming from the FMC+ connector. For the output buffer supply (VCC\_RFBUF) of the LMX2594, an additional EMI filter is used to provide effective filtering of the voltage level. The output pins are pulled-up and filtered via ferrite bead to VCC\_RFBUF as recommended in the data sheet. For the schematic of the LMX2594 see Figure 4.19.

**Table 4.5.** Loop filter characteristics of the LMX3594

Parameter	Value
<b>PLL parameters</b>	
VCO Gain	239 MHz/V
Loop Bandwidth	32.7 kHz
Phase Margin	69°
Effective Charge Pump Gain	3 mA
Phase Detector Frequency	24.576 MHz
VCXO Frequency	Designed for 15 GHz
<b>Loop filter components</b>	
$C_1$	2200 pF
$C_2$	180 nF
$C_3$	1800 pF
$R_2$	160 Ω
$R_3$	180 Ω

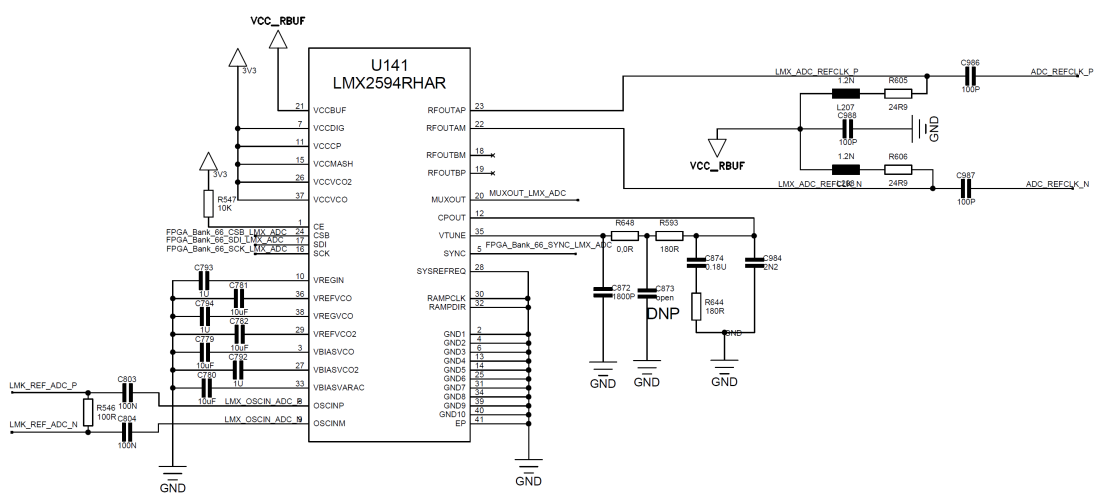


**Figure 4.19.** Schematics of the LMX2594

## Fanout Buffer

The fanout buffer receives as input the clock signal from the main PLL and distributes it to the delay chips. In this design, the HMC987LP5E from *Analog Devices* is chosen due to its low jitter and low skew performance. The schematics of the chip is shown in Figure 4.20.

Decoupling capacitors are placed at every power supply pin in order to guarantee a clean and stable voltage level.

The outputs of the fanout buffer is based on LVPECL signaling interfaces and therefore need to be connected to ground via resistors. Outputs can be enabled or disabled either via SPI (setting pin PMODE\_SEL to '0') or by using parallel pin control (setting pin PMODE\_SEL to '1').

In parallel pin control the SPI pins **SCLK**, **SDI** and **SEN** are reinterpreted as a 3-bit control bus. In this mode, the pins are either pulled up to  $V_{cc}$  or connected to ground via on-board jumpers to represent a logic '1' or '0'. For the design, the parallel pin control mode is selected, therefore the **PMODE\_SEL** pin is pulled up to  $V_{cc}$  ( $\cong$  logic '1'). In order to have the opportunity to enable the SPI mode in later usage, a jumper is placed at this pin so that it can be connected to ground if necessary ( $\cong$  logic '0', enabling SPI mode). The **SCLK**, **SDI** and **SEN** pins are connected to the FMC+ connector. To enable all outputs, the SPI pins need to be set to '111' according to the datasheet, i.e. pulled-up to  $V_{cc}$ . Here, jumpers are foreseen as well, to allow enabling/disabling in later usage.

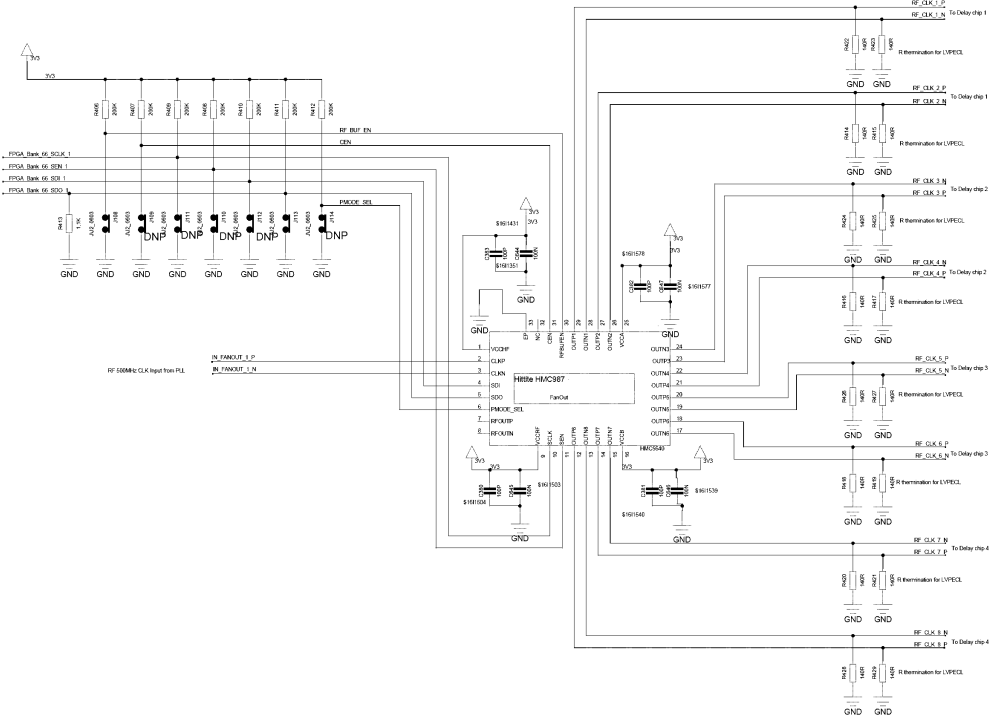


**Figure 4.20.** Schematic of the fanout

#### 4.1.4. Digital-To-Analog-Converter Channels

For test purposes, two DAC channels from the read-out card are routed on the sampling board. In this way, a programmable analog waveform can be generated by FPGA, without the need for an external signal generator. The differential inputs from the DACs are transformed into single ended outputs with dedicated baluns<sup>5</sup>. the BD3150N50100AHFa and the BD4859N50100AHF from *Anaren*. These are used for the signal frequency range 3.1 GHz to 5.0 GHz and 4.8 GHz to 5.9 GHz respectively. The single-ended output is connected to a miniature RF connector from *Hirose Electric*.

The programmable analog waveform, generated by the DAC (operating up to 10 GS/s), can be applied to the input of the sampling board as a test signal and be employed for testing, characterizing and calibrating each sampling channel individually.

The schematic of a DAC channel is shown in Figure 4.21.

<sup>5</sup>balanced to unbalanced

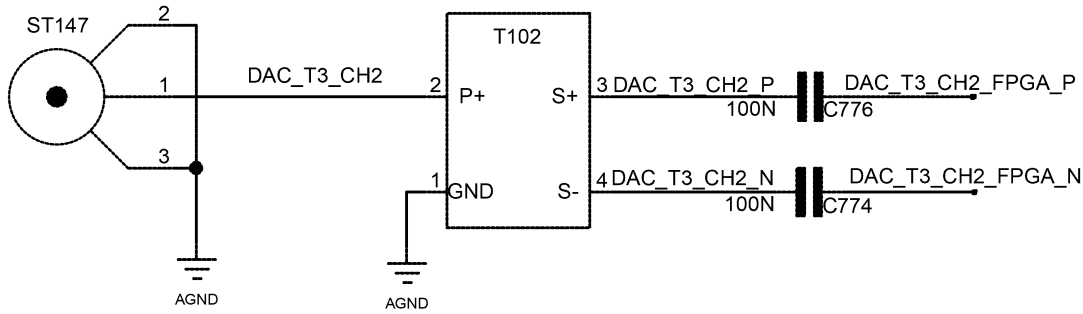


**Figure 4.21.** DAC-channel with balun. Signal propagates from right to left.

#### 4.1.5. Power Supply

Low-ripple power supply is an important point key for low noise performance of the board. Especially high-performance ICs, such as THAs, highly rely on a low-ripple voltage level for correct functionality. Therefore, proper power supply design is an important step which needs to be handled with care. This step includes the selection the right type voltage regulators, as well as providing appropriate filtering. Furthermore, in order

Table 4.6 lists the power supply requirements of all the components used on the board.

**Table 4.6.** Power consumption of components on the board

Component	$V_{cc}$ (V)	$I_{max}$ (A)	$P_{max}$ (W)	#parts	$I_{tot, max}^1$ (A)
HMC5649 (THA)	2	0.221	0.442	16	3.536
NB6L295 (Delay chip)	2.5	0.170	0.425	8	1.36
HMC987LP5E (Fanout buffer)	3.3	0.234 <sup>2</sup>	0.772	2	0.468
LMK04808B (PLL)	3.3	0.590 <sup>3</sup>	1.947	1	0.590
LMX2594 (PLL)	3.3	0.340	1.122	2	2.244
VCXO	3.3	0.03	0.198	1	0.03

<sup>1</sup>for 16 ADCs

<sup>2</sup>All Outputs and RF-Buffer

<sup>3</sup>All CLks

In general, there are four different voltage supplies provided by different sources:

- 1.8 V for digital components coming from FMC+ connector
- 3.3 V for digital components coming from FMC+ connector
- 3.3 V and -5 V for analog devices from external power supplies

An EMI filter needs to be placed in order to reduce the electromagnetic interference from external sources. The filter used is a passive LC low pass filter, the schematic of which is shown in Figure 4.22. It consists of an inductor and several shunting capacitors. This configuration guarantees that high frequency components on the power supply voltage are reduced and high frequency currents are redirected to ground through the capacitors. At

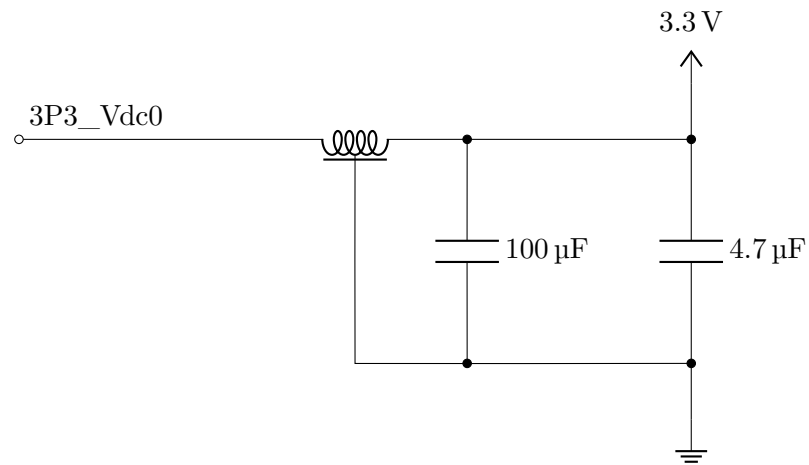


**Figure 4.22.** EMI-filter used for power supply

each power supply one EMI filter has been placed. For the sensitive components like THA voltage regulators have to be used to guarantee low noise operation.

### Voltage Regulator for Track-and-Hold-Amplifiers

The THAs need a low-ripple voltage level for optimal operation. Linear voltage regulators are capable to maintain a stable output voltage and are therefore to be used with the THAs.

On the KAPTURE sampling board, the Low Dropout Voltage Regulator (LDO) ADP1708 from *Analog Devices* is used to provide a power supply for the THAs. A LDO is able to operate at a low potential difference between the input and output voltage. This low potential difference has the benefit of low power dissipation, which also reduces the heat produced by the components. This power supply can provide at maximum 1 A to the load. In order to minimize the amount of components needed on the board and to save space, a different LDO which provides higher currents should be used. This way, one single voltage regulator can be used for more components.

For the new board, the ADP1741 low-dropout voltage regulator from *Analog Devices* has been selected. This voltage regulator has adjustable output voltage from 1.6 V to 3.6 V and a maximum output current of 2 A.

It is necessary to think about the number of voltage regulators needed. As a rule of thumb, the power supply should provide at least twice the maximum current (i.e. power) needed by the components it drives. [Mic] The power consumption/maximum current for the THAs on is listed in Table 4.6.

The maximal output current  $I_{\max, \text{LDO}}$  from the ADP1741 is 2 A. With the rule mentioned above and the maximal current draw  $I_{m, \text{THA}} = 0.221 \text{ A}$  from the THA, the maximal number  $N$  of components which the LDO can handle is calculated as

$$\begin{aligned} I_{\max, \text{LDO}} &> 2 \cdot N \cdot I_{m, \text{THA}} \\ I_{\max, \text{LDO}} / (2 \cdot I_{m, \text{THA}}) &> N \\ 2 \text{ A} / (2 \cdot 0.221 \text{ A}) &> N \\ 4.52 > N &\rightarrow N = 4 \end{aligned}$$

This means, 4 LDOs are needed to cover 16 THAs.

The output voltage level of the regulator is set by an external divider with the resistors  $R_1$  and  $R_2$  (refer to Figure 4.23). According to the datasheet [Anaa] the voltage  $V_{\text{OUT}}$  is determined by

$$V_{\text{OUT}} = 0.5 \text{ V} \left( 1 + \frac{R_1}{R_2} \right) \quad (4.5)$$

In order to achieve the required 2 V, the values of the resistors are chosen to  $R_1 = 30 \text{ k}\Omega$  and  $R_2 = 10 \text{ k}\Omega$ .

As input voltage, the 3.3 V from the external power supply is provided.

Capacitors and resistors are placed as recommended in the data sheet[Anaa](see Figure 4.23).

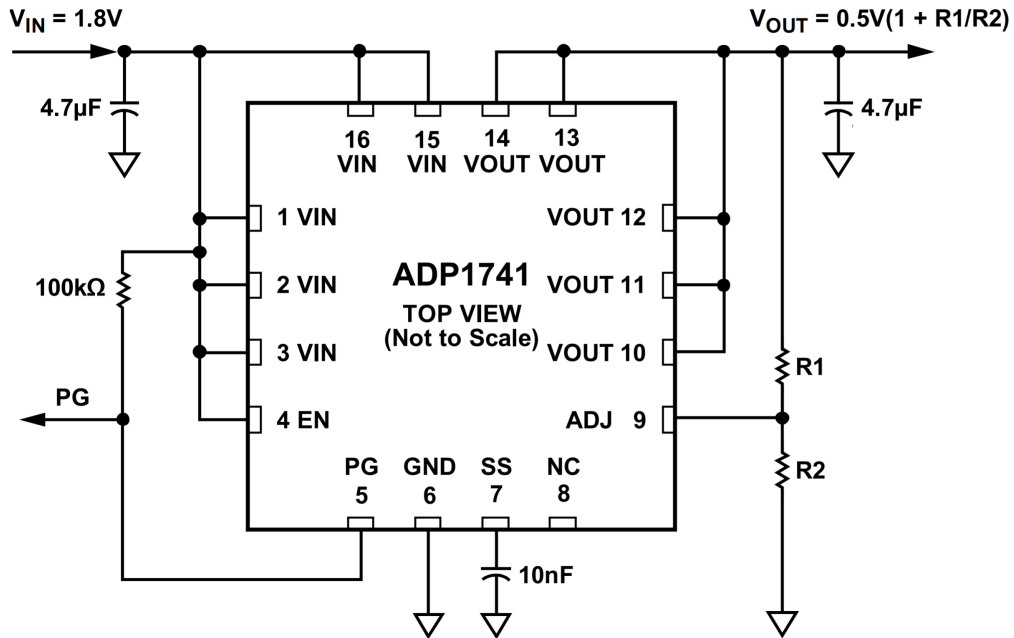


**Figure 4.23.** Recommended schematic of the ADP1741 voltage regulator [Anaa]

### Voltage Regulator for Delay Chips

The delay chips require a voltage level of 2.5 V. As they propagate the sensitive clock signals they also need stable voltage levels. The number  $N$  of delay chips with a maximal current draw  $I_{m, \text{Delay}}$ , which one LDO can handle, can be again calculated as:

$$\begin{aligned} I_{\max, \text{LDO}} &> 2 \cdot N \cdot I_{m, \text{Delay}} \\ I_{\max, \text{LDO}} / (2 \cdot I_{m, \text{Delay}}) &> N \\ 2 \text{ A} / (2 \cdot 0.170 \text{ A}) &> N \\ 5.88 &> N \rightarrow N = 5 \end{aligned}$$

Therefore, two regulators are needed to cover the 8 delay chips. In order to keep the current draw evenly distributed among the regulators, 4 chips are assigned to one regulator respectively.

In order to set the output voltage of the regulator to 2.5 V, the resistor values  $R_1 = 12 \text{ k}\Omega$  and  $R_2 = 3 \text{ k}\Omega$  are chosen (refer to Figure 4.23 and Equation 4.5).

The 2.5 V are also used as input for the bus transceiver which acts as a level translator. The current draw from this component lies in the range of  $\mu\text{A}$  and can thus be neglected.

As input voltage these regulators receive the digital 3.3 V from the FMC+ connector. The ground pins are connected to the digital ground of the PCB. This is important, in order to keep the analog and digital grounds and components separated.

### Power Dissipation of the Voltage Regulators

According to the data sheet of the ADP1741 [Anaa], the power dissipation  $P_D$  of the regulator can be calculated with the input and output voltage  $V_{IN}$  and  $V_{OUT}$ , load current  $I_{LOAD}$  and ground current  $I_{GND}$ <sup>6</sup>:

<sup>6</sup>difference between input and output current

$$P_D = (V_{IN} - V_{OUT}) \cdot I_{LOAD} + (V_{IN} \cdot I_{GND}) \quad (4.6)$$

$I_{GND}$  is very small (range of  $\mu\text{A}$ ), thus the power dissipation due to this current can be neglected. Therefore the equation above can be simplified to:

$$P_D = (V_{IN} - V_{OUT}) \cdot I_{LOAD} \quad (4.7)$$

The power dissipation  $P_{D, THA}$  of one voltage regulator for the THAs is therefore

$$P_{D, THA} = (3.3 \text{ V} - 2 \text{ V}) \cdot (4 \cdot 0.221 \text{ A}) = 1.149 \text{ W}. \quad (4.8)$$

The power dissipation  $P_{D, Delay}$  of one voltage regulator for the delay chips is

$$P_{D, Delay} = (3.3 \text{ V} - 2.5 \text{ V}) \cdot (4 \cdot 0.17 \text{ A}) = 0.544 \text{ W}. \quad (4.9)$$

In order to dissipate the heat, an exposed pad is provided under the component. This pad can be connected through vias to a (ground) plane located on the inner layers, in this way allowing to dissipate the heat through the PCB. Furthermore, a matrix of vias is placed underneath the component area in order to improve the heat flow. This should be enough to handle the calculated power dissipation. Heat sinks could be added later during operation, if the deployed method is not sufficient to dissipate the produced heat.

## 4.2. Layout

After completing the schematic capture, the following step is the PCB layout design. During this process, the following points need to be considered:

- An appropriate PCB substrate has to be chosen. The most important parameter of a substrate is its dielectric constant. For high-frequency circuits, a low dielectric constant is necessary.
- Generally, complex PCBs consist of a number of layers. In order to be able to route all the signals, it is necessary to think about the number of layers needed.
- Closely linked to the dielectric constant are the transmission lines. The geometry of these lines has to be calculated in order to meet the desired characteristic impedance (single-ended:  $50 \Omega$ , differential pair:  $100 \Omega$ ). As this impedance also is defined by the dielectric constant, this step is closely linked to the selection of the substrate.
- Components need to be placed in a way that minimizes traces and routing. Sensitive components, like THAs have to be placed first
- Route traces, taking care that traces of the same group (e.g. clock signals distributed to the THAs) have the same length. For sensitive signals take care that these are shielded by ground planes on the layers above and below.
- Places additional structures to reduce cross-talk, EMI, etc. (via fences, stitching vias, ...)
- Create proper power distribution by placing planes at appropriate places, i.e. reducing overlapping with traces carrying signals that could induce noise on the power plane.

For better understanding, first a general overview over PCB structures is given. Then the steps mentioned above are described.

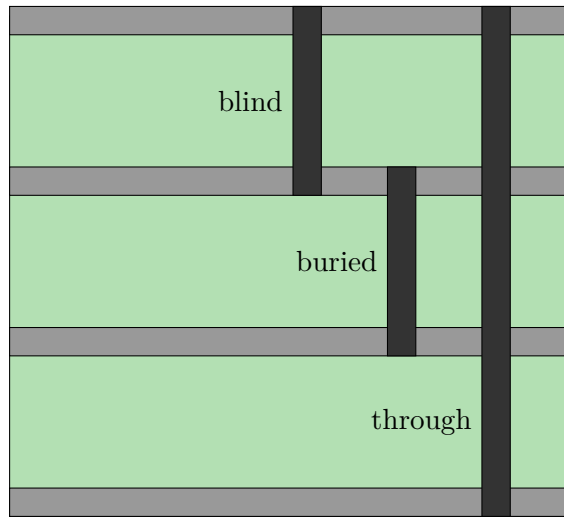


**Figure 4.24.** Visualization of via types [our]

## PCB Structures Overview

In this section an overview over the basic structures on a PCB is given.

### Traces

A *trace* is a strip of metal, which establishes an electrical connection and carries signals between two (or more) points in the horizontal plane of a PCB. [Xile]

### Planes

*Plane* denotes an uninterrupted area of metal, which covers the whole PCB layer. If this area only covers a part of the layer, it is called a *planelet*. These areas provide power distribution or ground across the PCB and present an important transmission medium for the return currents<sup>7</sup>. [Xile]

### Vias

A via is metal-plated hole, which is used to route a trace in vertical direction, i.e. from the PCB outer layer to the inner layers. They carry signals and power. Three types of vias are [our]:

- Blind via: A blind via connects the surface layers with a few layers below.
- Buried via: A buried via only connects internal layers.
- Through-via: A through-via goes from one PCB surface to another and is used to connect any layer.

In this design only blind and through vias are used.

#### 4.2.1. PCB Substrate Selection and Metal Layer Stackup

High-frequency transmission lines require an appropriate and very pure substrate dielectric, which needs to be selected to match the maximum frequency, the acceptable losses, and transmission lines typologies. The Megtron6 substrate from *Panasonic* is designed for high-speed/high frequency applications. Characteristics of this material are:

<sup>7</sup>Any current that is injected into the components/boards, needs a return path, as otherwise there is no closed circuit.

- Low dielectric constant:  $\epsilon_r = 3.61$  at 10 GHz, 3.71 at 1 GHz
- Low dielectric dissipation factor: 0.002 at 10 GHz, 0.004 at 1 GHz
- Low transmission loss
- High heat resistance: Decomposition temperature  $T_d = 410^\circ\text{C}$

Another important step is deciding the number of layers. The complexity of the board implies that a lot of layers are needed in order to integrate the analog and digital signal lines, as well as the necessary power planes. For this design a number of 16 layers is chosen.

In order to keep the analog and digital part of the PCB separated, the top eight layers are dedicated solely to the digital signal lines and components, the bottom eight to the analog. For shielding purposes, every second layer contains a (analog or digital) ground plane covering the whole layer. RF transmission lines carrying the sensitive analog signals from the detector are therefore routed on the inner layers in order to guarantee shielding from any noise or interference. Slow control signals are routed in such way to not destroy the ground above/below the RF lines, i.e. avoiding the area around these lines.

Lines, where time skew control needs to be very precise, are routed in inner layers. Due to the dielectric on both sides of the line, the electromagnetic waves propagate with lower speed, than if the signal lines would have been routed on the top layer. The speed of the waves  $V_P$  can be calculated with the speed of light  $c$  and the effective dielectric constant  $\epsilon_{r,\text{eff}}$  as (see [Thi17]):

$$V_P = \frac{c}{\sqrt{\epsilon_{r,\text{eff}}}} \quad (4.10)$$

The dielectric constant of air<sup>8</sup> is approximately 1, meaning the effective dielectric constant for waves propagating on the top layers is smaller, than the one for waves propagating in the inner layers where they are surrounded by the substrate. According to the equation above, this also results in a higher propagation speed. Time skew control can be handled more easily for slower waves, meaning for lines where the arrival time of the signals should be matched as precise as possible, propagation in the inner layers is necessary.

Filtered voltage from the power supplies is propagated through vias to the inner layers, from where the levels are distributed to the respective components, either by connected plane or single traces.

#### 4.2.2. Transmission Lines

Transmission lines guide electromagnetic waves from one point to another with a well-defined impedance. They have a characteristic impedance which is determined by parameters like width of the trace, separation from ground plane, etc. A mismatch can lead to reflections and damping of the RF signals. For single-ended signals the waveguide characteristic impedance for the front-end sampling card is  $50\Omega$ , for differential pairs  $100\Omega$ . The impedance has to be matched especially for sensitive, high-speed signals, e.g. clock signals. Proper calculation of the geometrical parameters is therefore very important to ensure signal integrity and reduce reflection and damping.

Formulas to calculate the characteristic impedance are quite complex (see section A) and not easy to solve. To make the design of transmission lines easier, specific tools are used for quick calculations of the geometric values needed for impedance matching. For this design, the Si9000e tool for modeling PCB transmission lines from *Polaris* is used to calculate the necessary trace widths, trace separations, etc. A screenshot of the Polaris tool, showing the geometry of a coplanar waveguide is shown in Figure 4.25. Note that the labels used in

---

<sup>8</sup>1.00059 at room temperature ( $25^\circ\text{C}$ ) [Bri]

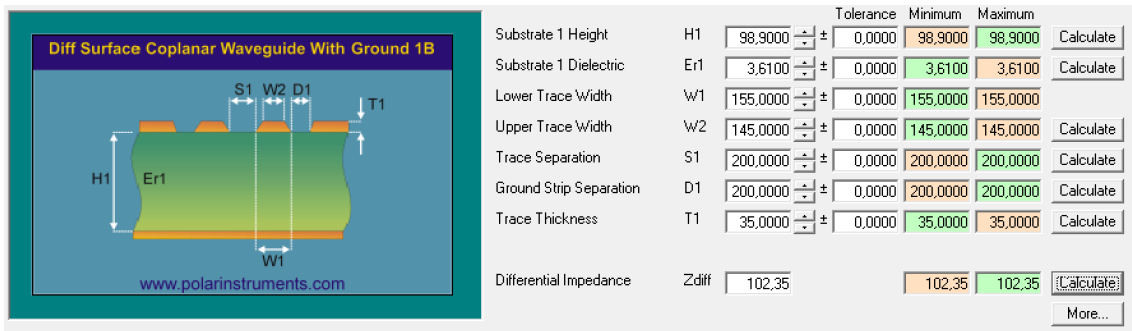


**Figure 4.25.** Screenshot of the Polaris Si9000e tool for modeling PCB transmission lines, showing calculation of characteristic impedance of a coplanar waveguide

the tool to indicate the different geometry parameters are different from the ones used in this thesis.

As there are a lot of parameters which can be tuned, as a starting point the geometrical parameters of the KAPTURE PCB design are applied. These were carefully designed for optimal transmission line geometry. However, the substrate used in the KAPTURE system, has a different dielectric constant than the Megtron6 substrate selected for the new design. Therefore, the impedance has to be recalculated. For the results, a deviation of 10% from the ideal  $50\ \Omega$  and  $100\ \Omega$  is still regarded as acceptable, as tolerances during manufacturing need to be considered.

Three types of transmission lines have been designed for this layout:

- Surface coplanar waveguide with ground layer for analog input to the THAs
- Differential surface coplanar waveguide with ground layer for output from the delay chips to the THAs
- Symmetrical differential coplanar waveguide for clock signals and signals coming from the THAs

These waveguide types and the respective geometric dimensions calculated with the Si9000e tool are presented.

### Surface Coplanar Waveguide with Ground

The surface coplanar waveguide has the geometry shown in Figure 4.26. The single trace of thickness  $t$  and width  $a$  lies between two ground planes on a dielectric of thickness  $h$  and the effective dielectric constant  $\epsilon_r$ . Another ground plane is located at the bottom of the dielectric. Separation between trace and ground plane is defined as  $(b - a)/2 := d$ .

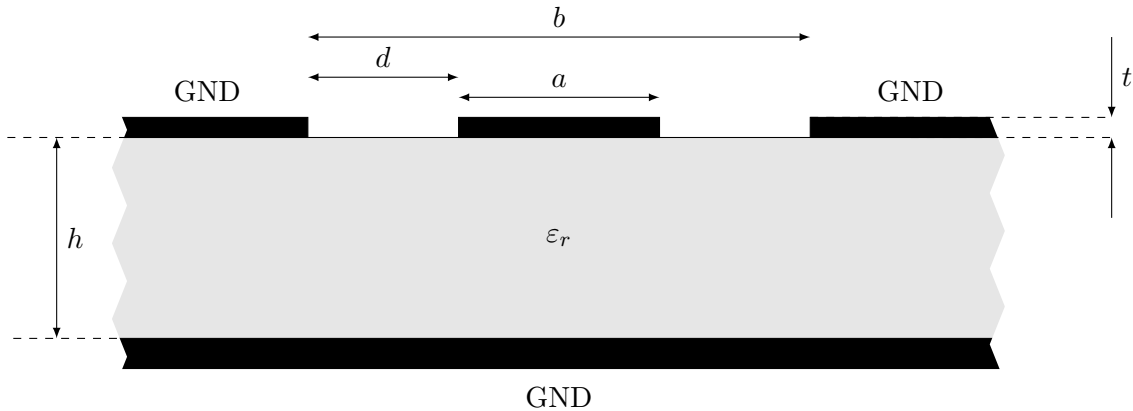


**Figure 4.26.** Coplanar Waveguide with ground plane

To have a rough starting point of the dimensions of the parameters, the following widths are taken from the KAPTURE board:

- $a = 213 \mu\text{m}$
- $d = 250 \mu\text{m}$

In the Si9000e tool, an upper and a lower trace width can be specified taking into account the etching process during manufacturing. The exact production parameters are not known, therefore there is no knowledge about the exact upper trace width. For the calculation of the characteristic impedance the upper and lower trace widths are assumed to be of the same value. The influence of the variation of the upper trace width is simulated with the tool in order to give an estimation for the characteristic impedance to be expected. The thickness  $t$  of the trace and the thickness  $h$  of the dielectric is defined by the used substrate. For Megtron6 it is

- $t = 30 \mu\text{m}$
- $h = 100 \mu\text{m}$ .

With all these parameters, the value for the characteristic impedance is calculated to  $Z_o = 47.33 \Omega$ . This lies well in the 10% tolerance range of  $45 \Omega$  to  $55 \Omega$ .

According to the datasheet of the Megtron6, the dielectric constant  $\epsilon_r$  changes over frequency (see subsection 4.2.1). As the dielectric constant  $\epsilon_r$  of the Megtron6 substrate varies between 3.61 and 3.71 depending on the frequency, the effect of the changing  $\epsilon_r$  should also be studied. The Si9000e tool provides the possibility to simulate the characteristic impedance versus a changing parameter. In Figure 4.27 the characteristic impedance  $Z_o$  is plotted against  $\epsilon_r$ . It can be seen that with higher effective dielectric constant the characteristic impedance decreases. The lowest values lies around  $47 \Omega$ , a change of 0.7%, which is still inside the 10% tolerance range.

Furthermore, the effect of changing the trace width on  $Z_o$  is studied and shown in Figure 4.28. This plot shows that for best matching of the impedance a trace thickness of around  $200 \mu\text{m}$  is the best choice. This result however does not take into account the real upper tracewidth.

For an estimation of the effect of the upper trace width on the impedance, a constant lower trace width of  $213 \mu\text{m}$  and  $\epsilon_r = 3.61$  is assumed, while varying the upper trace width

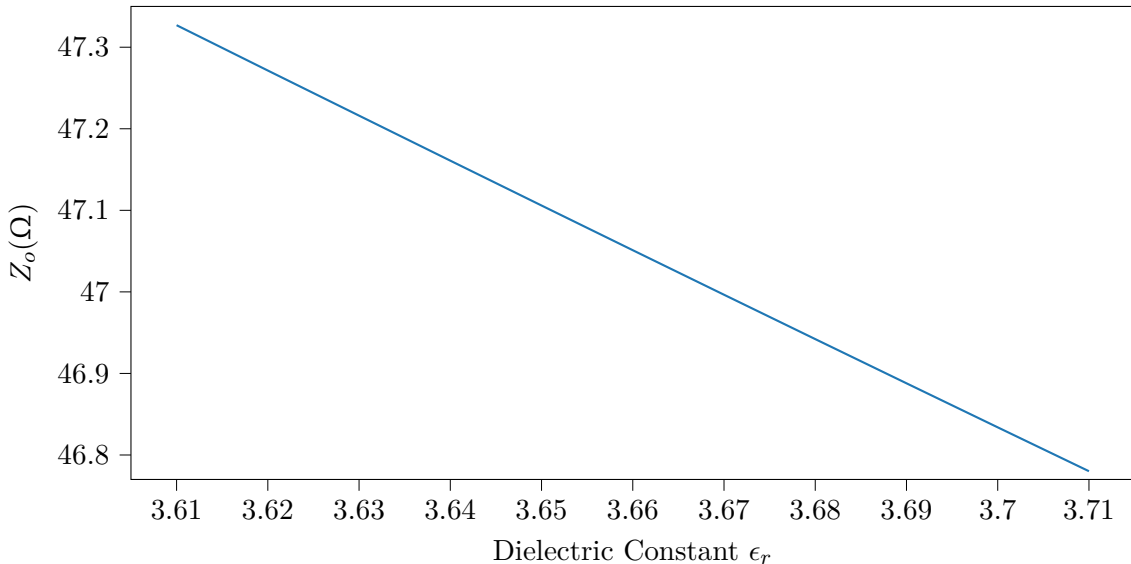


**Figure 4.27.** Characteristic impedance  $Z_o$  of a coplanar waveguide versus dielectric constant  $\epsilon_r$  assuming  $a = 213 \mu\text{m}$

from  $183 \mu\text{m}$  to  $213 \mu\text{m}$ . The result is shown in Figure 4.29. With decreasing width the characteristic impedance approaches the desired  $50 \Omega$ .

Figure 4.30 shows the calculated attenuation (combination of conductor and dielectric loss) of the coplanar waveguide with the given geometries over a frequency range 0.1 GHz to 100 GHz. This attenuation was calculated for the trace length of 10 mm, higher than the actually routed trace. As can be derived from the plot, the attenuation lies well below 1 dB, therefore ensuring high bandwidth of the trace.

### Differential Pairs on Surface

The geometry of the differential surface is similar to the waveguide type before, with the difference of having a pair of traces instead of one single trace (see page 70). The characteristic differential impedance  $Z_{\text{diff}}$  of this transmission line type is determined by the trace width  $w$ , the trace separation  $s$ , the trace-to-ground-separation  $d$ , the thickness of the trace  $t$  and thickness of the dielectric  $h$ .

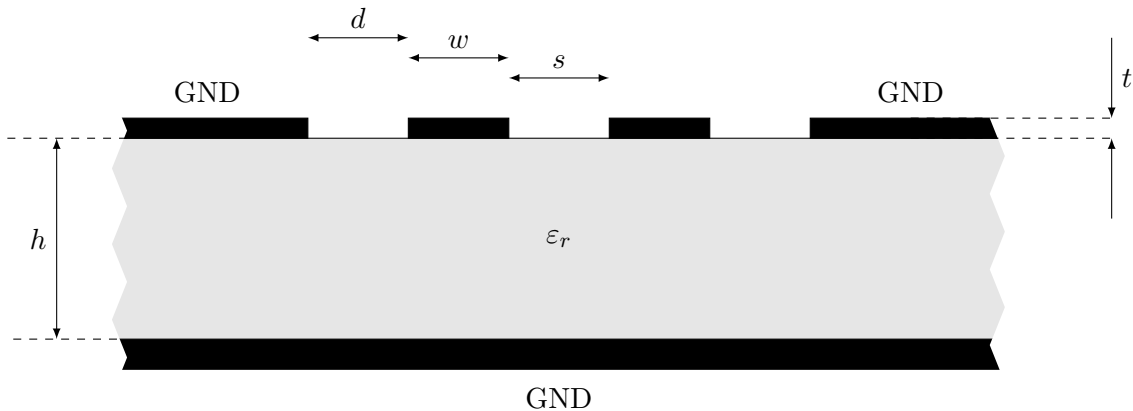


**Figure 4.31.** Edge-coupled differential coplanar waveguide

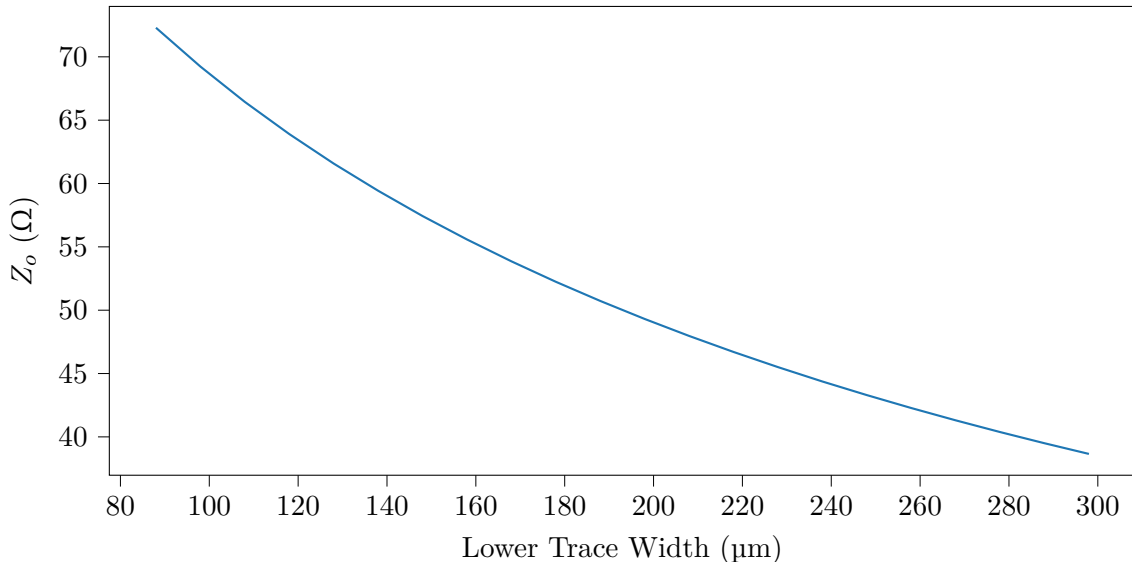


**Figure 4.28.**  $Z_o$  of a coplanar waveguide vs. lower trace thickness  $a$ , assuming  $\varepsilon_r = 3.61$

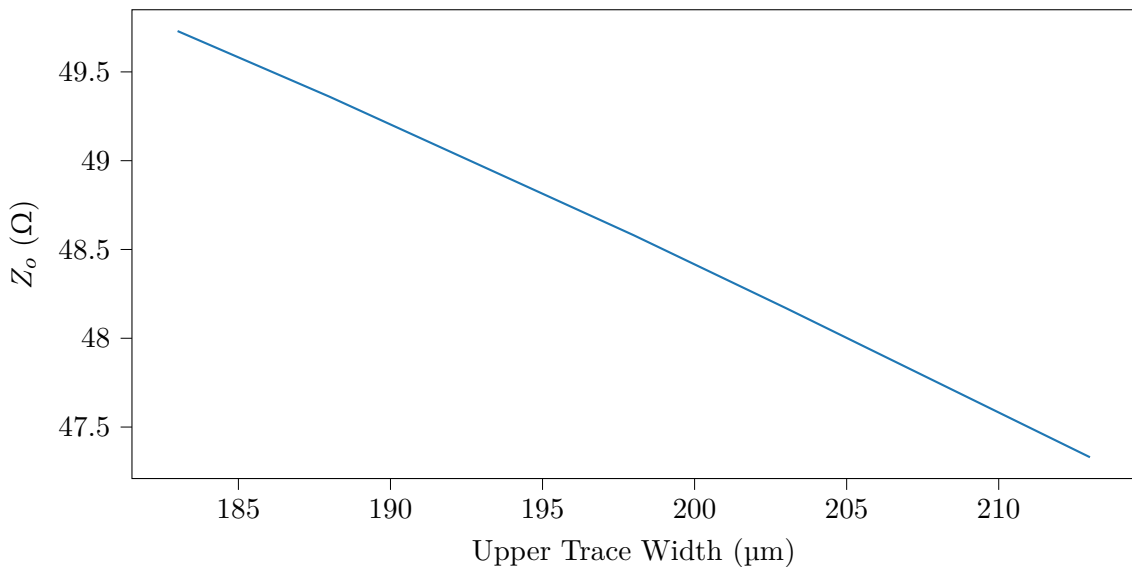


**Figure 4.29.**  $Z_o$  of a coplanar waveguide vs. upper trace thickness

The parameters  $t$  and  $h$  have the same value, as for the coplanar waveguide described below. For the other parameters first the following values are assumed:

- Trace width  $w = 180 \mu\text{m}$
- Trace separation  $s = 150 \mu\text{m}$
- Trace-to-ground separation  $d = 600 \mu\text{m}$

For these parameters and an  $\varepsilon_r = 3.61$  an impedance of  $92.35 \Omega$  is calculated with the Si9000e tool. This is still inside the tolerance band, but can potentially be improved.

In Figure 4.32 a the characteristic impedance  $Z_{\text{diff}}$  is plotted against the trace width<sup>9</sup>. The impedance  $Z_{\text{diff}}$  lies around  $100 \Omega$  for a trace width  $w \approx 155 \mu\text{m}$ .

Setting the width to  $155 \mu\text{m}$  indeed gives an impedance of  $Z_{\text{diff}} = 99.37 \Omega$ . The influence of the changing dielectric constant  $\varepsilon_r$  is studied in this case as well (see Figure 4.33). At the

<sup>9</sup>Assuming lower and upper trace width are equal.

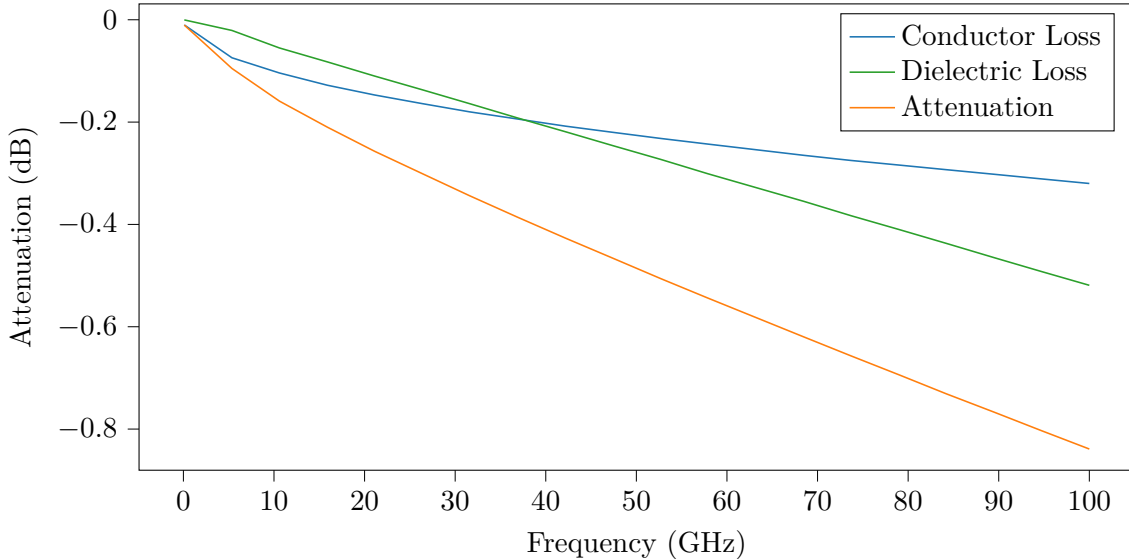


**Figure 4.30.** Attenuation per trace length of the surface coplanar waveguide over frequency simulated for trace length of 10 mm

maximal value of  $\varepsilon_r = 3.71$ , the impedance lies around  $98.4 \Omega$  corresponding to a change of 0.88 % compared to the value at  $\varepsilon_r = 3.61$ .

Furthermore, assuming  $\varepsilon_r = 3.61$  and a lower trace width  $w = 155 \mu\text{m}$ , the impedance over a varying upper trace width is plotted in Figure 4.34.

Figure 4.35 shows the calculated attenuation (combination of conductor and dielectric loss) of the coplanar waveguide with the given geometries over a frequency range 0.1 GHz to 10 GHz. This range is interesting as the signals propagated on these lines (e.g. clock signals) do not extend 10 GHz. This attenuation was calculated for the trace length of 50 mm, an estimation of the maximal length of such lines. As can be derived from the plot, the attenuation lies under 2 dB, which is an acceptable result for the design.

## Differential Pairs between Layers

The analog signals from the THAs, as well as the clock signals, are propagated through differential pair traces on the inner layers of the PCB. This forms a symmetrical differential coplanar waveguide as seen in Figure 4.36. The impedance of this waveguide type depends on the trace width  $w$ , the trace separation  $s$ , the trace-to-ground separation  $d$ , the thickness  $t$  of the trace, as well as the thickness of the dielectrics  $h_1$  and  $h_2$  and their respective dielectric constant  $\varepsilon_1$  and  $\varepsilon_2$ .

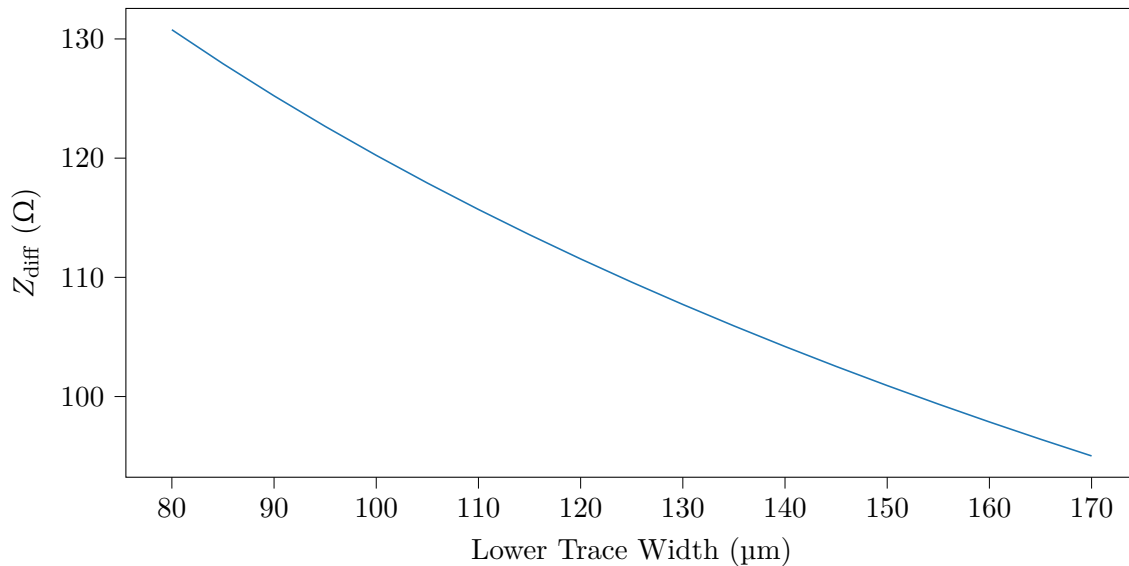


**Figure 4.32.**  $Z_{\text{diff}}$  of an edge-coupled differential coplanar waveguides. lower trace width  $w$ , assuming  $\epsilon_r = 3.61$

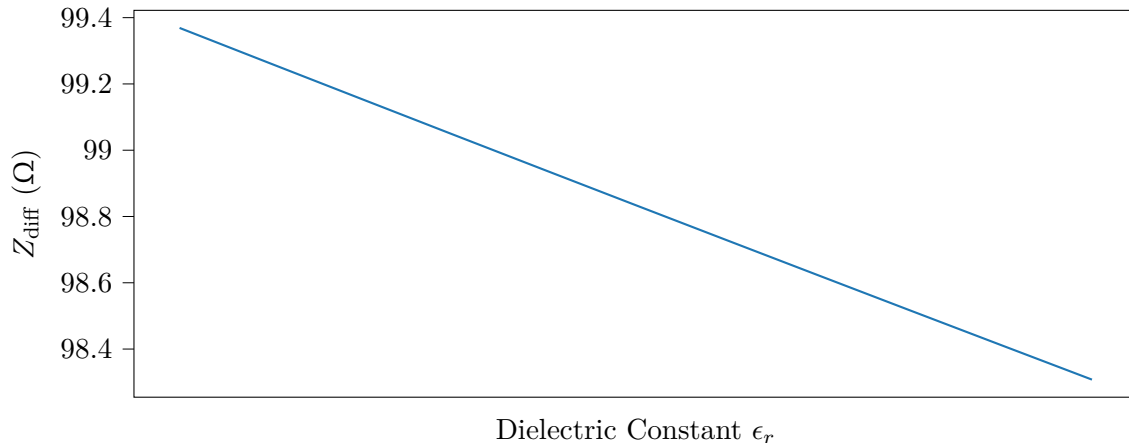


**Figure 4.33.**  $Z_{\text{diff}}$  of an edge-coupled differential coplanar waveguide vs. dielectric constant  $\epsilon_r$

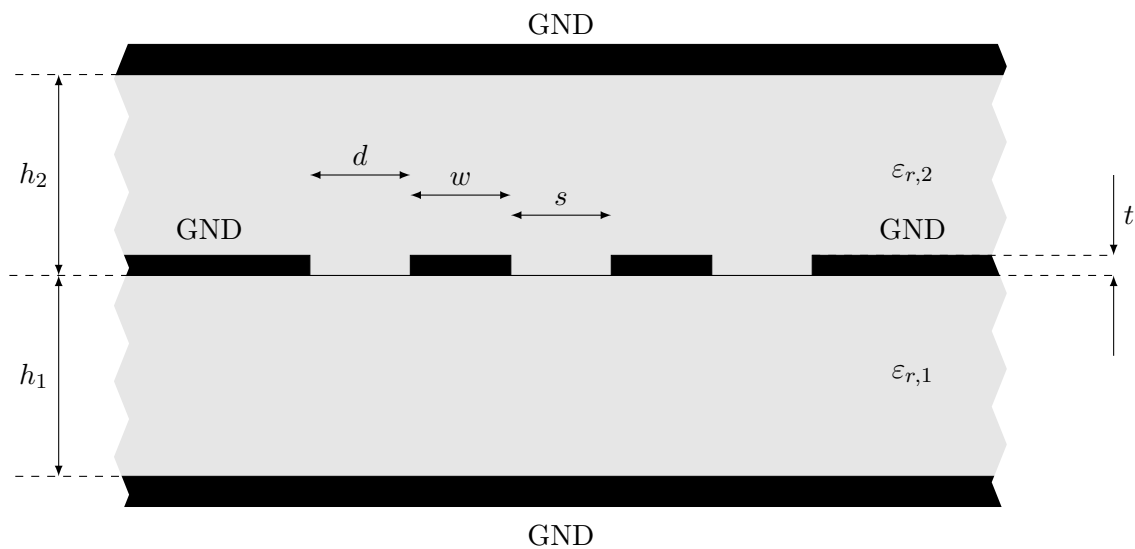


**Figure 4.36.** Symmetrical differential coplanar waveguide

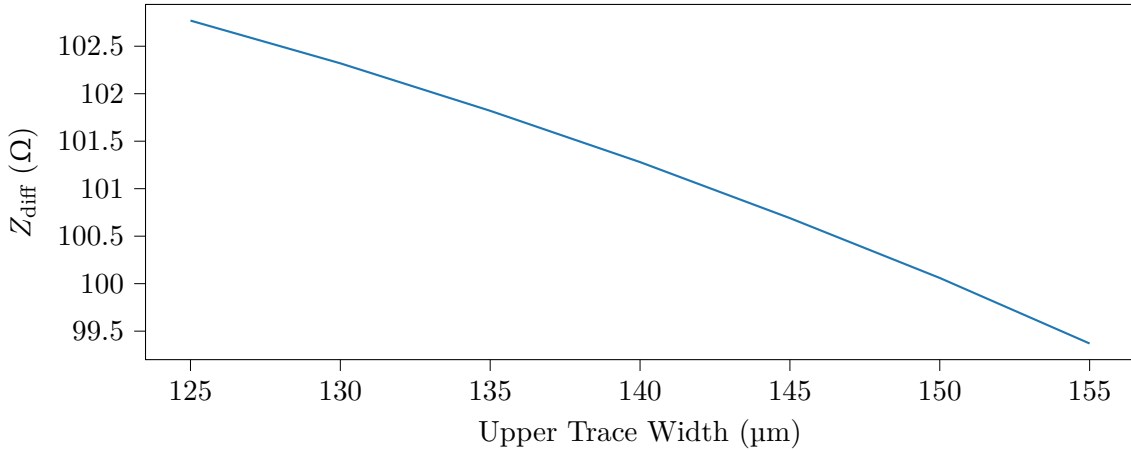


**Figure 4.34.**  $Z_{\text{diff}}$  of an edge-coupled differential coplanar waveguide vs. upper trace width, assuming lower trace width  $w = 155 \mu\text{m}$  and  $\varepsilon_r = 3.61$

The parameters are assumed as

- Trace width  $w = 88 \mu\text{m}$
- Trace separation  $s = 150 \mu\text{m}$
- Trace-to-ground separation  $d = 250 \mu\text{m}$

The thickness of the dielectrics is  $h_1 = h_2 = 150 \mu\text{m}$  and the dielectric constant is equal for both ( $\varepsilon_1 = \varepsilon_2 = \varepsilon_r = 3.61$ .) With these parameters the impedance is calculated as  $Z_{\text{diff}} = 90.40 \Omega$ . In Figure 4.37  $Z_{\text{diff}}$  is plotted against the trace width  $w$  (assuming upper trace width equal to  $w$ ). It can be seen, that in order to improve the impedance, one should decrease the trace width. Due to the manufacturing technology the minimal trace width possible is  $88 \mu\text{m}$ . Therefore this option is not feasible.

Keeping the trace width constant at  $w = 88 \mu\text{m}$  the trace separation could also be changed. Figure 4.38 shows  $Z_{\text{diff}}$  plotted against the trace separation  $s$ . It can be seen that  $Z_{\text{diff}}$  does not change significantly over a large range of  $s$ . For a trace separation of around  $300 \mu\text{m}$  (more than 3 times larger than the trace width itself)  $Z_{\text{diff}} \approx 94 \Omega$  and not significantly improved. Taking this into consideration, as well as the available space on the board, the parameters are left as is.

The influence of the dielectric constant  $\varepsilon_r$  is shown in Figure 4.39.  $Z_{\text{diff}}$  decreases with higher value of  $\varepsilon_r$  and even get below  $90 \Omega$ , exceeding the 10 % tolerance. However, the upper trace width has also to be taken into account, which is in any case smaller than the lower trace width due to the etching process during manufacturing. As Figure 4.40 shows, the impedance is potentially higher than calculated by assuming both width equal. Therefore the impedance can still be regarded as falling into the tolerance band.

Figure 4.41 shows the calculated attenuation (combination of conductor and dielectric loss) of the coplanar waveguide with the given geometries over a frequency range 0.1 GHz to 2 GHz. This attenuation was calculated for the trace length of 200 mm, an upper estimate of the length of the traces carrying the output signal from the THAs to the connector. As can be derived from the plot, the attenuation reaches up to 4 dB. Considering the length of the traces this is an expected result. The traces need therefore to be routed in the lowest noise conditions possible, i.e. through shielding by ground layers and placing via fences around the trace, to ensure that the signal under study is propagated correctly to the connectors. During characterization the

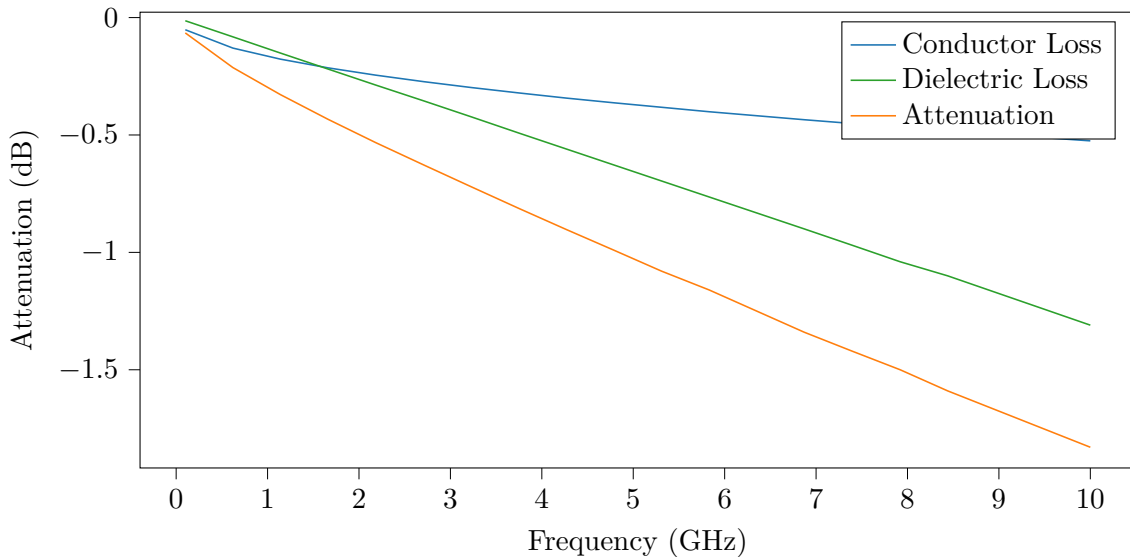


**Figure 4.35.** Attenuation per trace length of the surface differential coplanar waveguide over frequency simulated for trace length of 50 mm

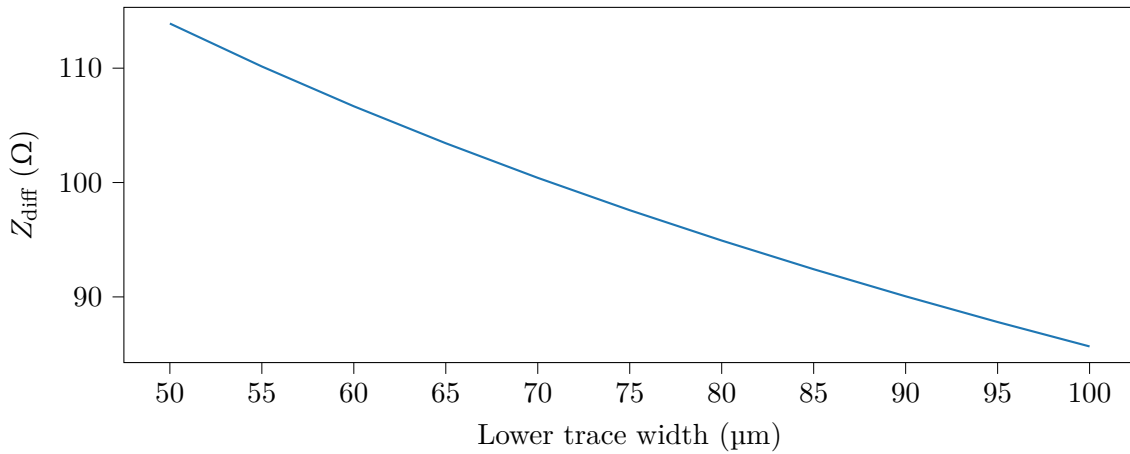


**Figure 4.37.**  $Z_{\text{diff}}$  of a symmetrical differential coplanar waveguide vs. lower trace width  $w$ , assuming upper trace width equals to  $w$

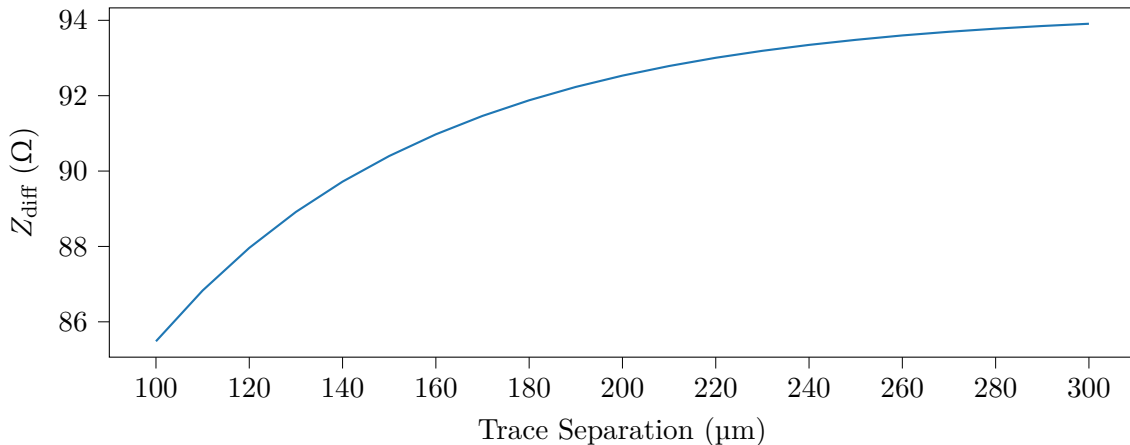


**Figure 4.38.**  $Z_{\text{diff}}$  of a symmetrical differential coplanar waveguides. trace separation  $s$ , assuming trace width  $w = 88 \mu\text{m}$

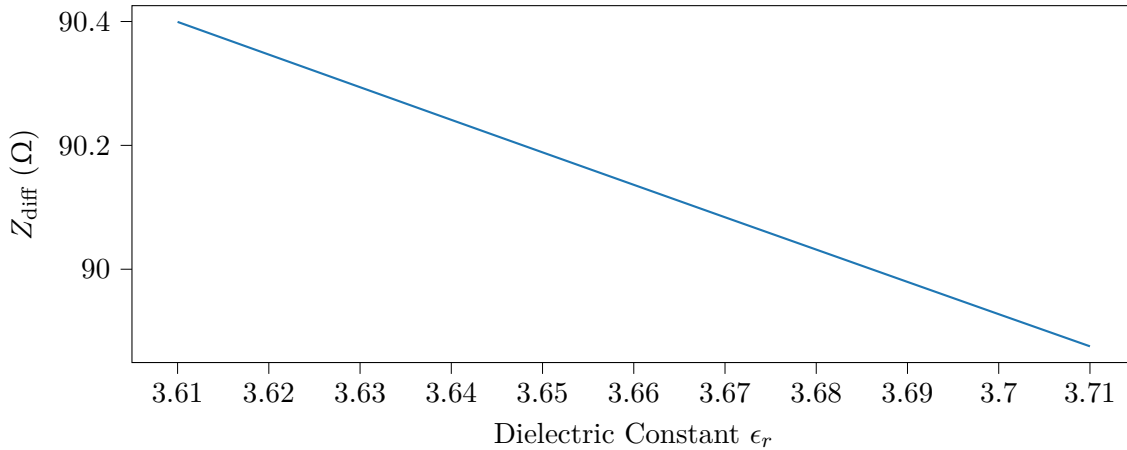


**Figure 4.39.**  $Z_{\text{diff}}$  symmetrical differential coplanar waveguide vs. dielectric constant  $\epsilon_r$ , assuming lower trace width  $w = 88 \mu\text{m}$  and  $\epsilon_r = 3.61$

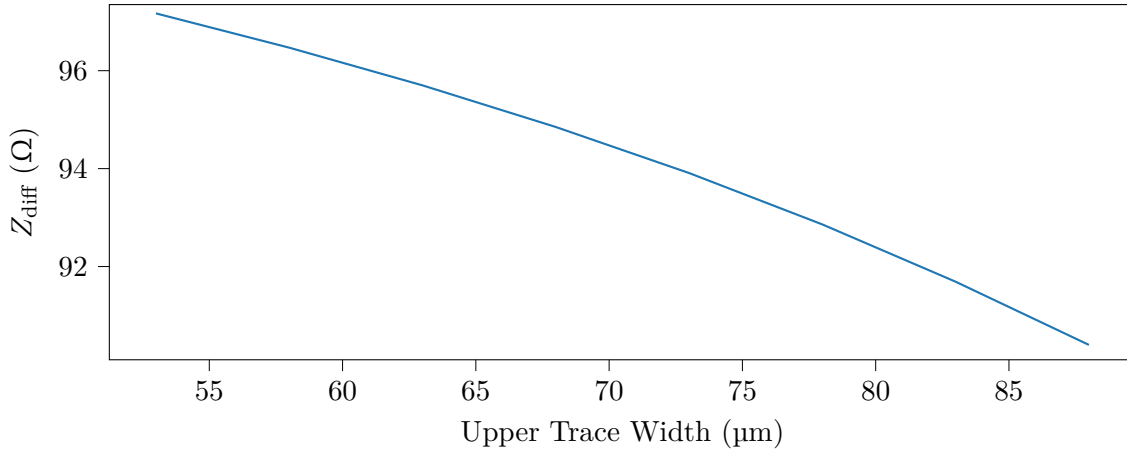


**Figure 4.40.**  $Z_{\text{diff}}$  Symmetrical differential coplanar waveguide vs. upper trace width, assuming lower trace width  $w = 88 \mu\text{m}$  and  $\epsilon_r = 3.61$

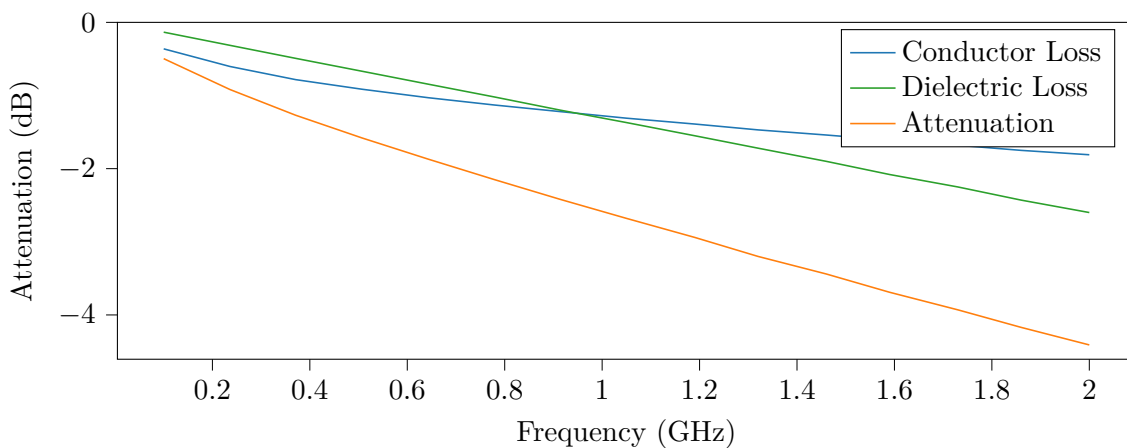


**Figure 4.41.** Attenuation per trace length of the symmetrical differential coplanar waveguide over frequency simulated for trace length of 200 mm

### 4.2.3. Component Placement and Routing

For the placement and routing of the components many steps need to be considered.

At the beginning, the separation of the analog and digital grounds has to be taken care of. Due to the complexity of the board, the respective grounds need to cover the whole plane. Therefore, in order to guarantee a full separation without any interference between the two parts, the PCB is split into two parts. The topside part is dedicated to the digital components and the routing of digital signal. These layers cover the clocking distribution as well as the slow control signal paths leading from the FPGA to the respective components. The bottomside part of the PCB is dedicated to the analog components and integrates the analog signal paths coming from the THAs.

Closely linked to the structuring of the overall PCB is the number of stacked-up metal layers used. In order to integrate all necessary signals and power planes, 16 layers in total are used. The topside 8 layers are therefore used for the digital part, the other 8 for the analog. For shielding purposes and to guarantee a small as possible signal return path for the transmission lines, layers carrying signal paths are “sandwiched” between two ground layers.

Some signals need to be routed from top layer to bottom and vice versa by through vias. In order to maintain the separation between analog and digital parts in such cases, a sufficient isolation between the via and the surrounding (ground) plane has to be ensured.

At some point, the analog and digital grounds need to be connected together. As mentioned in the section about the schematic capture, these connections are deployed by placing ferrite beads at each THA connecting analog and digital grounds. This way, any noise coming from the digital ground is compensated for. RF filtering at the THA is placed in the same manner, in order to mitigate any noise which could interfere with the sensitive analog signal.

Sensitive, i.e. analog components, should be placed first in order to minimize the routing paths, therefore reducing additional inductance and possible interference due to longer traces. Also the transmission lines carrying sensitive analog signals should be routed first, in order to define the further routing of other signal paths, e.g. slow control signals. These transmission lines should be separated from digital signal paths as much as possible in order to reduce cross-talk between the lines.

Routing the transmission lines should be done with time skew control in mind. This is especially necessary for the outputs leading from THAs to the RFMC connector. Due to the asymmetric position of the connector on the board, if the THA component outputs would be connected directly to the connector, the signal paths would vary significantly between components. This would introduce a significant time skew between the lines. Therefore, to account for this problem, signal paths coming from the closest THAs need to be made longer. This is achieved by routing the traces in patterns called “accordions”, which allow for prolonging the trace length in a compact way. An example for such accordions is shown in Figure 4.42.

To achieve high signal integrity, “via-fences” are placed next to the traces carrying analog signals. These consist of via holes connected to analog ground, placed close enough together to form a barrier for electromagnetic wave propagation. This forms a shield against any electromagnetic interference originating from other components on the board. Furthermore, via-fences act as a barrier also for the signal, therefore guiding it on the desired path and keeping it to its respective area.

Figure 4.44 shows the 3D model of the final design of the sampling card. On the top side (Figure 4.44a), the digital parts and clock distribution is placed. The clock distribution is

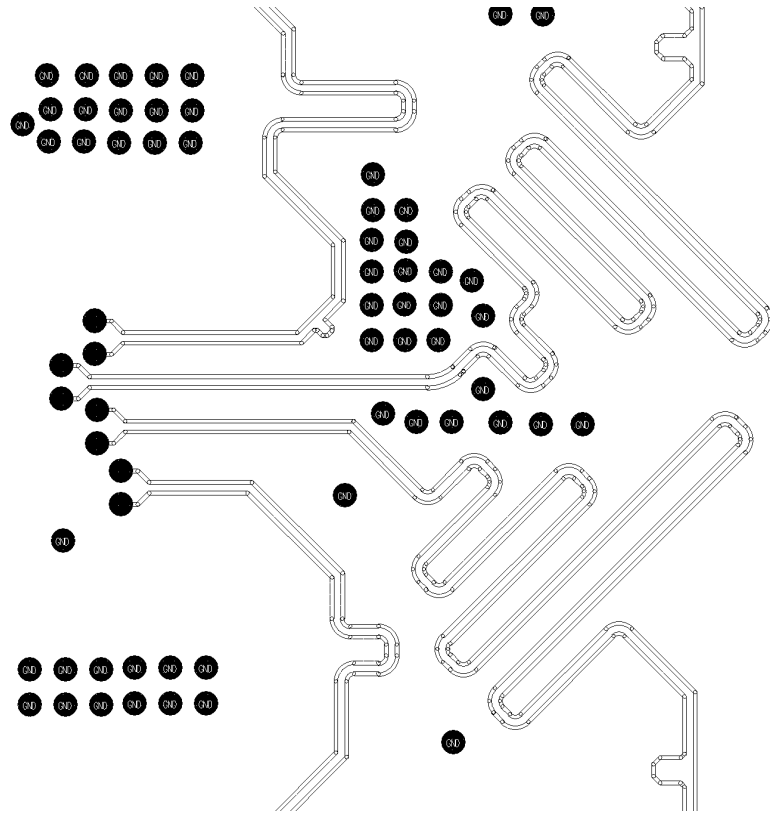


**Figure 4.42.** Example for trace accordions which are used to enlarge the trace length when little space is available

placed on the bottom, as close as possible to the THAs, with the main PLL in the middle. Two PLLs, providing the high frequency clock necessary for the data converters in the FPGA, are placed close to the main PLL. Furthermore, the FMC+ connector is located on the top, in order to connect the board with the FPGA and to provide the slow-control signals.

On the bottom (Figure 4.44b) side of the board, the analog components, i.e. the THAs and analog voltage regulators are placed. The output of the THAs is propagated to the RF connector (on the left in Figure 4.44b) which propagates the signal to the FPGA. To propagate test signals from the DACs on the FPGA, the connector on the right is used. The small connector on the top propagates the clock signal, coming from the high-frequency PLLs, to the data converters

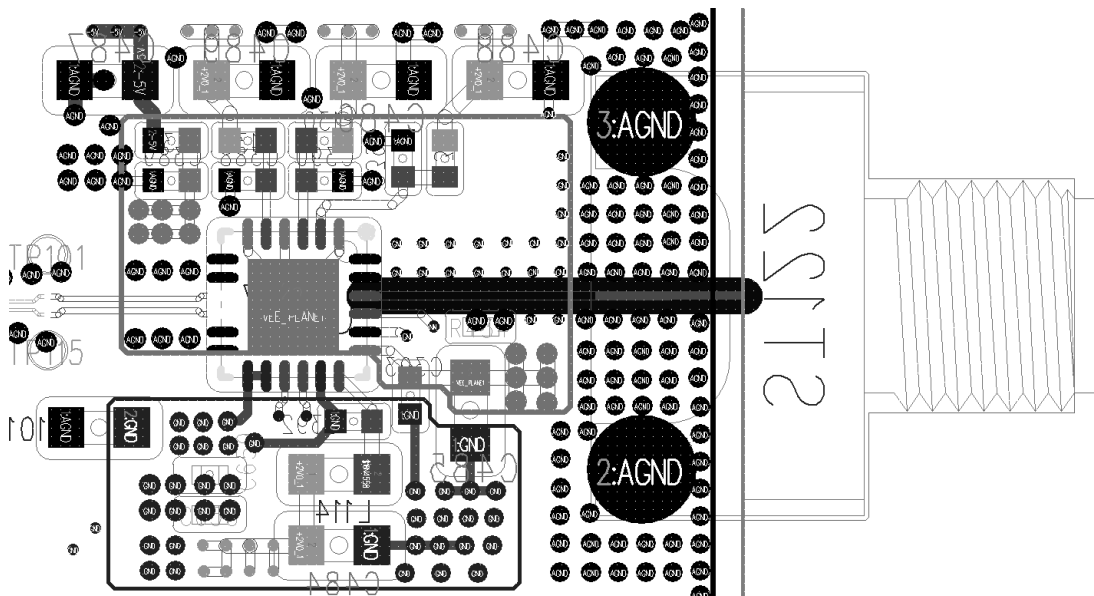


**Figure 4.43.** Layout of the THA, showing stitching vias and RF filtering components for low noise conditions

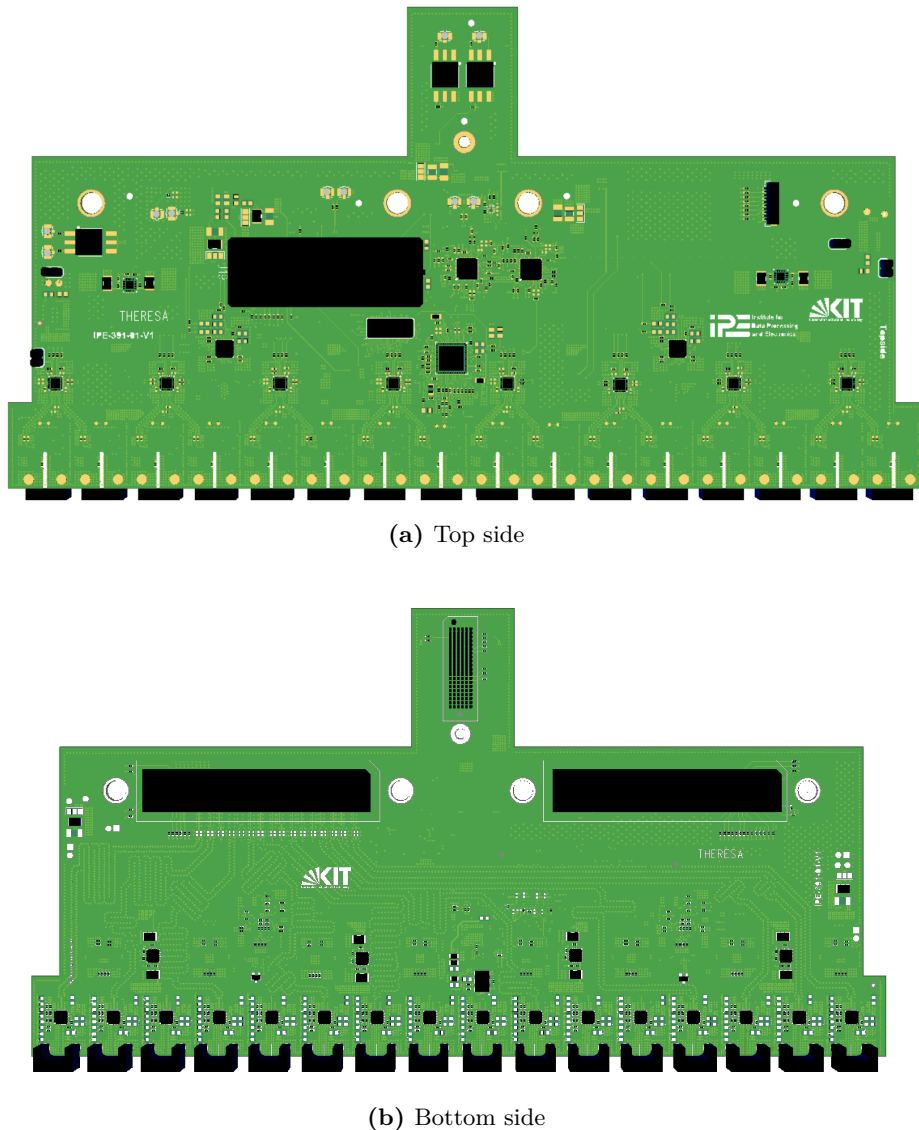


**Figure 4.44.** 3D model of the THERESA sampling card, showing the top and bottom side of the card

## 5. Back-End Readout Card and System Integration

The back-end readout card for the system under development, the Zynq UltraScale+ RFSoC ZCU216 Evaluation Card, has been chosen taking into consideration the points described in subsection 3.2.2. In this section, the overall architecture and features of the card are presented. A possibility for evaluation of the card is also demonstrated. At last, a design for the read-out firmware is proposed and an overview of the firmware elements is given.

### 5.1. Xilinx ZCU216 Evaluation Card

The ZCU216 Evaluation Card is equipped with the ZU49DR Zynq Ultrascale+ RFSoC (Gen 3). It allows for quick evaluation of the on-chip RF data converters and quick prototyping of different user-defined systems.

The features which are important for the designed read-out system are listed in the following (as seen in [Xilc]):

- Sixteen 14-bit, 2.5 GS/s RF-ADC
- Sixteen 14-bit, 10 GS/s RF-DAC
- I/O expansion options: FPGA Mezzanine Card (FMC+) interfaces, RFMC 2.0 interfaces, and Pmod (peripheral module) connections
- Double Data Rate Gen 4 (DDR4) Dual In-Line Memory Module (DIMM) – 4 GB, 64-bit, 2.666 MT/s, attached to the programmable logic (PL)
- DDR4 Small Outline Dual In-Line Memory Module (SODIMM) – 4 GB, 64-bit, 2.400 MT/s, attached to the processing system (PS)
- High-speed I/Os: 2 × 2 Small Form-Factor Pluggable (SFP)/SFP+/zSFP+/SFP28 modules
- Breakout cards for evaluation of the ADC and DAC performance, together with a clock add-on card for internal/external reference clocking

Other peripheral connections and features are shown in the top view of the board in Figure 5.1.

#### ZU49DR RFSoC

Together with an UltraScale+ programmable logic, the ZU49DR RFSoC integrates an ARM®Cortex™-A53 PS. This PS contains a 64-bit quad-core ARM®Cortex™-A53, serving as Application Processing Unit (APU), and a dual core ARM Cortex-R5F, serving as Real-Time Processing Unit (RPU). Furthermore, the system integrates RF data converters, allowing to use the system for RF applications. At the moment of writing, this is the industry's only single-chip, adaptable radio platform. [Xild]

Figure 5.2 shows the general block diagram of the RFSoC.

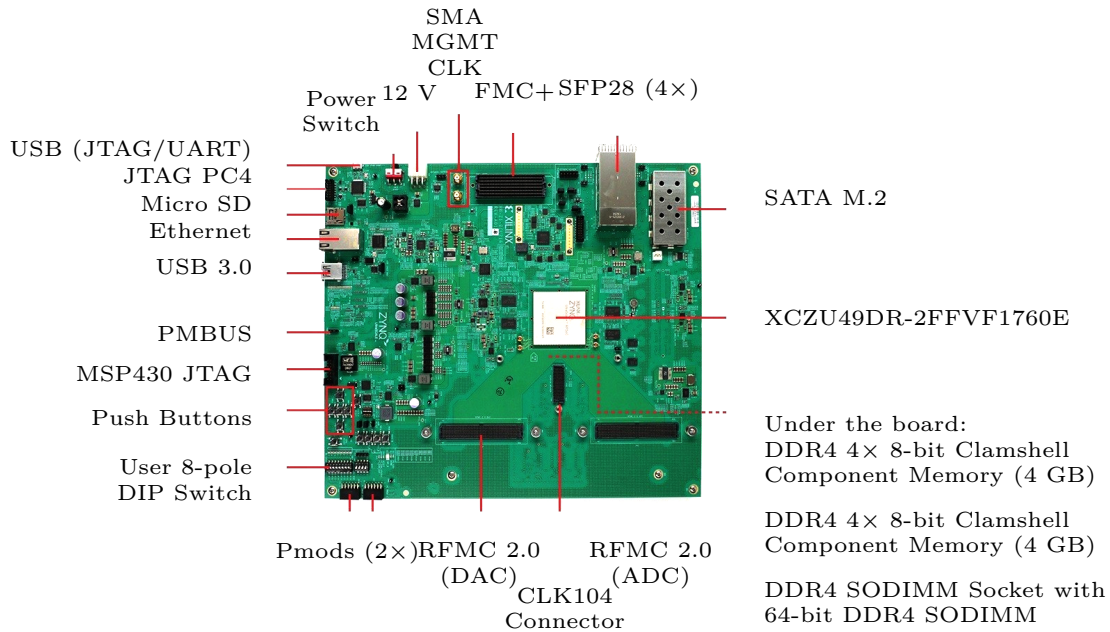


**Figure 5.1.** Topview of ZCU216 evaluation board with labeled components [Xilc]

## Evaluation Tool

In order to provide a quick evaluation of data converter performance an evaluation framework from *Xilinx* can be deployed on the card. The architecture of the tool is shown in Figure 5.3. [Xil20]

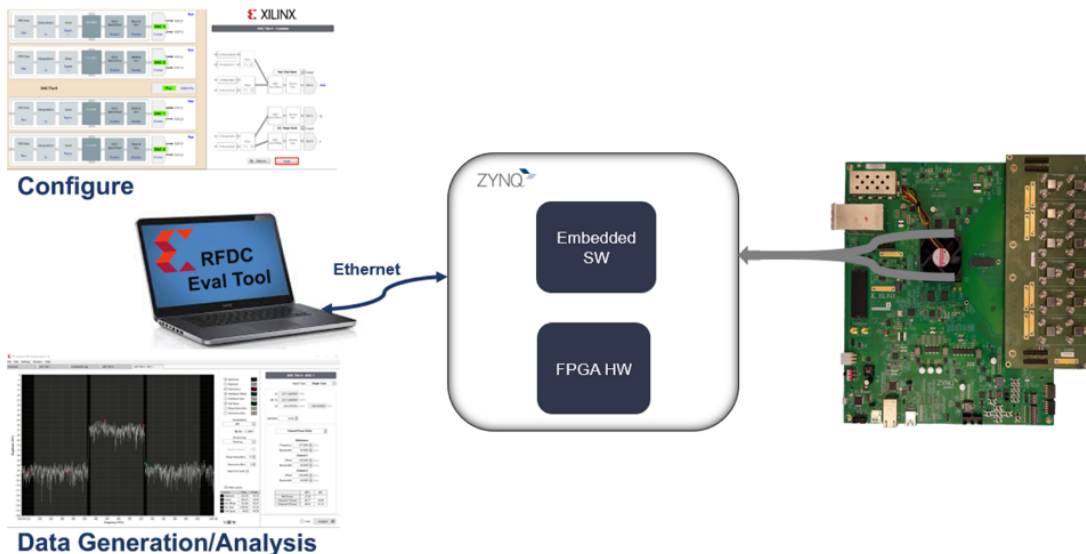


**Figure 5.3.** Concept of the Evaluation Tool for the ZCU216, showing the interactions between the host PC and the board [Xil20]

It enables control of the ZCU216 Intellectual Property (IP) cores and the associated designs from a host PC. With the tool, different RF configurations can be explored, RF data can be generated and captured and different RF metrics (see subsection 2.3.1) can be observed. [Xil20] For this, the breakout card provided with the board, or any other user-designed board, needs to be attached to the evaluation card via the RFMC connectors<sup>1</sup>.

<sup>1</sup>FMC connector for RF signals

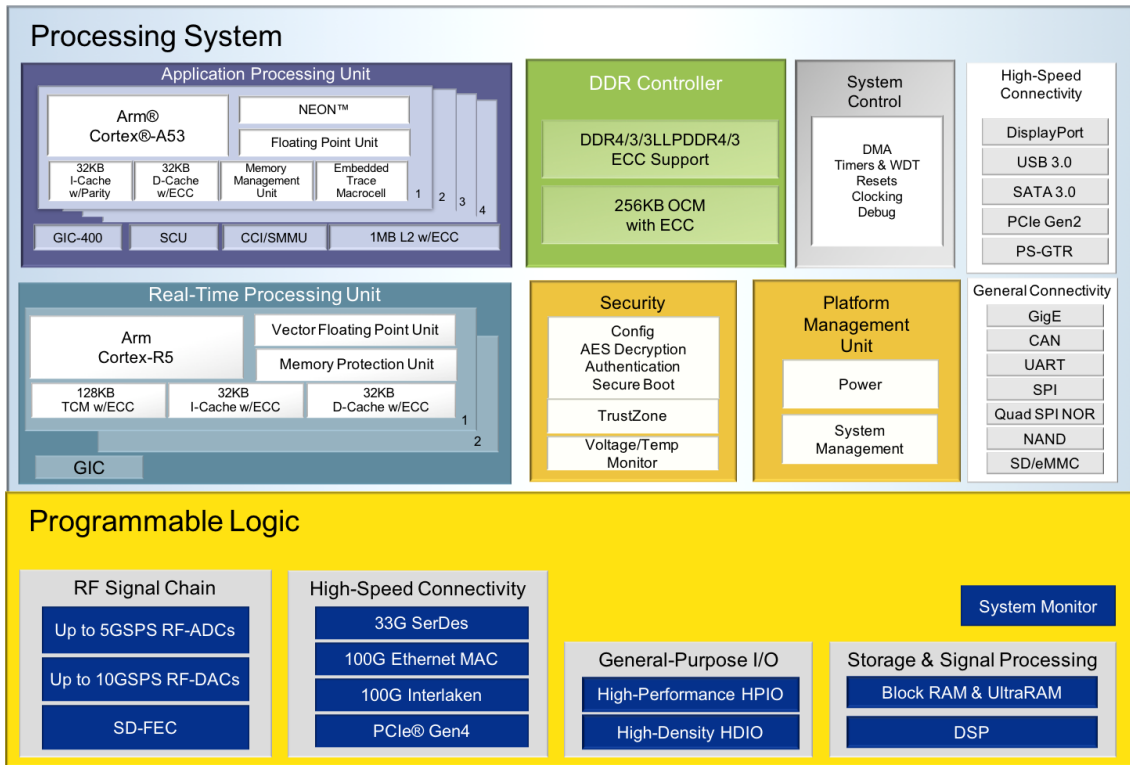


**Figure 5.2.** Zynq Ultrascale+ RFSoC block diagram, showing in detail the different components of the PS and PL

The RF DC (Data Converter) Evaluation Tool consists of two parts:

- Hardware design on the PL/FPGA, in order to implement the configuration and data generation/capture of the data converters. It is built around the RF Data Converter IP Core from Xilinx, described in section 5.2.
- Software design on the PS and host PC, in order to control the hardware implemented on the FPGA. On the PS a Linux application receives commands from the host PC Graphical User Interface (GUI) over Ethernet. Based on the commands, it performs the according action, e.g. setting the sampling clock or enabling/disabling data converter channels. The GUI provides a convenient possibility to configure the data converters. Data generation via DACs can be started, as well as data capture with the ADCs. Furthermore, the tool provides methods to quickly characterize the performance of the data converters (see Figure 5.4) from which the performance of the plugged break-out board can be derived.

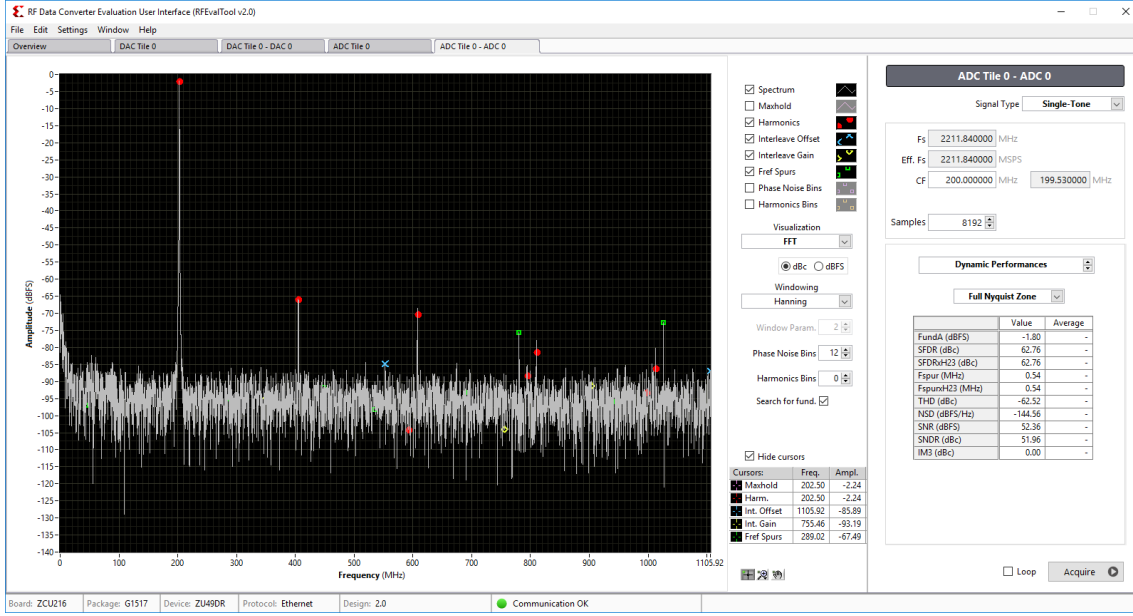


**Figure 5.4.** GUI of the RF Data Converter Evaluation Tool

## 5.2. Firmware

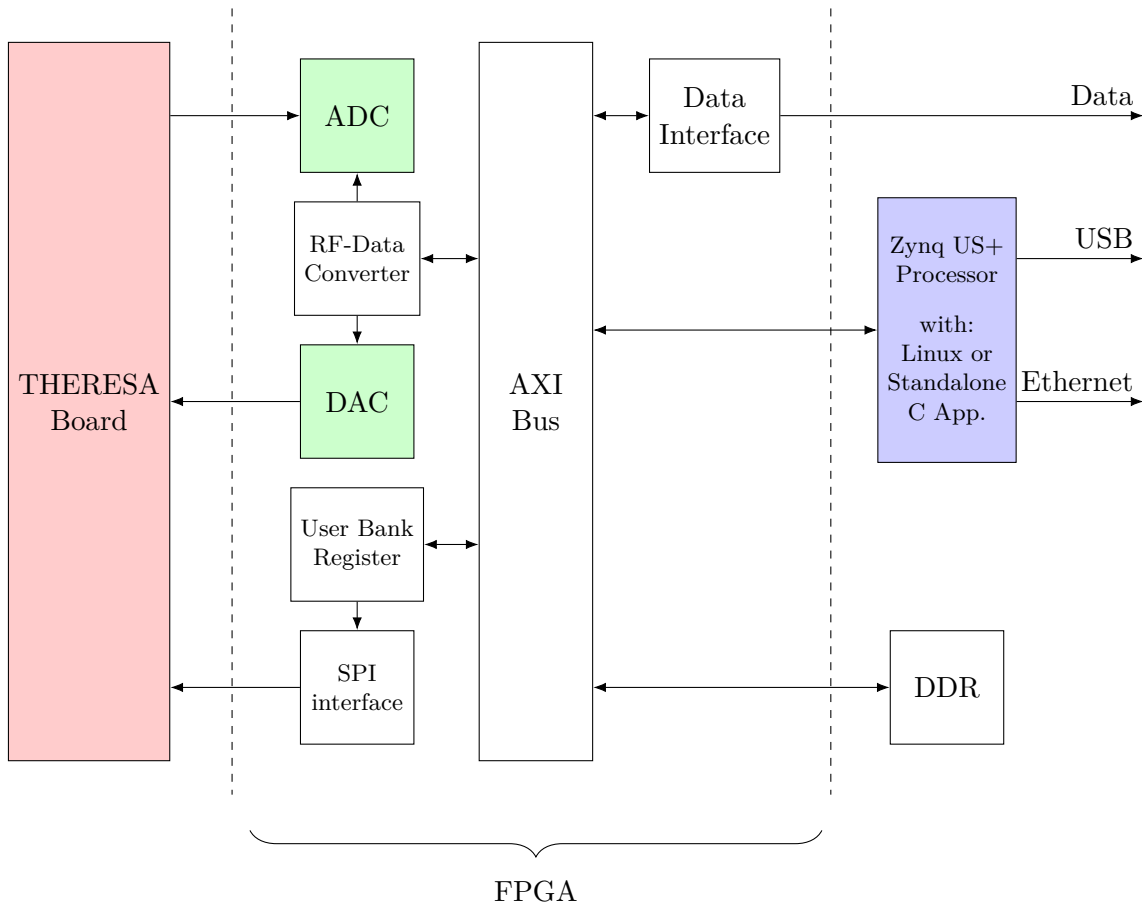
Similar to the evaluation tool, the firmware for the readout system should contain a software part on the PS which allows for control and configuration of the data converters. The hardware design part should implement the interface to the sampling board. This means it should provide the necessary interfaces to configure the data converters on the readout card, as well as slow control to the delay chips and PLLs on the sampling board (i.e. through SDI and SPI). Furthermore, the high-speed data-throughput interface should be implemented.

Figure 5.5 shows the general schematic of the firmware on the readout card.

The sampled data is propagated from the sampling card to the ADCs inside the FPGA. This data is written in the Double Data Rate (DDR), from which it is accessible by the data interface, which is responsible for the high-speed data transfer to the following processing node in the DAQ system. A built-in test-loop is implemented with an integrated DAC, in order to produce test signals which are propagated to the sampling board. Configuration of the data converters is done via the Xilinx “RF Data Converter” which is described below.

Components on the sampling board, such as the delay chips, are controlled via a SPI interface. This interface is connected to a user bank register, where the user can specify e.g. the desired delay values.

The PS communicates with the PL via Advanced eXtensible Interface (AXI). AXI is a parallel, synchronous, multi-master, multi-slave communication interface. On the PS an operating system, e.g. Linux, or a standalone C application, can run implementing functionalities for the user to be able to control the overall system. Access to the PS is provided by for example via Ethernet or USB.



**Figure 5.5.** Schematic of the firmware and processing unit on the readout card

### 5.2.1. Programmable Logic - Hardware design

For synthesis and analysis of the Hardware Description Language (HDL) design for the PL, the Integrated Design Environment (IDE) *Xilinx Vivado IDE* is used. To configure and control the data converters, the RF Data Converter IP Core from Xilinx is used. In order to program the components on the sampling board, appropriate SPI interfaces are implemented, respecting the recommendations in the data sheet.

#### RF Data Converter IP Core

In order to configure the data converters, the HDL design should be based around the Xilinx RF Data Converter IP Core. The IP core provides a configuration screen, which is used to

- enable the data converter tiles
- configure decimation, interpolation and mixing
- set up the sampling rates, PL word widths and data types
- enable optional interface ports.

Handling of the configuration and power-up of the data converters is covered by the IP core. Figure 5.6 shows a simple design example. It implements the RF Data Converter IP core, which configures one DAC to generate data and one ADC to capture incoming data.

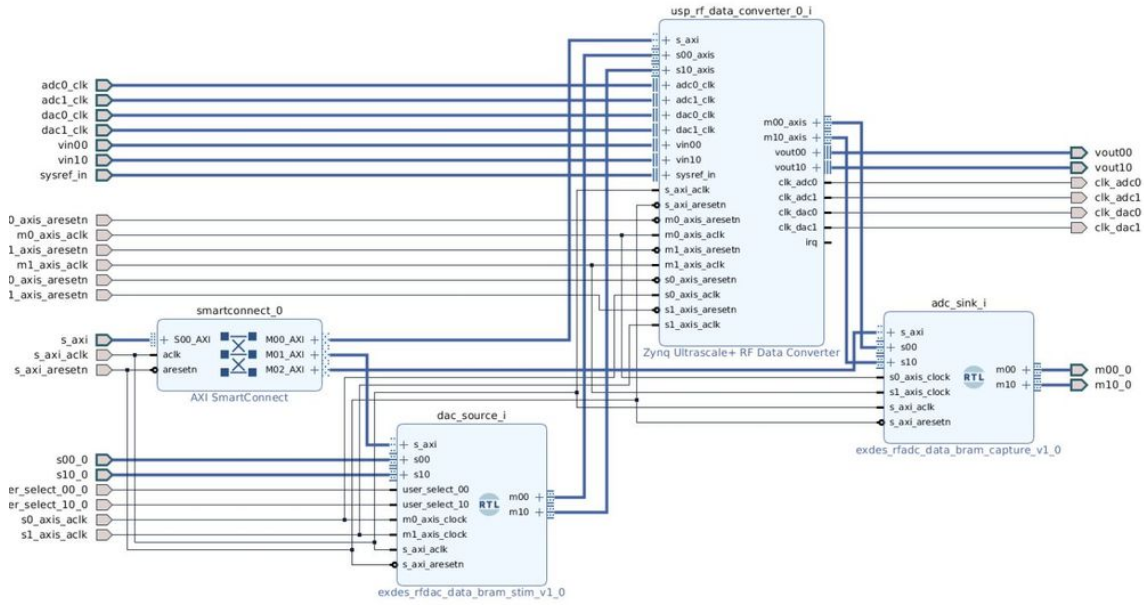


**Figure 5.6.** Simple example design with the RF Data Converter

## Slow Control

Components on the sampling board are controlled via a slow control interface. As example, the on-board delay chips are controlled via a SDI interface, consisting of four signals: EN, SDIN, SCLK and SLOAD. In order to program a certain delay, the timing diagram shown in Figure 5.7 has to be respected. The delay chip only accepts data when the EN input is HIGH. Therefore, this signal has to remain high in the course of the whole data transaction. The data pin, SDIN, which is clocked in by the SCLK signal, has to respect the following structure: delay channel select bit, mode select bit, followed by 9 data bits, which represent the desired delay value in binary format. At the end, SLOAD has to be asserted HIGH, in order to signal the chip to load the received data into the chip's internal register. The HDL implementation for this interface is listed in section B.

In a similar way, the interface for other components is to be implemented.

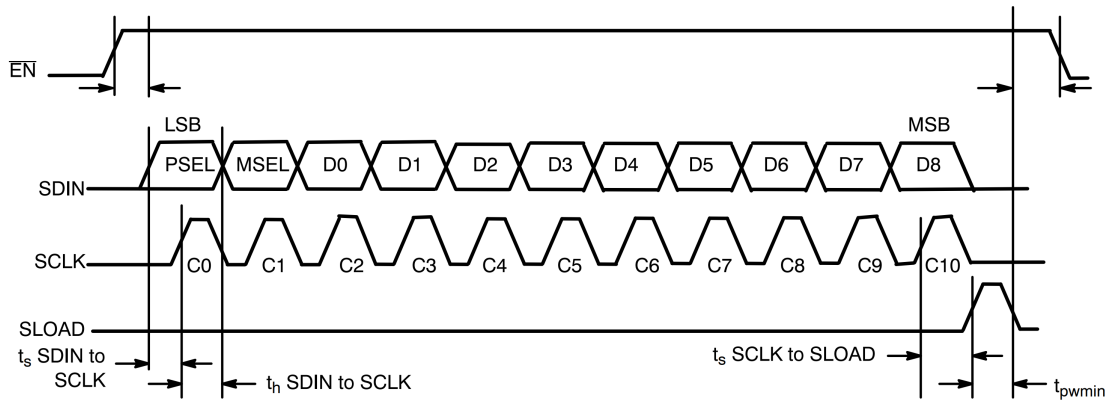


**Figure 5.7.** SDI timing diagram for the NB6L295 delay chip [ONS]

### RDMA over Converged Ethernet (RoCE)

The high speed data interface is implemented using the RDMA over Converged Ethernet (RoCE).

Remote Direct Memory Access (RDMA) allows direct memory access from one computer to another over an Ethernet network. This permits high-throughput, low-latency communication between applications which are hosted on clusters of servers or storage arrays.

RoCE is a network protocol defined in the InfiniBand Trade Association (IBTA) standard, allowing RDMA over converged Ethernet network. It allows devices to perform direct memory access between each other without involving the host CPU. The transport processing and memory translation are performed by hardware. RoCE has the benefits of the RDMA technology and the ease of use and availability of Ethernet.

The ERNIC (Xilinx Embedded RDMA enabled NIC) IP provides an Initiator and Target implementation of RDMA over Converged Ethernet Version 2 (RoCEv2) enabled Network Interface Controller (NIC) functionality. This IP is specifically designed for embedded applications that require reliable transmission over Ethernet networks.

Figure 5.8 shows a possible working principle of a system with multiple host CPUs and multiple native Non-Volatile Memory Express (NVMe)<sup>2</sup> devices talking over a network fabric through the Xilinx Xilinx Embedded RDMA enabled NIC (ERNIC) IP subsystem. [Xilb]

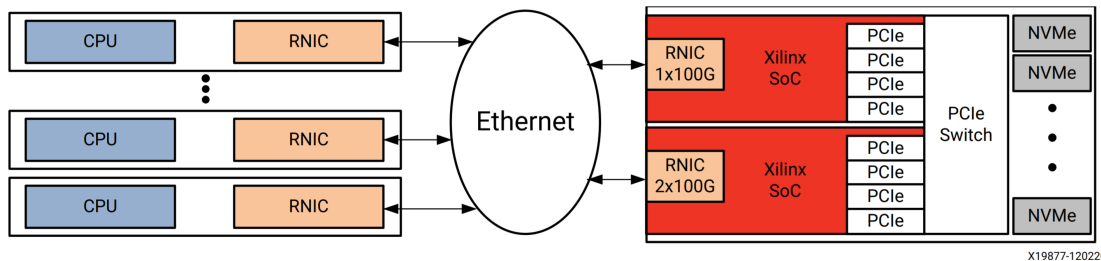


**Figure 5.8.** Xilinx ERNIC working principle example [Xilb]

#### 5.2.2. Processing Unit - Software Design

In order for the user to be able to control the whole system, some kind of application has to be implemented for control of the hardware design. For this the PS side of the RFSoC is used. The ARM Cortex processor allows to implement standalone C application, as well as hosting an operating system like Linux. Providing a number of peripheral connections, like Ethernet or USB, the PS can easily be accessed by the user from another host computer, given the necessary drivers and protocols are implemented. The aforementioned evaluation tool for example uses the Linux application *rftool* in order to receive commands and perform the according action.

For interaction and monitoring of the data converters the RFdc driver Application Programming Interface (API) needs to be used. It is available both as bare-metal and Linux driver and includes functionalities to respond to interrupt, change settings (e.g. mixer frequency of the data converters) and interaction with the RF Data Converter IP.

For interaction and monitoring of the data converters, the RFdc driver API needs to be used. It is available both as bare-metal and Linux driver and includes functionalities to

<sup>2</sup>NVMe is an open, logical-device interface specification for accessing a computer's non-volatile storage

respond to interrupt, change settings (e.g. mixer frequency of the data converters) and interaction with the RF Data Converter IP

In order to implement and build software applications, the novel *Xilinx Vitis* unified software platform is used. It enables the development of embedded software and accelerated applications on heterogeneous *Xilinx* platforms including FPGAs and SoCs. It offers APIs and libraries for accelerated development of software applications for the system under development. The applications can be programmed with common languages like C, C++, and Python.

## 6. Summary and Outlook

Analysis of events occurring in the time range of femtoseconds is necessary in many scientific experiments. Continuous measurement of such events over a long period of time is desired in order to study the long-term evolution of such events. With currently commercially available Data Acquisition System (DAQ) this is not possible due to the high sampling rates required and the limited memory space of such systems.

In this thesis, a first demonstrator of a new type of DAQ has been developed to overcome these limitations. The system consists of a high bandwidth front-end sampling card, mounted on a back-end card integrating a new generation of Radio-Frequency System-On-Chip (RFSoC) for continuous readout of the acquired samples. It is based on the photonic time-stretch method, using chirped laser pulses and dispersion in fibers to stretch the signal under study in time. In this way, the signal can then be measured with a lower sampling rate than would usually be needed to measure events with a duration of several femtoseconds. The name given to the system is Terahertz Readout Sampling (THERESA).

The THERESA front-end sampling card integrates 16 sampling channels, each containing a Track-And-Hold-Amplifier (THA) and an Analog-To-Digital-Converter (ADC) (integrated in the RFSoC) with individually programmable delay (step size 11 ps) in sampling time. With this setup, the so called time-interleaving technique can be implemented. This allows to sample the signal at higher sampling rate than one single data converter can achieve.

The design of the board allows it to be used either with the time-stretch setup or independently from it. In single-channel mode one detector is connected to one sampling channel, therefore allowing sampling of up to 16 detectors at the same time with one sampling point per channel. In the second mode, several channels are connected to one detector via power-splitter, therefore allowing multiple sampling points for one detector per channel by setting the delay times accordingly.

High-speed ADCs, integrated in the RFSoC, with 14-bit resolution and a sample rate of up to 2.5 GS/s allow continuous sampling of the signal with high time resolution. Using the time-interleaving technique for all sixteen ADCs results in an overall maximal achievable sample rate of 40 GS/s. When used in combination with the time-stretch method and considering typical stretch-factors the signal can be sampled with a time resolution corresponding to hundreds of femtoseconds in the original signal.

The sampling card has furthermore been designed to fully exploit all the features of the RFSoC, which integrates a processing unit together with a Field Programmable Gate Array (FPGA). The on-chip FPGA provides the possibility to flexibly adjust the firmware to user needs. Slow-control implemented in the FPGA takes care of programming the components on the sampling card, such as the delay chips. The acquired samples are intermediately stored in the on-board Double Data Rate (DDR), where they can be accessed by the high-speed data interface. This interfaces allows transfer speeds over 100 Gb/s, are a crucial component for the high throughput of the large amount of data continuously

generated by the data converters. The processing unit can host for example an operating system and communicate with the firmware on the FPGA. Over common periphery, such as Ethernet, the user can access and control the overall system.

With the evaluation tool provided by the manufacturer a quick set-up and measurement of key data converter performance characteristics (e.g. Signal-to-Noise-and-Distortion Ratio (SINAD) or Spurious-Free Dynamic Range (SFDR)) is possible. Together with provided add-on cards, a first evaluation of the data converter performance has been possible.

The design of the sampling card was approved by the Institute for Data Processing and Electronics (IPE) and the card is currently in production. It has been shown, that the evaluation tool provided for the readout card allows to perform the necessary measurements (see subsection 2.3.1) for a quick characterization of the sampling card. THERESA will then be commissioned and taken into operation, improving the research in various scientific fields, especially beam diagnostics at e.g. at Karlsruhe Research Accelerator (KARA). There it can be used for studying Coherent Synchrotron Radiation (CSR), in the far-field and near-field Electro-Optic (EO) setup, for study of fast laser dynamics and many other applications. The selected FPGA is powerful and suitable for deploying Artificial Intelligence (AI) applications (i.e. reinforcement learning). Therefore the system can also be used for interfacing with the Bunch-By-Bunch feedback at KARA. In the context of the Exploration et contrôle ULTRArapide de la dynamique des paquets d'électrons dans les sources de lumière SYNChrotron (ULTRASYNC) project, funded by Agence Nationale de la Recherche (ANR) and Deutsche Forschungsgemeinschaft (DFG), THERESA can be used to study the control of electron bunches in accelerators at KARA and Source optimisée de lumière d'énergie intermédiaire du LURE (SOLEIL).

Therefore the newly developed THERESA system is an important step towards new usable Terahertz (THz) sources and can be deployed to improve beam diagnostics at several renowned facilities.

# Acknowledgments

First, I would like to thank Prof. Anke-Susanne Müller from the Institute of Beam Physics and Technology for being my first reviewer.

I want to express my sincere appreciation for my advisor Dr. Michele Caselle for always being a great support and an excellent teacher, who always has time to explain all details, even if it concerns fundamental topics. His great support at all times made the successful conclusion of this thesis and my studies possible.

Prof. Serge Bielawski from Lille University I would like to thank for the collaboration and the useful feedback concerning the system.

I would also like to thank Andreas Kopmann (IPE) for his support during the writing of this thesis and the preparation of the final defence.

Michael Schleicher (IPE) I would like to thank for his useful advice and help during the design phase of the card layout.

My biggest gratitude also goes to Meghana Patil (LAS) for her support at all times, especially during the last phase of writing and preparation of my presentation.

I would like to thank Miriam Brosi (IBPT) for giving me the possibility to see the KARA facility from inside and for prove-reading my thesis.

I am eternally grateful to Marvin Noll for his invaluable support not only during the writing of the thesis (especially concerning LaTeX-related questions) and the preparation of the final defense, but also for his great support at any times during the whole course of my studies.

Finally, I would like to thank my parents for always supporting me in any situations at all times. I owe them my biggest appreciation for successfully completing my studies, without their support and care this would have never been possible.



# Appendix

## A. Characteristic Impedance Of Coplanar Waveguides

### Edge-Coupled Coplanar Waveguide

Characteristic impedance (see [Wad91, p197-198]):

$$Z_{0,o} = \frac{\eta_0}{\sqrt{\epsilon_{\text{eff},o}}} \left( \frac{1.0}{2.0 \frac{K(k_o)}{K'(k_o)} + \frac{K(\beta_1)}{K'(\beta_1)}} \right) \quad (\text{A.1})$$

$$Z_{0,e} = \frac{\eta_0}{\sqrt{\epsilon_{\text{eff},e}}} \left( \frac{1.0}{2.0 \frac{K(k_e)}{K'(k_e)} + \frac{K(\beta_1 k_1)}{K'(\beta_1 k_1)}} \right) \quad (\text{A.2})$$

$$\epsilon_{\text{eff},o} = \frac{2.0 \epsilon_r \frac{K(k_o)}{K'(k_o)} + \frac{K(\beta_1)}{K'(\beta_1)}}{2.0 \frac{K(k_o)}{K'(k_o)} + \frac{K(\beta_1)}{K'(\beta_1)}} \quad (\text{A.3})$$

$$\epsilon_{\text{eff},e} = \frac{2.0 \epsilon_r \frac{K(k_e)}{K'(k_e)} + \frac{K(\beta_1 k_1)}{K'(\beta_1 k_1)}}{2.0 \frac{K(k_e)}{K'(k_e)} + \frac{K(\beta_1 k_1)}{K'(\beta_1 k_1)}} \quad (\text{A.4})$$

with

$$k_o = \Lambda \frac{-\sqrt{\Lambda^2 - t_c^2} + \sqrt{\Lambda^2 - t_B^2}}{t_B \sqrt{\Lambda^2 - t_c^2} + t_c \sqrt{\Lambda^2 - t_B^2}} \quad (\text{A.5})$$

$$k_e = \Lambda' \frac{-\sqrt{\Lambda'^2 - t_c'^2} + \sqrt{\Lambda'^2 - t_B'^2}}{t_B' \sqrt{\Lambda'^2 - t_c'^2} + t_c' \sqrt{\Lambda'^2 - t_B'^2}} \quad (\text{A.6})$$

$$\Lambda = \frac{\sinh^2 \left( \frac{\pi(s/2.0+w+d)}{2.0h} \right)}{2} \quad (\text{A.7})$$

$$t_c = \sinh^2 \left( \frac{\pi(s/2.0+w)}{2.0h} \right) - \Lambda \quad (\text{A.8})$$

$$t_B = \sinh^2 \left( \frac{\pi s}{4.0h} \right) - \Lambda \quad (\text{A.9})$$

$$\Lambda' = \frac{\cosh^2 \left( \frac{\pi(s/2.0+w+d)}{2.0h} \right)}{2} \quad (\text{A.10})$$

$$t'_c = \sinh^2 \left( \frac{\pi(s/2.0 + w)}{2.0h} \right) - \Lambda' + 1.0 \quad (\text{A.11})$$

$$t'_B = \sinh^2 \left( \frac{\pi s}{4.0h} \right) - \Lambda + 1.0 \quad (\text{A.12})$$

The parameters have to be chosen according to

$$s + 2.0w + 2.0d \leq h \quad (\text{A.13})$$

to guarantee coplanar propagation. [Wad91]

### Surface Coplanar Waveguide with Ground

The characteristic impedance of a coplanar waveguide is given as (see [Wad91])

$$Z_0 = \frac{60.0\pi}{\sqrt{\epsilon_{\text{eff}}}} \frac{1.0}{\frac{K(k)}{K(k')} + \frac{K(k_1)}{K(k'_1)}}. \quad (\text{A.14})$$

It comprises of the following components, with  $K(k)$  being an elliptical integral of the first kind (see also [BSMM99, p. 430]):

$$k = a/b \quad (\text{A.15})$$

$$k' = \sqrt{1.0 - k^2} \quad (\text{A.16})$$

$$k_1 = \frac{\tanh(\frac{\pi a}{4.0h})}{\tanh(\frac{\pi b}{4.0h})} \quad (\text{A.17})$$

$$k'_1 = \sqrt{1.0 - k_1^2} \quad (\text{A.18})$$

$$\epsilon_{\text{eff}} = \frac{1.0 + \epsilon_r \frac{K(k')}{K(k)} \frac{K(k_1)}{K(k'_1)}}{1.0 + \frac{K(k')}{K(k)} \frac{K(k_1)}{K(k'_1)}} \quad (\text{A.19})$$

## B. Verilog Code for SPI Interface for Delay Chips

```
'timescale 1ns / 1ps

module SDI_Delay_NB6L295(
    input [10:0]           In_1, In_2, In_3, In_4, In_5, In_6, In_7, In_8, // 
                           data for respective delay chips
    input                  Clk,
    input                  Reset,
    output reg [7:0]        EN, // enable signal for delay chips, active LOW
    output reg              SDIN, // configuration data
    output reg              SLOAD, // signals delay chip to load previously sent
                           data
    output                 SCLK // clock for serial communication with delay chips
);

reg                      start_clk;
assign SCLK = start_clk & (!Clk);

reg [21:0]             In_1_reg, In_2_reg, In_3_reg, In_4_reg, In_5_reg,
                       In_6_reg, In_7_reg, In_8_reg; // registers to intermediately store the
                           inputs
```

```

reg [7:0] select; // register used by Priority Encoder to detect
// which input changed

parameter DATA_SHIFT_WIDTH = 11; // number of bits to be shifted
// during transmission, 1 Data word = 11 bits
reg [4:0] clk_cnt;

reg [DATA_SHIFT_WIDTH-1:0] Data_reg; // register for storing data for
state machine

reg data_start; // signal for state machine to start sending
reg is_finished dataSent; // flags if transmission for one delay chip

parameter dly = 1; // delay control

reg delayReady;

always @ (posedge Clk)
begin
    if (select == 'd0) delayReady <= #dly 'b1;
    else delayReady <= #dly 'b0;
end

// Priority Encoder
// Check if any input has changed, select which data should be sent
// accordingly
always @ (posedge Clk)
begin
    if (Reset)
        begin
            In_1_reg <= #dly 'd0;
            In_2_reg <= #dly 'd0;
            In_3_reg <= #dly 'd0;
            In_4_reg <= #dly 'd0;
            In_5_reg <= #dly 'd0;
            In_6_reg <= #dly 'd0;
            In_7_reg <= #dly 'd0;
            In_8_reg <= #dly 'd0;
            Data_reg <= #dly 'd0;

            select <= #dly 'd0;

            start <= #dly 1'b0;;
        end
    else
        begin
            if (~start & delayReady)
                begin
                    select[7] <= #dly In_1_reg != In_1;
                    select[6] <= #dly In_2_reg != In_2;
                    select[5] <= #dly In_3_reg != In_3;
                    select[4] <= #dly In_4_reg != In_4;
                    select[3] <= #dly In_5_reg != In_5;
                    select[2] <= #dly In_6_reg != In_6;
                    select[1] <= #dly In_7_reg != In_7;
                    select[0] <= #dly In_8_reg != In_8;
                end
            else
                begin

```

```

        if (clk_cnt == 4'd12 & ~start_clk) // = end of
          sequence
            start           <= #dly 1'b0;
        else
          start           <= #dly 1'b1;
      end

      casex (select)
        8'b1???????: begin
          if (~dataSent)
            begin
              In_1_reg      <= #dly In_1;
              Data_reg       <= #dly In_1;
              EN             <= #dly
              8'b01111111;
              start          <= #dly 1'b1;
            end
          else
            begin
              start          <= #dly 1'b0;
              select[7]      <= #dly 1'b0;
            end
          end
        8'b01???????: begin
          if (~dataSent)
            begin
              In_2_reg      <= #dly In_2;
              Data_reg       <= #dly In_2;
              EN             <= #dly
              8'b10111111;
              start          <= #dly 1'b1;
            end
          else
            begin
              select[6]      <= #dly 1'b0;
              start          <= #dly 1'b0;
            end
          end
        8'b001?????: begin
          if (~dataSent)
            begin
              In_3_reg      <= #dly In_3;
              Data_reg       <= #dly In_3;
              EN             <= #dly
              8'b11011111;
              start          <= #dly 1'b1;
            end
          else
            begin
              select[5]      <= #dly 1'b0;
              start          <= #dly 1'b0;
            end
          end
        8'b0001?????: begin
          if (~dataSent)
            begin
              In_4_reg      <= #dly In_4;
              Data_reg       <= #dly In_4;
              EN             <= #dly
              8'b11101111;
            end
          end
        endcase
      end
    end
  end
end

```

```

                start          <= #dly 1'b1;
        end

    else
        begin
            select [4]      <= #dly 1'b0;
            start           <= #dly 1'b0;
        end
    end
8'b00001???: begin
    if (~dataSent)
        begin
            In_5_reg       <= #dly In_5;
            Data_reg        <= #dly In_5;
            EN              <= #dly
            8'b11110111;   start           <= #dly 1'b1;
        end
    end
else
    begin
        select [3]      <= #dly 1'b0;
        start           <= #dly 1'b0;
    end
end
8'b000001??: begin
    if (~dataSent)
        begin
            In_6_reg       <= #dly In_6;
            Data_reg        <= #dly In_6;
            EN              <= #dly
            8'b11111011;   start           <= #dly 1'b1;
        end
    end
else
    begin
        select [2]      <= #dly 1'b0;
        start           <= #dly 1'b0;
    end
end
8'b0000001?: begin
    if (~dataSent)
        begin
            In_7_reg       <= #dly In_7;
            Data_reg        <= #dly In_7;
            EN              <= #dly
            8'b11111101;   start           <= #dly 1'b1;
        end
    end
else
    begin
        select [1]      <= #dly 1'b0;
        start           <= #dly 1'b0;
    end
end
8'b00000001: begin
    if (~dataSent)
        begin
            In_8_reg       <= #dly In_8;
        end
    end

```

```

Data_reg <= #dly In_8;
EN <= #dly
8'b11111110;
start <= #dly 1'b1;
end
else
begin
    select [0] <= #dly 1'b0;
    start <= #dly 1'b0;
end
end
default:
begin
    EN <= #dly
    8'b11111111;
    start <= #dly 1'b0;
end
endcase
end
end

// State Machine for Sending Configuration Data to Delay Chip NB6L295
/*
State Description
-----
RESET Resetting all parameters and registers ->
if (reset): stay; else: to IDLE
IDLE Waiting for start signal from priority
encoder -> if (start): to LOAD_P0; else: stay
LOAD_P0 Load first half of Delay_X - which
corresponds to data for Delay PD0 on delay chip - into
temporary register -> to LOAD_P1
LOAD_P1 Load second half of Delay_X - which
corresponds to data for Delay PD1 on delay chip - into
temporary register -> to SHIFT
SHIFT Shift bits for sending serial bitstream to
SDIN, assert SLOAD -> to END
END End transmission, deassert SLOAD, inform
priority encoder about end of transmission -> to IDLE
*/
parameter RESET = 3'd0;
parameter IDLE = 3'd1;
parameter LOAD = 3'd2;
parameter SHIFT = 3'd3;
parameter END = 3'd4;
reg [2:0] STATE;
reg [DATA_SHIFT_WIDTH-1:0] tmp;

always @ (posedge Clk)
begin
    if (Reset)
        begin
            STATE <= #dly RESET;
            tmp <= #dly 'd0;
            dataSent <= #dly 1'b0;
            start_clk <= #dly 1'b0;
            SLOAD <= #dly 1'b0;
            clk_cnt <= #dly 1'b0;
        end
    else
        begin
            case (STATE)

```

```

RESET:
begin
  if (Reset)
    STATE    <= #dly RESET;
  else
    STATE    <= #dly IDLE;
end // RESET

IDLE:
begin
  SDIN      <= #dly 1'b0;
  clk_cnt   <= #dly 5'd0;
  dataSent  <= #dly 1'b0;
  SLOAD     <= #dly 1'b0;

  if (start & ~dataSent)
    STATE    <= #dly LOAD;
  else
    STATE    <= #dly IDLE;
end // IDLE

LOAD:
begin
  tmp       <= #dly Data_reg;
  STATE    <= #dly SHIFT;
end // LOAD_W1

SHIFT:
begin
  if (clk_cnt < 4'd12) // number of bits to be
  shifted //
  begin
    start_clk      <= #dly 1'b1;
    clk_cnt        <= #dly clk_cnt +1;
    tmp            <= #dly
                  {tmp[DATA_SHIFT_WIDTH-2:0], 1'b0};
    SDIN          <= #dly
                  tmp[DATA_SHIFT_WIDTH-1];
  end
  else
  begin
    SLOAD         <= #dly 1'b1;
    clk_cnt       <= #dly
                  clk_cnt;
    start_clk     <= #dly 1'b0;
    STATE         <= #dly END;
    SDIN          <= #dly 1'b0;
  end
end // SHIFT

END:
begin
  SLOAD         <= #dly 1'b0;
  start_clk     <= #dly 1'b0;
  dataSent      <= #dly 1'b1;
  clk_cnt       <= #dly clk_cnt;
  SDIN          <= #dly 1'b0;
  STATE         <= #dly IDLE;
end // END
default:
  STATE    <= #dly RESET;
endcase
end
endmodule

```



# Acronyms

- AC** Alternating Current. 42, 53
- ADC** Analog-To-Digital-Converter. v, 1, 2, 5, 10, 12, 13, 15–22, 24, 28, 29, 33–35, 37–39, 42, 45, 46, 54, 55, 61, 81, 83, 84, 89
- AI** Artificial Intelligence. 90
- ANR** Agence Nationale de la Recherche. 8, 90
- API** Application Programming Interface. 87, 88
- APU** Application Processing Unit. 81
- AXI** Advanced eXtensible Interface. 84
- CML** Current Mode Logic. 49
- CPU** Central Processing Unit. 28, 87
- CSR** Coherent Synchrotron Radiation. 1, 7, 9, 10, 90
- DAC** Digital-To-Analog-Converter. 15, 39, 45, 46, 54, 60, 78, 81, 83, 84
- DAQ** Data Acquisition System. v, 1, 2, 5, 6, 28, 30, 84, 89
- dBc** decibels relative to the carrier. 20
- dBFS** decibels relative to full scale. 20
- DC** Direct Current. 20, 28, 34, 52
- DDR** Double Data Rate. 84, 89
- DDR3** Double Data Rate Gen 3. 30
- DDR4** Double Data Rate Gen 4. 81
- DFG** Deutsche Forschungsgemeinschaft. 8, 90
- DIMM** Dual In-Line Memory Module. 81
- DNL** Differential Nonlinearity. 18
- EMI** Electro-Magnetic Interference. 42, 57, 61, 62, 65
- ENOB** Effective Number Of Bits. 1, 2, 20
- EO** Electro-Optic. 9, 10, 90
- EOS** Electro-Optic Sampling. 9
- ERNIC** Xilinx Embedded RDMA enabled NIC. 87

**ESL** Equivalent-Series-Inductance. 43

**ESR** Equivalent-Series-Resistance. 42, 43

**FFT** Fast-Fourier-Transform. 19, 30

**FMC** FPGA Mezzanine Card. 44–46, 49, 51, 52, 54, 57, 59, 61, 64, 78, 81, 82

**FPGA** Field Programmable Gate Array. v, 2, 8, 9, 28–30, 39, 44, 46, 54, 60, 77, 78, 81–84, 88–90

**FS** Full-Scale. 47

**FWHM** Full Width At Half Maximum. 28

**GPU** Graphics Processing Unit. 28, 30, 32

**GUI** Graphical User Interface. x, 83, 84

**HDL** Hardware Description Language. 85, 86

**HSPCe** High Serial Pin Count Extension. 44

**HWP** Half-Wave Plate. 9

**IBPT** Institute of Beam Physics and Technology. 6

**IBTA** InfiniBand Trade Association. 87

**IC** Integrated Circuit. 39, 40, 42, 61

**IDE** Integrated Design Environment. 85

**IEEE** Institute of Electrical and Electronics Engineers. 45

**INL** Integral Nonlinearity. 18

**IP** Intellectual Property. 82, 85, 87

**IPE** Institute for Data Processing and Electronics. 27–29, 90

**KAPTURE** Karlsruhe Pulse Taking Ultra-fast Readout Electronics. 2, 27–29, 31–33, 46, 49, 63, 68, 69

**KAPTURE-2** Karlsruhe Pulse Taking Ultra-fast Readout Electronics 2. 28, 32

**KARA** Karlsruhe Research Accelerator. vi, 2, 5–7, 27–29, 46, 54, 90

**KIT** Karlsruhe Institute of Technology. 6, 27

**LDO** Low Dropout Voltage Regulator. 63, 64

**LINAC** linear accelerator. 5

**LNA** Low-Noise-Amplifier. 28

**LPAF** Low Profile Array, Female. 45

**LPAM** Low Profile Array, Male. 45–47

**LSB** Least Significant Bit. 12, 15, 17, 18, 22

**LVDS** Low Voltage Differential Signaling. 41

- LVPECL** Low-Voltage Positive Emitter-Coupled Logic. 49, 50, 52, 59
- MMIC** Microwave Monolithic Integrated Circuit. 28
- NIC** Network Interface Controller. 87
- NVMe** Non-Volatile Memory Express. 87
- PCB** Printed Circuit Board. v, 41–44, 47, 49, 64–68, 72, 77
- PCIe** PCI Express. 2, 29, 30
- PL** programmable logic. 81–85
- PLL** Phase-Locked-Loop. 29, 32, 33, 46, 54–57, 59, 61, 78, 84
- PS** processing system. 81, 83, 84, 87
- QWP** Quarter-Wave Plate. 9
- RDMA** Remote Direct Memory Access. 87
- RF** Radio Frequency. x, 6, 29, 45, 46, 60, 67, 77, 78, 81, 82, 85, 86
- RFSoC** Radio-Frequency System-On-Chip. v, 39, 81, 87, 89
- RMS** Root Mean Square. 19, 20, 22, 52
- RoCE** RDMA over Converged Ethernet. 87
- RoCEv2** RDMA over Converged Ethernet Version 2. 87
- RPU** Real-Time Processing Unit. 81
- SDI** Serial Data Interface. x, 49, 84, 86
- SFDR** Spurious-Free Dynamic Range. 19–21, 90
- SFP** Small Form-Factor Pluggable. 81
- SHA** Sample-And-Hold-Amplifier. 13, 18, 19, 21
- SINAD** Signal-to-Noise-and-Distortion Ratio. 20, 90
- SJNR** Signal-to-Jitter-Noise-Ratio. 22
- SNR** Signal-To-Noise-Ratio. 15, 16, 19, 20, 22
- SoC** System-On-Chip. 2, 39, 88
- SODIMM** Small Outline Dual In-Line Memory Module. 81
- SOLEIL** Source optimisée de lumière d'énergie intermédiaire du LURE. 1, 90
- SPI** Serial Peripheral Interface. 41, 44, 59, 84, 85
- SR** synchrotron radiation. 5, 6, 8
- THA** Track-And-Hold-Amplifier. v, 13, 28, 29, 33, 37, 38, 42, 45–49, 52–54, 61–63, 65, 68, 72, 74, 77, 78, 89
- THERESA** Terahertz Readout Sampling. v, 2, 8, 27, 28, 33, 36, 37, 39, 46, 49, 89, 90

**THz** Terahertz. 2, 5–10, 27–29, 90

**TS-QPI** time-stretch quantitative phase imaging. 1

**ULTRASYNC** Exploration et contrôle ULTRArapide de la dynamique des paquets d'électrons dans les sources de lumière SYNChrotron. 8, 90

**USB** Universal Serial Bus. 84, 87

**VCO** Voltage-Controlled Oscillator. 55, 56

**VCXO** Voltage-Controlled Crystal Oscillator. 54

**VITA** VMEbus International Trade Association. 44

**WP** Wollaston Prism. 9

# Bibliography

- [Anaa] Analog Devices: *2 A, Low Dropout, CMOS Linear Regulator.* [https://www.analog.com/media/en/technical-documentation/data-sheets/ADP1740\\_1741.pdf](https://www.analog.com/media/en/technical-documentation/data-sheets/ADP1740_1741.pdf), Rev. H.
- [Anab] Analog Devices: *28 Gbps, 5-Bit, Digital Time Delay with Programmable Output Voltage.* <https://www.onsemi.com/pdf/datasheet/nb61295-d.pdf>, Rev. 4.
- [Anac] Analog Devices: *Decoupling Techniques.* <https://www.analog.com/media/en/training-seminars/tutorials/MT-101.pdf>, Tutorial.
- [Anad] Analog Devices: *WIDEBAND 4 GS/s TRACK-AND-HOLD AMPLIFIER DC - 5 GHz.* <https://www.analog.com/media/en/technical-documentation/data-sheets/hmc760.pdf>, v01.0514.
- [Ban] Banerjee, Dean: *PLL Performance, Simulation and Design.* <https://www.ti.com/cn/lit/ml/snna106c/snna106c.pdf>, 5th edition.
- [BBB<sup>+</sup>19] Bielawski, Serge, Edmund Blomley, Miriam Brosi, Erik Bründermann, Eva Burkard, Clément Evain, Stefan Funkner, Nicole Hiller, Michael Nasse, Gudrun Niehues und et al.: *From self-organization in relativistic electron bunches to coherent synchrotron light: observation using a photonic time-stretch digitizer.* Scientific Reports, 9(1), July 2019. <http://dx.doi.org/10.1038/s41598-019-45024-2>.
- [Bri] Britannica: *Dielectric constant of air.* <https://www.britannica.com/science/dielectric-constant>, [Online; accessed 2021-08-09].
- [Bro20] Brosi, Miriam: *In-Depth Analysis of the Micro-Bunching Characteristics in Single and Multi-Bunch Operation at KARA.* Dissertation, Karlsruher Institut für Technologie (KIT), 2020. 54.01.01; LK 01.
- [BSMM99] Bronstein, Semendjajew, Musiol und Mühlig: *Taschenbuch der Mathematik.* Verlag Harri Deutsch, 1999.
- [CAB<sup>+</sup>17] Caselle, M., L.E. Ardila Perez, M. Balzer, A. Kopmann, L. Rota, M. Weber, M. Brosi, J. Steinmann, E. Bründermann und A. S. Müller: *Kapture-2. a picosecond sampling system for individual thz pulses with high repetition rate.* Journal of Instrumentation, 12, 2017.
- [CBC<sup>+</sup>13] Caselle, M., M. Balzer, S. Cilingaryan, M. Hofherr, V. Judin, fjtA. Kopmann, K. Ll'in, A. Menshikov, A. S. Müller, N.J. Smale, P. Thoma, S. Wuensch, M. Siegel und M. Weber: *Ultra-fast data acquisition system for coherent synchrotron radiation based on superconducting terahertz detectors.* In: *IPAC 2013: Proceedings of the 4th International Particle Accelerator Conference*, Seiten 2094–2096. Asian Committee for Future Accelerators (ACFA), 2013, ISBN 978-3-9545012-2-9. 55.51.10; LK 02.

- [CBC<sup>+</sup>14] Caselle, M, M Balzer, S Chilingaryan, M Hofherr, V Judin, A Kopmann, N J Smale, P Thoma, S Wuensch, A S Müller, M Siegel und M Weber: *An ultra-fast data acquisition system for coherent synchrotron radiation with terahertz detectors*. Journal of Instrumentation, 9(01):C01024–C01024, jan 2014. <https://doi.org/10.1088/1748-0221/9/01/c01024>.
- [CBJ99] Coppinger, F., A.S. Bhushan und B. Jalali: *Photonic time stretch and its application to analog-to-digital conversion*. IEEE Transactions on Microwave Theory and Techniques, 47(7):1309–1314, 1999.
- [Col21] College, Mohawk Valley Community: *Slew Rate and Power Bandwidth*, März 2021. <https://eng.libretexts.org/@go/page/3575>, [Online; accessed 2021-07-16].
- [DID] DIDACTIC, LD: *Demonstrating the pockels effect in a conoscopic beam path*. [https://www.ld-didactic.de/literatur/hb/e/p5/p5451\\_e.pdf](https://www.ld-didactic.de/literatur/hb/e/p5/p5451_e.pdf).
- [DK20] Dang, Hoang Long und Sangshin Kwak: *Review of Health Monitoring Techniques for Capacitors Used in Power Electronics Converters*. Sensors, 20(13), 2020, ISSN 1424-8220. <https://www.mdpi.com/1424-8220/20/13/3740>.
- [Ele] Electronics, Wavelength: *What is a photodiode?* <https://www.teamwavelength.com/photodiode-basics/>, [Online; accessed 2021-07-26].
- [ESR] ESRF: *Synchrotron radiation properties*. <https://www.esrf.fr/about/ask-an-expert/questions-answers>, [Online; accessed 2021-08-09].
- [FMC] FMCHUB - FPGA MEZZANINE CARDs: *Vita 57 fpga mezzanine card (fmc) signals and pinout of high-pin count (hpc) and low-pin count (lpc) connectors*. [https://fmchub.github.io/appendix/VITA57\\_FMC\\_HPC\\_LPC\\_SIGNALS\\_AND\\_PINOUT.html](https://fmchub.github.io/appendix/VITA57_FMC_HPC_LPC_SIGNALS_AND_PINOUT.html), [Online; accessed 2021-07-17].
- [Har19] Harris, Jonathan: *The abcs of interleaved adcs*, 2019. <https://www.analog.com/en/technical-articles/the-abcs-of-interleaved-adcs.html>.
- [Kei] Keim, Robert: *pn-junction*. [https://www.allaboutcircuits.com/uploads/articles/4.3\\_The\\_pn\\_Junction\\_and\\_the\\_Diode1\\_.jpg](https://www.allaboutcircuits.com/uploads/articles/4.3_The_pn_Junction_and_the_Diode1_.jpg), [Online; accessed 2021-08-08].
- [Kes05] Kester, Walt: *The Data Conversion Handbook*. Newnes, 2005.
- [Kes09] Kester, Walt: *Understand sinad, enob, snr, thd, thd + n, and sfdr so you don't get lost in the noise floor*. Januar 2009.
- [LV02] Lundberg, Kent H. und Vin Vq: *Analog-to-digital converter testing*, 2002.
- [MCB<sup>+</sup>17] Mahjoubfar, A., D. Churkin, S. Barland, N. Broderick, S. Turitsyn und B. Jalali: *Time stretch and its applications*. Nature Photonics, 11:341–351, 2017.
- [Mic] Michele Caselle. Personal communication. KIT-IPE.
- [Mik] Mike Wang: *Timing is everything: Understanding lvpecl and a newer lvpecl-like output driver*. <https://bit.ly/3iIsTAm>, [Online; accessed 2021-07-18].
- [MR15] Manganaro, Gabriele und Dave Robertson: *Interleaving adcs: Unraveling the mysteries*. Analog Dialogue, 2015.
- [Mü12] Müller, Anke Susanne: *Accelerator-Based Sources of Infrared and Terahertz Radiation*. Reviews of Accelerator Science and Technology, 03, April 2012.
- [Nyg28] Nyquist, H.: *Certain Topics in Telegraph Transmission Theory*. Transactions of the American Institute of Electrical Engineers, 47(2):617–644, 1928.

- [ONS] ONSem: *2.5V / 3.3V Dual Channel Programmable Clock/Data Delay with Differential LVPECL Outputs*. <https://www.analog.com/media/en/technical-documentation/data-sheets/hmc856.pdf>, Rev. D.
- [our] ourPCB: *PCB Via: What is it, and Which Type Should You Choose?* <https://www.ourpcb.com/pcb-via.html>, [Online; accessed 2021-07-18].
- [PCM] PCMag: *Definition: Mezzanine card*. <https://www.pc当地/encyclopedia/term/mezzanine-card>, [Online; accessed 2021-07-17].
- [Pue15] Puente León, Fernando: *Messtechnik - Systemtheorie für Ingenieure und Informatiker*. Vieweg Verlag, 10. aufl. Auflage, 2015, ISBN 978-3-662-44820-5.
- [Ree17] Reeder, Rob: *Radically extending bandwidth to crush the x-band frequencies using a track-and-hold sampling amplifier and rf adc*, 2017. <https://www.analog.com/en/analog-dialogue/articles/radically-extending-bandwidth-to-crush-the-x-band-frequencies.html>, [Online; accessed 2021-07-16].
- [RELP<sup>+</sup>15] Roussel, Eleonore, Clément Evain, Marc Le Parquier, Christophe Szwaj, Serge Bielawski, Laurent Manceron, Jean Blaise Brubach, M. A Tordeux, Jean Paul Ricaud, L Cassinari, M Labat, Marie Emmanuelne Couprie und Pascale Roy: *Observing microscopic structures of a relativistic object using a time-stretch strategy*. Scientific Reports, 5, Mai 2015.
- [Rot18] Rota, Lorenzo: *KALYPSO, a novel detector system for high-repetition rate and real-time beam diagnostics*. Dissertation, Karlsruher Institut für Technologie (KIT), 2018. 54.02.02; LK 01.
- [Rou14] Roussel, Eleonore: *Spatio-temporal dynamics of relativistic electron bunches during the microbunching instability: study of the Synchrotron SOLEIL and UVSOR storage rings*. Dissertation, September 2014.
- [SAM] SAMTEC: *Rendering of fmc+ connector*. <https://www.mouser.in/images/marketingid/2019/img/140577954.png?v=052120.0746>, [Online; accessed 2021-07-17].
- [See09] Seelam, Raj: *I/o design flexibility with the fpga mezzanine card (fmc)*, 2009. [https://www.xilinx.com/support/documentation/white\\_papers/wp315.pdf](https://www.xilinx.com/support/documentation/white_papers/wp315.pdf).
- [Ser] Serge Bielawski. Personal communication. PhLAM, Lille University.
- [Sha49] Shannon, C.E.: *Communication in the Presence of Noise*. Proceedings of the IRE, 37(1):10–21, 1949.
- [Tex] Texas Instruments: *LMK0480x Low-Noise Clock Jitter Cleaner with Dual Loop PLLs*. [https://www.ti.com/lit/ds/symlink/lmk04808.pdf?ts=1628076639562&ref\\_url=https%253A%252F%252Fwww.google.com%252F](https://www.ti.com/lit/ds/symlink/lmk04808.pdf?ts=1628076639562&ref_url=https%253A%252F%252Fwww.google.com%252F), Revised 12/2014.
- [Thi17] Thierauf, Stephen: *High-Speed Circuit Board Signal Integrity, Second Edition*. 2017.
- [Vol] Vollrath, Prof. Dr. Jörg: *Ideal adc, dnl and inl*. [https://personalpages.hs-kempten.de/~vollratj/InEl/2016\\_10\\_10\\_03\\_InEl\\_DNL\\_INL.html](https://personalpages.hs-kempten.de/~vollratj/InEl/2016_10_10_03_InEl_DNL_INL.html), [Online; accessed 2021-07-27].
- [Wad91] Wadell, Brian C.: *Transmission Line Design Handbook*. Artech House, 1991.

- [wil] *Noise and Distortion*. John Wiley and Sons, Ltd, ISBN 9780470841624. <https://onlinelibrary.wiley.com/doi/abs/10.1002/0470841621.ch2>.
- [Xila] Xilinx: *Understanding Key Parameters for RF-Sampling Data Converters*. [https://www.xilinx.com/support/documentation/white\\_papers/wp509-rfsampling-data-converters.pdf](https://www.xilinx.com/support/documentation/white_papers/wp509-rfsampling-data-converters.pdf), v1.0.
- [Xilb] Xilinx: *Xilinx Embedded RDMA Enabled NIC v3.1*. [https://www.xilinx.com/support/documentation/ip\\_documentation/ernic/v3\\_1/pg332-ernic.pdf](https://www.xilinx.com/support/documentation/ip_documentation/ernic/v3_1/pg332-ernic.pdf), Revised 06/2021.
- [Xilc] Xilinx: *Zcu216 product page*. <https://www.xilinx.com/products/boards-and-kits/zcu216.html>.
- [Xild] Xilinx: *Zu49dr*. <https://www.xilinx.com/products/silicon-devices/soc/rfsoc.html>, [Online; accessed 2021-08-01].
- [Xile] Xilinx Inc.: *UltraScale Architecture PCB Design*. <http://xilinx.eetrend.com/files-eetrend-xilinx/download/201408/7602-13778-ug583-ultrascale-pcb-design.pdf>, Advance Specification User Guide.
- [Xil20] Xilinx: *Ug1433 - zynq ultrascale+ rfsoczcu208 and zcu216 rf-data converter evaluation tool user guide*, June 2020. [https://www.xilinx.com/support/documentation/boards\\_and\\_kits/zcu216/ug1433-zcu216-rfsoc-eval-tool.pdf](https://www.xilinx.com/support/documentation/boards_and_kits/zcu216/ug1433-zcu216-rfsoc-eval-tool.pdf).